Radome Design and Curvature Effects on Antenna Performance, with Application to Radar Array Installation in Transonic Aircraft

By
© 2019
Alejandra Stefania Escalera Mendoza
B.S., University of Kansas, 2014

Submitted to the graduate degree program in Aerospace Engineering and the Graduate Faculty of the University of Kansas in partial fulfillment of the requirements for the degree of Master's of Science.

_____

Dr. Richard Hale
Spahr Professor and Chair
(Chairperson)

_____

Dr. Emily Arnold
Assistant Professor of Aerospace Engineering
(Committee Member)

_____

Dr. Mark Ewing
Associate Professor of Aerospace Engineering
(Committee Member)

Date Defended: May 20th, 2019

The thesis committee for Alejandra Stefania Escalera Mendoza
certifies that this is the approved version of the following thesis:

Radome Design and Curvature Effects on Antenna Performance, with Application to Radar Array Installation in Transonic Aircraft

_____

Dr. Richard Hale
Spahr Professor and Chair
(Chairperson)

_____

Dr. Emily Arnold
Assistant Professor of Aerospace Engineering
(Committee Member)

_____

Dr. Mark Ewing
Associate Professor of Aerospace Engineering
(Committee Member)

Date Approved: June 3rd, 2019

Abstract

Significant and fast changes in the cryosphere have been observed and monitored using radioglaciology and remote sensing technology. A fuselage mounted Ultrawideband Multichannel Coherent Radar Depth Sounder (UWB MCoRDS) with eight Tx/Rx channels was proposed for measuring polar ice sheets to depths up to six kilometers. This radar system operates in the 150-600 MHz frequency range and would be integrated onto the DC-8 aircraft platform for remote sensing.

The high speed of the aircraft (M=0.8) results in high design loads that restrict the size of the radome and can thus limit the capability of the radar system. The desire to increase the size of the array along the cross-track direction to improve system performance resulted in an increase in radome size of 73% spanwise and 52.5% chordwise compared to systems previously installed on the DC-8. This significant increase in size and mass required investigating methods to reduce the aerodynamic loading while minimizing negative effects on the performance of the UWB MCoRDS antenna. These methods include reducing the radome depth by decreasing the antenna ground plane distance, and conforming the antenna or ground plane to more aerodynamically efficient profiles.

Two dimensional CFD analyses show that conforming the radome to a supercritical airfoil shape results in lower aerodynamic loads compared to only reducing the radome depth. Single antenna electromagnetic simulations indicate that variations in ground plane distance or the addition of curvature to the radiating/reflecting components affect the antenna performance differently depending on the frequency range and antenna parameter of interest. Changes of 0.59 in. (15 mm) or less in effective ground plane distance minimally impacts the return loss for the UWB MCoRDS antenna addressed herein. Smaller ground plane distances reduce the gain for $f \leq 450$ MHz (improves it for $f > 450$ MHz), but have negligible effects on the cross-track half power beam width (HPBW) in the 200-400 MHz range. Larger ground plane distances at the feed generally widen the main beam in both cross-track and along-track directions. Similar results are observed for either adding curvature to the ground plane or the antenna (in both cases the ground plane distance at the feed location is increased).

Conforming the UWB MCoRDS antenna to a SC0010 airfoil curvature results in minimal changes to the simulated return loss, less than 0.5dB change in gain, and less than 8 degrees change in cross-track HPBW. These results were experimentally verified using a bare UWB MCoRDS antenna. However, a 1.93dB reduction in gain at 550 MHz was observed instead, and the main beam does not have a dip at nadir for frequencies higher than 475 MHz. Deviations from the simulation results, in these instances, are attributed to the use of ideal properties in simulations and possible errors introduced by the test set-up structure among other reasons discussed herein.

By considering the antenna array performance rather than the single antenna element performance, conforming the antennas does not have noticeable effects in the normalized cross-track pattern and HPBW, but the single antenna effects are still evident in the array gain. The radar range equation for extended targets shows that higher frequencies are mainly affected by conforming the antenna due to large gain reductions in the 350-575 MHz frequency range. However, conforming the antennas to a supercritical airfoil shape is preferred instead of reducing the number of elements as the latter limits the radar system performance much more significantly. Negative effects on antenna performance caused by curving the antenna can be compensated, if needed, with variations in flight altitude, transmit power, and other signal processing techniques. The radome design for an eight UWB MCoRDS antenna array with a cross-section that maintains the curvature of the supercritical airfoil is proven to be aerodynamically effective and electromagnetically feasible, and is expected to result in improved structural performance due to significantly reduced drag loading.

Acknowledgements

I would first like to thank the KU-AE and CReSIS faculty and staff for their continuous support and encouragement in all my years at KU. Their generosity and interest on the success of students have been paramount to my great experiences as an undergraduate and graduate student.

I would also like to thank my peers and colleagues for their willingness to help and answer questions. I have gained deeper knowledge through their individual expertise, learned how to work more effectively in groups, and had a great time sharing and learning about our different background experiences.

Next I would like to thank Dr. Emily Arnold. Electrical engineering was a daunting field to me before starting to work with her and taking her antenna's course. Because of her excellent instruction skills and genuine interest in her students, I gained deep interest and appreciation for electromagnetics and the vast number of applications that this field has.

I am most thankful to my advisor Dr. Richard Hale. He provided me the opportunity to gain manufacturing skills in the Composite Laboratory as a sophomore at KU when I had no previous experience. These skills have served me to obtain a job upon my B.S. graduation and to be a better structures engineer while in industry and graduate school. His expertise in composite materials, manufacturing, and aircraft integration have inspired me to pursue a career in the structures field and also to pursue higher education degrees. His advice and support for professional and personal decisions have greatly influenced my formation into the engineer I am today. I will always be thankful to him for all the growth opportunities he has provided me.

Finally, I am immensely thankful to my family, friends and loved ones for their unconditional support, encouragement and love through all my years in the U.S. You have given me the strength to pursue and achieve higher goals than I could have ever imagined. Despite the long distance in the U.S. or all the way to my home country Bolivia, I have always kept your instruction and advice in mind. Thank you for the insightful discussions that allow me to think outside the box, for being interested in knowing and learning about what I do, and for constantly reminding me that you are always there for me.

Table of Contents

List of Figures

List of Tables

List of Equations

List of Symbols

Acronyms and Abbreviations

Acronym or Abbreviation	*Description*
2D	Two Dimensional
3D	Three Dimensional
AN	Army-Navy Specification Series
AUT	Antenna Under Test
CAD	Computer Aided Design
CF	Center Frequency
CFD	Computational Fluid Dynamics
CReSIS	Center for Remote Sensing of Ice Sheets
FEM	Finite Element Model
FS	Fuselage Station or Factor of Safety
FWD	Forward
GP	Ground Plane
HF	High Frequency
HFSS	High Frequency Structure Simulator
KU	University of Kansas
LF	Low Frequency
MS	Margin of Safety
NACA	National Advisory Committee for Aeronautics
NAS	National Aerospace Standard
NASA	National Aeronautics and Space Administration
SAR	Synthetic Aperture Radar
SC	Supercritical
TE	Trailing Edge
UWB MCoRDS	Ultrawideband Multichannel Coherent Radar Depth Sounder

Symbols

Symbol	*Description*	*Units*
B	Bandwidth	MHz
c	Speed of Light	m/s or ft/s
F	Frequency	MHz
G	Gain	dBi

HPBW	Half Power Beam Width	°
l	Length	in. or m
M	Mach Number	~
N	Gust Maneuvering Load Factor	~
P	Power	W
q	Dynamic Pressure	psf
R	Slant Range	in. or m
Rx	Receiving element/receive	~
S_{11}	Return Loss S-Parameter	dB
S_{21}	Transmission S-Parameter	dB
t/c	Thickness to chord ratio	~
T	Temperature	°F
Tx	Transmitting element/transmit	~
x	position along length	in. or m
α, AoA	Angle of Attack	°
β	Sideslip angle	°
ΔA	Spatial Resolution	$in.^2$ or m^2
Δx	Cross-track Resolution	in. or m
Δy	Along-track Resolution	in. or m
θ	Elevation Angle	°
λ	Wavelength	in. or m
σ^o	Backscattering Coefficient	~
τ_p	Pulse Duration	s
φ	Azimuth Angle	°

Subscripts

Subscript	*Description*
az	Azimuth
max	Maximum
r	receive
t	transmit
x	Element or Drag Direction
z	Lift Direction

1. Introduction

Rapid changes in area, volume and mass of ice sheets, glaciers and sea ice in Antarctica and Greenland have been observed in the last decades. The 2013 technical summary report of the United Nations Intergovernmental Panel on Climate Change states that the ice sheet mass loss is due to summer surface melt and increased glacier discharge (Ref. 1). This has accelerated over the last decades, and significant changes (region dependent) have been observed in the extent of the sea ice. The "changes in the water cycle and cryosphere" section of Ref. 1 indicates that glaciers around the globe are persistently shrinking and are expected to continue shrinking in the future disregarding further temperature increase.

These changes have been monitored over wide areas with continuous advancements in radioglaciology and remote sensing (Ref. 2). Airborne remote sensing provides the advantage of measuring areas that would otherwise be inaccessible or dangerous, reduces the time to cover extensive regions, and can provide results with high resolution. In this case, the capability of the radar system has to be maximized within the constraints imposed by the type of aircraft platform selected for the mission and the corresponding flight conditions.

Radar technology uses radio waves to measure the ice surface, depth of the ice column, and ice bed topography to improve the scientific knowledge of the cryosphere and its changes through time. Similar principles apply for measuring snow on ice (Ref. 2). The Center for Remote Sensing of Ice Sheets (CReSIS) has developed radar systems that provide a wide-coverage sounding and imaging of the polar ice sheets from various aircraft platforms. These include the Ultrawideband Multichannel Coherent Radar Depth Sounder (UWB MCoRDS) that operates in the 150-600 MHz frequency range. This radar is optimized for mapping the ice layers to depths of several kilometers (Ref. 3).

The author of this thesis studies the effects on the electromagnetic performance of the UWB MCoRDS antenna due to aerodynamic and structural restrictions on radome geometry and mass. These are specifically studied with respect to restrictions imposed for radome integration onto the McDonnell Douglas DC-8 research aircraft for ice-sounding applications. The DC-8 has a top speed of M=0.8 at an altitude of 30,000 ft (9.14 km) which results in high aerodynamic and

structural loads that limit the size of the radome and hence limit the size and extent of the radar array. The author investigates methods to reduce the aerodynamic loading. These include re-shaping of the radome cross-section by changing the antenna ground plane distance, and conforming the flat ground plane or the flat antenna to a more aerodynamically suitable shape.

The following sub-sections describe the capabilities and restrictions of past missions, explain the objective and feasibility of the proposed mission with the UWB MCoRDS radar on the DC-8, and define the organization of the author's research.

1.1. Mission Description and Technology Background

The University of Kansas (KU) CReSIS team proposed in 2018 the use of the UWB MCoRDS radar in an 8-channel configuration for measurements of polar ice sheets using the DC-8 research aircraft platform. The UWB MCoRDS system has flown multiple times on the Basler BT-67 aircraft (modified DC-3) with 24-channel and 8-channel configurations. The 24-channel configuration includes an 8-channel fuselage mounted Tx/Rx sub-array, and two 8-channel Rx-only wing mounted sub-arrays as shown in Figure 1. The 8-channel configuration includes only the fuselage array and has reduced bandwidth (Ref. 3).

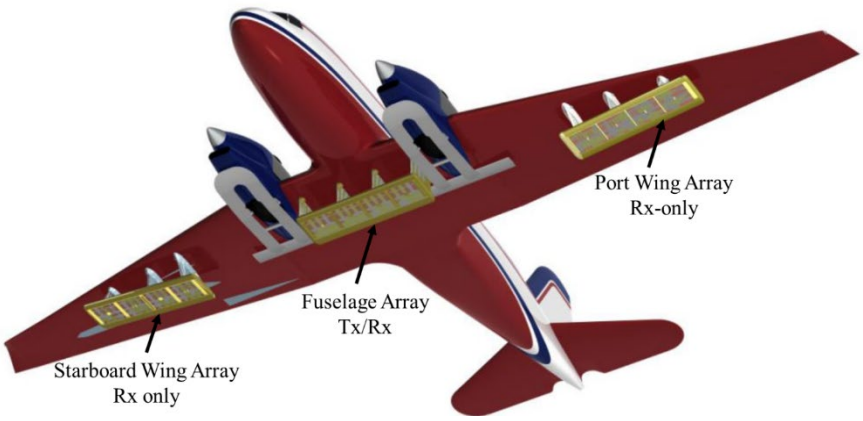

Figure 1: UWB MCoRDS Antennas Installed on BT-67 Aircraft (Ref. 3 & 4)

CReSIS has operated earlier generations of the MCoRDS antenna on various aircraft (DC-8, P-3, and C-130) for multiple deployments. The current fairing on the DC-8 with antennas that operate in the 165-215 MHz frequency range is shown in Figure 2 (Ref. 2).

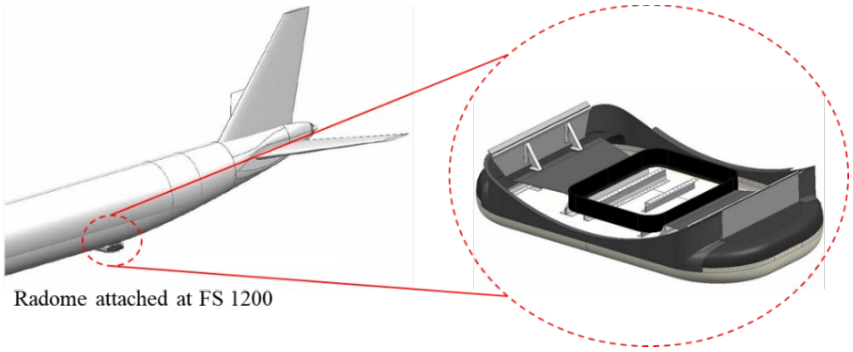

Figure 2: Current Radome Attached to Nadir Port Frame of the DC-8 with Earlier Generation of MCoRDS Antenna (Ref. 5)

The DC-8 has only one attachment location at FS 1200 as shown above, thus the proposed mission would only use the Tx/Rx UWB MCoRDS antenna array. This requires the development of a new radome with similar fuselage mounting structure as the current radome. Aerodynamic, structural and electromagnetic analysis are required to prove that the concept is viable and to obtain airworthiness certification.

1.2. Motivation for Studies

The 143.5 in. x 32in. (3.64 m x 0.81 m) 8-element fuselage UWB MCoRDS array results in a preliminary radome design, created by the author of this thesis, which has a span of 172.1 in. (4.37 m) and a chord of 87.1 in. (2.21 m). This is larger by 73% spanwise and 52.5% chordwise than the span and chord of the current radome (99.3 in. or 2.52 m and 57.1 in. or 1.45 m respectively) as shown in Figure 3. The new radome concept was generated with similar characteristics as other radomes used in previous missions. These include:

- Placing the dipole antennas on the bottom surface of the radome;
- Assuming both the antenna and the bottom radome section are flat;
- Using same ground plane distance and element spacing as in the BT-67 installation;
- Including a gap between the ground plane and the top surface of the radome to accommodate and aerodynamically fair in electronic hardware (cables and matching networks that need to be placed on the ground plane and directly above the antennas) and radome mounting structure.

Figure 3 shows that the edges of the new radome extend past the diameter of the fuselage at FS 1200 whereas the current radome is within the fuselage dimension. The radome regions further away from the center of the fuselage experience higher aerodynamic loads (higher magnitude shockwaves and pressure) than regions closer to the centerline. These are augmented at the high speed and altitude cruise of the DC-8. For these reasons, the first iteration of the new radome design was reduced in depth compared to the current radome. The trailing edge was also elongated as shown below to reduce drag due to flow separation and to avoid vortex shedding.

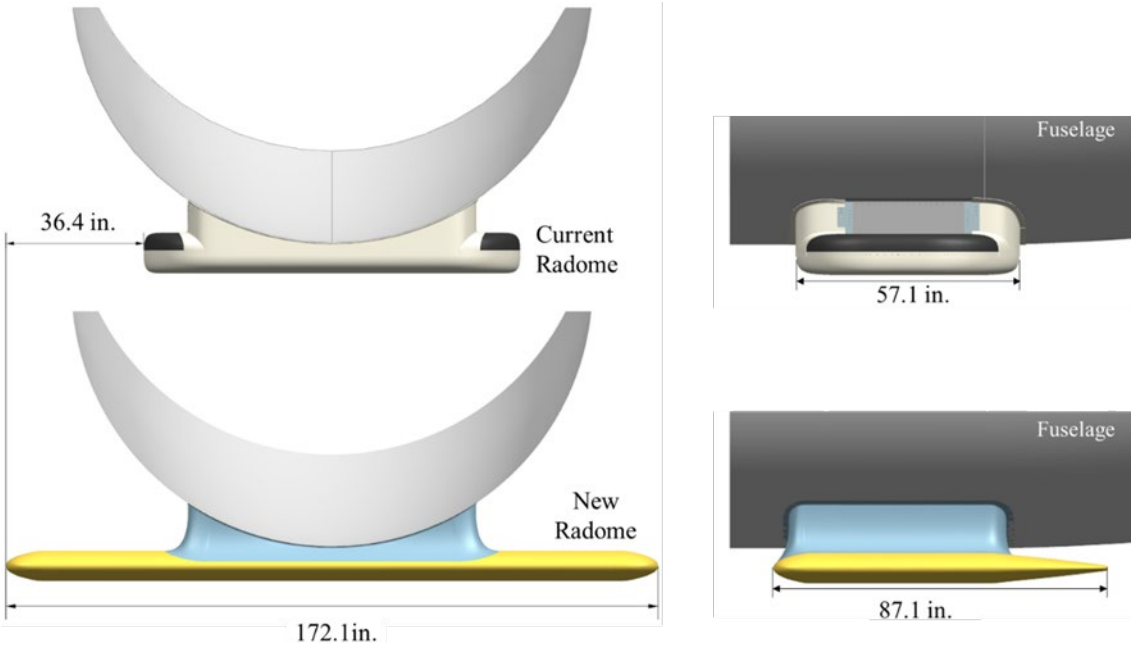

Figure 3: Current vs. New Radome. Left: Front View. Right: Side View. Scale 1:50.

A revised version of the 3D CFD pressure loadings of the current radome were used in the preliminary structural sizing of the new radome. These loads were used to estimate the amount of structure required to sustain such loading and to help define if the current geometry is structurally feasible. To do this, the loads were applied to regions on the new radome that are similar to the current radome. The analyses resulted in a preliminary radome design that is three times heavier than the current radome (1244 lb. or 564 kg to the 413 lb. or 187 kg from Ref. 6), and may be heavier since structural failure is predicted in various regions which are further discussed in Chapter 2.

The CFD loads of the current radome are not fully applicable to all locations on the new radome, as for example in the trailing edge where the loading is expected to be low. Three dimensional CFD analyses for the new radome geometry would provide accurate loads; however, these analyses are expensive and analyzing multiple concepts is cost prohibitive. Hence, two dimensional aerodynamic analyses were run on different versions of the new radome (with a long trailing edge and with a blunt trailing edge) to help define the radome shape. The results of these analyses are explained in detail in Chapter 2.2.

The 2D aerodynamic analysis results for the new radome concepts show excessive wave drag, and large undesired vortex shedding at the trailing edge for the concept with a blunt trailing edge. Due to unsatisfactory aerodynamic and structural results, the author investigates methods to reduce both aerodynamic and structural loading while minimizing negative effects on the antenna performance.

1.3. Description and Organization of Solution Strategies

The UWB MCoRDS radar system requires a ground plane to improve the performance of the system in ice sounding applications (improve antenna gain and isolate the antennas from undesired reflections). Figure 4 shows a schematic of the position of the ground plane and the antennas inside the radome.

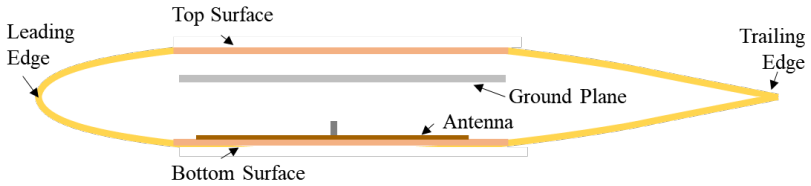

Figure 4: Schematic of Ground Plane and Antenna inside Radome (other structural components not shown)

Electromagnetically, the ground plane distance and the shape of both the ground plane and antenna are crucial to the performance of the radar system. Hence, the radome size and shape, and the radar capability are limited by the manufacturing constraints and fabrication costs. Aerodynamic, structural, electromagnetic and manufacturing aspects of the design are evaluated while investigating different solution strategies to the complications described in the previous sub-section. The different solution strategies include:

1. Reducing the depth of the radome to minimize drag at high speeds and high angle of attack. This can result in negative effects in antenna performance as the ground plane is brought closer to the antenna. Detailed description of the electromagnetic results are presented in Chapter 2.3.
2. Maintaining the curvature of the airfoil rather than flattening at the chordwise location of the antenna in both upper and lower surfaces. This can result in negative effects in antenna performance (reduced transmissivity, distortions to the beam pattern and reductions in realized gain) depending on the amount of curvature added. Two different studies are performed:
    a. Conforming the ground plane to an airfoil shape. In this case, the top surface of the radome also becomes the ground plane which can allow reducing the radome depth significantly. Electromagnetic analyses and results are presented in in Chapter 4.
    b. Conforming the antenna to the shape of an airfoil suitable for transonic flight speeds. For this case, the radome maintains the airfoil shape at all sections which can allow reducing wave drag significantly. Aerodynamic results are included in Chapter 5. Electromagnetic simulation and experimental results are included in Chapter 6 and Chapter 7 respectively.

All electromagnetic results are finally assessed with respect to a radar array application rather than just single antenna performance using the concepts explained in Chapter 8. Conclusions and recommendations considering all aspects of the design of the radome are presented in Chapter 9.

The studies presented in this thesis assess methods intended to reduce the aerodynamic loadings to enable a larger array, and thus enable future science missions with enhanced electromagnetic capability. A final detailed structural design has not been performed, nor has the airworthy hardware been manufactured and tested, since that takes considerable time and funding. However, sufficient theoretical and experimental studies are presented herein to verify the aerodynamic and electromagnetic feasibility of this concept for future missions. These are expected to significantly improve the structural performance of the radome by reducing the aerodynamic loading by enabling thinner sections where able, and deeper sections where required.

2. Background Studies and Literature Review

This chapter presents background structural and aerodynamic studies to assess the feasibility of an eight element array installation on the DC-8 using the new radome design presented in the previous chapter. Sub-chapter 2.1 presents a rough order of magnitude sizing of a new radome using the current radome aerodynamic loads. Sub-chapter 2.2 presents two dimensional aerodynamic results of the cross-section shape of the same new radome. The results of both sections are used to define the need and approach for further tailoring of the radome.

2.1. Rough Order of Magnitude Sizing of a Radome to House an Eight Element Ultrawideband MCoRDS Radar Array

A preliminary structural analysis was performed on the new fairing concept shown in the previous chapter to rapidly evaluate the feasibility of the new radome when integrated onto the DC-8. The structure is evaluated using the factors of safety shown in Table 1 which are recommended by NASA for this airframe (Ref. 7). These are the same as those used in the design of the current radome. A summary of the results, design and assumptions is provided below.

Table 1: Factors of Safety (Ref. 7)

Material	FS
Composite	3
Metal	2.25
Fitting Factor to Allowables	1.11

2.1.1. Design Results Summary

The author performed a preliminary structural analysis using MSC Patran 2018 and Nastran 2018.2 finite element analysis software (Ref. 8). This resulted in a new radome with 1244 lb. or 564 kg weight, which is three times the weight of the current radome (413 lb. or 187 kg from Ref. 6). Table 2 presents the critical margins of safety in components of the new radome. Negative or close to zero margins of safety are distinguished with blue letters. These results indicate structural failure in various regions of the radome: leading edge, trailing edge, and main ribs and spars. The analysis has not been continued as this is believed to be of sufficient rough order of magnitude sizing to

address viability of this concept. Large stresses are caused by the large applied loads at the leading and trailing edges which cause the radome to rotate clockwise about the stiff nadir sill attachment as shown in Figure 5. High loads at the upper skin also cause the end tips of the structure to rotate upwards while the center section experiences almost no deformation due to the high stiffness of the nadir sill as shown in Figure 6. This induces high tension loads primarily on the ribs and main spars.

High bolt loads are also induced as shown by the 0.004 margin of safety for the fasteners at the outboard attachment. However, the margin of safety can be increased with the use of NAS fasteners. All bearing margins of safety for metal-to-metal and metal-to-composite structures are higher than 0.13.

Table 2: Critical Margins of Safety

Structure	Critical Mode	MS
Bottom Skin	Longitudinal Compression	0.64
Fairing	Transverse Tension	0.01
Ground Plane	Maximum Principal Stress	1.62
Leading Edge	Core Shear	-0.13
Trailing Edge	Core Shear	0.76
Trailing Edge Ribs	Longitudinal Tension	-0.18
Trailing Edge Spar	Transverse Tension	1.30
Aft Inserts	Transverse Tension	-0.02
Upper Skin	Maximum Principal Stress	0.75
Fairing Ribs	Maximum Combined Stress	0.83
Fuselage Supports	Maximum Principal Stress	0.31
Main Ribs	Transverse Tension	-0.01
Main Spars-Flange	Longitudinal Tension	-0.05
Main Spars-Flange	Transverse Tension	-0.10
Main Spars-Doubler	Maximum Principal Stress	-0.09
Ground Plane Supports	Maximum Principal Stress	0.61
Radome End Tips	Core Shear	0.46
Outboard Attachment Fasteners-AN3	Combined Shear and Tension	0.004

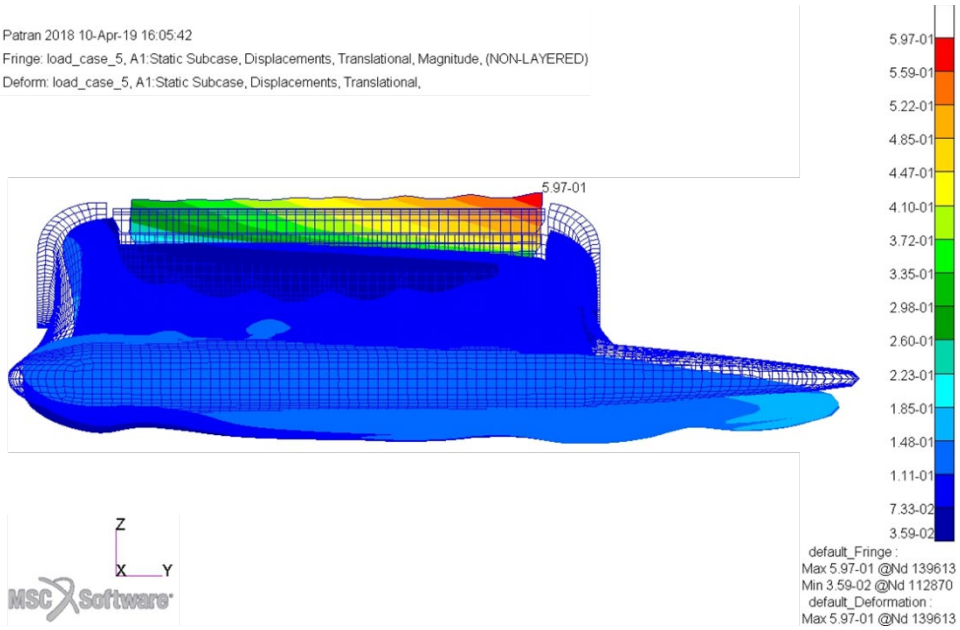

Figure 5: Side View of Total Displacement. Radome Rotates Clockwise (in.)

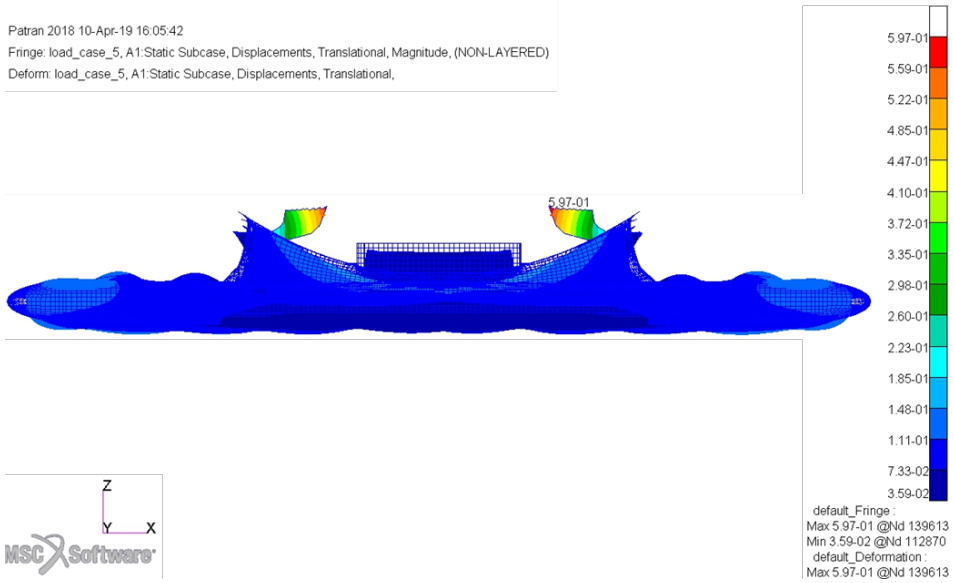

Figure 6: Front View of Total Displacement. Tip Ends Rotate Upwards Towards Center (in.)

2.1.2. Geometry Modeled

The main dimensions of the new radome compared to the current radome are shown in Table 3. The new radome is larger in span and chord, but is shorter than the current radome since the ground plane distance for the UWB MCoRDS is smaller than for the antennas used in the current radome.

Table 3: New Radome vs. Current Radome Dimensions

	New Radome		Current Radome		% Difference
Total Weight	1244 lbf	564 kg	413 lbf	187 kg	201%
Span	172.1 in.	4.37 m	99.3 in.	2.52 m	73%
Chord	87.1 in.	2.21 m	57.1 in.	1.45 m	53%
Max. Depth	8 in.	0.2 m	10.8 in.	0.27 m	-26%

The span of the new radome is defined by the 143.5 in. (3.64 m) span of the 8-element MCoRDS array shown in Figure 7, and the span of the port and starboard radome tips. The chord is driven by the 32 in. (0.81 m) length of the antenna and the curvature of the airfoil used to model the radome. The depth is defined by both the ground plane distance and by the airfoil geometry to accommodate the length of the antenna. The current radome has a thickness to chord ratio (t/c) of 18.9% with blunt leading and trailing edges, and has successfully flown multiple times. Hence, the symmetrical and sub-sonic NACA 0010 (Ref. 9) was selected for the new radome design because, once scaled to accommodate all structural and electromagnetic components, it resulted in the smallest profile depth from this group of airfoils. This was also selected to allow the section where the antenna is placed to remain as flat as possible.

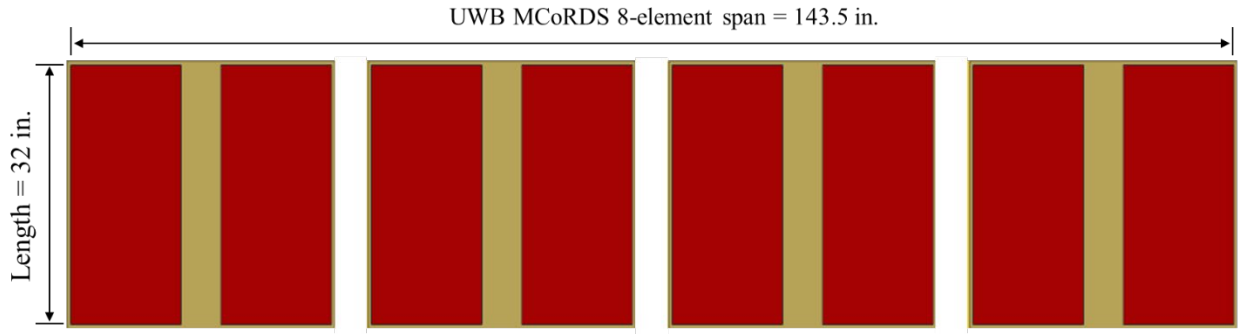

Figure 7: Bottom View of UWB MCoRDS Arrangement (not to scale)

The main components of the new radome design are shown in Figure 8. The antennas could either be placed outside or embedded in the flat bottom skin. To reduce adverse effects on the antenna array performance, spars were placed in front and aft of the antennas instead of through the center of the structure. Similarly, main ribs were placed in between antenna elements rather than directly on top.

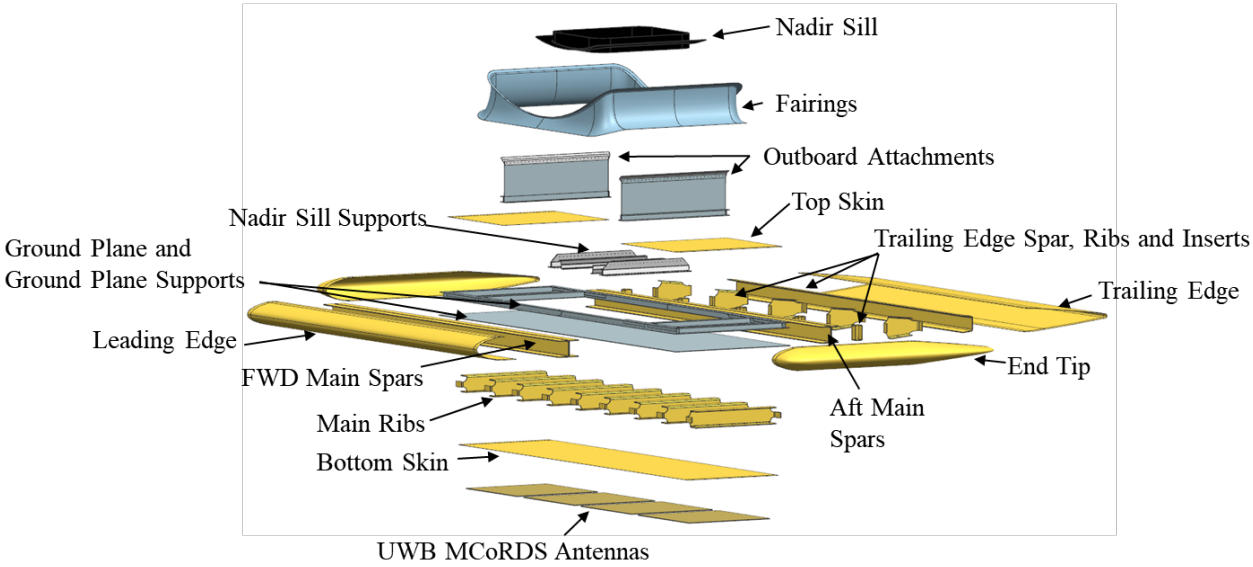

Figure 8: Exploded View of New Radome Components

The ground plane size had been defined based on previous installations of the UWB MCoRDS antennas, and is attached to the top surface of the spars and ribs. Supports on the ground plane help attach the leading edge, end tips, trailing edge and top skin to the structure. The trailing edge is stiffened with a trailing edge spar and ribs. These also serve to connect the trailing edge to the main body and provide a load path.

The same nadir sill supports and similar outboard attachments compared to those in the current radome are used. These are protected from the environment with the fairings that are designed to accommodate the curvature of the aircraft and of the radome. Fairing ribs, leading edge ribs, trailing edge ribs aft of the trailing edge spar, and additional ground plane-to-top skin stiffeners were added in the finite element model due to large displacements.

2.1.3. Critical Flight Conditions

The structural analyses were performed with similar external loads as those used for the current radome. Some external loads used in the analysis of the current radome were overly conservative based on the feedback of the lead flight test engineer for the DC-8 (Ref. 5). The current radome loads were revised based on this and on further examination of Reference 7. Table 4 presents the resulting load conditions for the new and the current radomes.

Table 4: Load Conditions

		New Radome					Current Radome				
Case	**Description**	**q (psf)**	**T (°F)**	**α (°)**	**Altitude (k ft)**	**Speed (kts)**	**q (psf)**	**T (°F)**	**α (°)**	**Altitude (k ft)**	**Speed (kts)**
1	Airplane High Speed Dive Flight Condition	261	~	3.5	15	350	572	~	5	Sea level	406
2	Airplane High Speed Dive with Worst Temperature Differential Flight Condition	261	-83	3.5	15	350	572	-65	5	Sea level	406
3	Airplane Cruise with Lowerst Temperature Flight Condition	235	-105	~	35	473	235	-105	~	35	473
4	Airplane Highest Temperature at Highest Appropriate Dynamic Pressure Flight Condition	399	122	~	5	370	370	122	~	5	356
5	Airplane at Maximum Aerodynamic Loads, Side Slip and Lateral Inertial Load Flight Condition β=5°	399	-76	~	20	470	470	-76	~	20	510.5

All cases include gust maneuvering load factors of Nx (drag direction)= 2.5 and Nz (lift direction) = 4, and inertial loads of -4g vertical and 1.5g rearwards.

The most critical conditions for the design of the current radome were load cases 1 and 2, which are highlighted in green above. These used a 572 psf maximum dynamic pressure at sea level which is specified in Reference 7, and a conservative 5°angle of attack. However, the flight test engineer indicated that the worst case dynamic pressure could have been limited to a 350kts, 15,000 ft (4.57 km) altitude and 3.5° angle of attack which results in q_{max} = 261 psf (Ref. 5). By making this change in the load conditions, load case 5, highlighted in blue above, becomes the most critical for the new radome design.

The dynamic pressure of load case 5 is then used to scale the pressure loads applied to the finite element model. The pressures were scaled with a 0.69 factor which equals to q_{max} of load case 5 for the new radome divided by q_{max} of load case 1 for the current radome (399/572). This operation

can be performed since all current radome pressures are proportional to q_{max} = 572 psf. The resulting pressures as shown in Table 5.

Table 5: New vs. Current Pressure Loadings

Current			New		
Region	**Color**	**Pressure(psi)**	**Region**	**Color**	**Pressure(psi)**
Front Surface	Yellow	6.2	Front Surface of Fairing	Red	4.34
Sides	Light Blue	-4.9	Sides of Fairing	Blue	-3.43
Back Surface	Dark Green	-2.4	Aft Surface of Fairing	Light Blue	-1.68
Front Corners	Yellow	-5.85	LE Top	Light Orange	-4.10
Back Corners	Light Green	-6.82	TE and Radome End Tips Top	Orange	-4.77
Side Corners	Red	-8.58	Side Corners	Red	-6.01
Shoulder Surfaces	Light Green	-7.3	Top Skin	Orange	-5.11
Bottom Flat Surface	Light Green	-6.67	Bottom Flat Surface	Light Orange	-4.67
Bottom Curved Perimeter	Red	-8.3	Bottom Curved Perimeter	Red	-5.81
Front Surface	Pink	7.5	Front Surface	Blue	5.25
Sides	Blue	-5	Sides	Yellow	-3.50

The pressure loadings presented above were applied to the new radome at similar regions as the current radome. Figure 9, Figure 10 and Figure 11 show color maps of the applied pressures on both the current and new radomes that correspond to the values presented above.

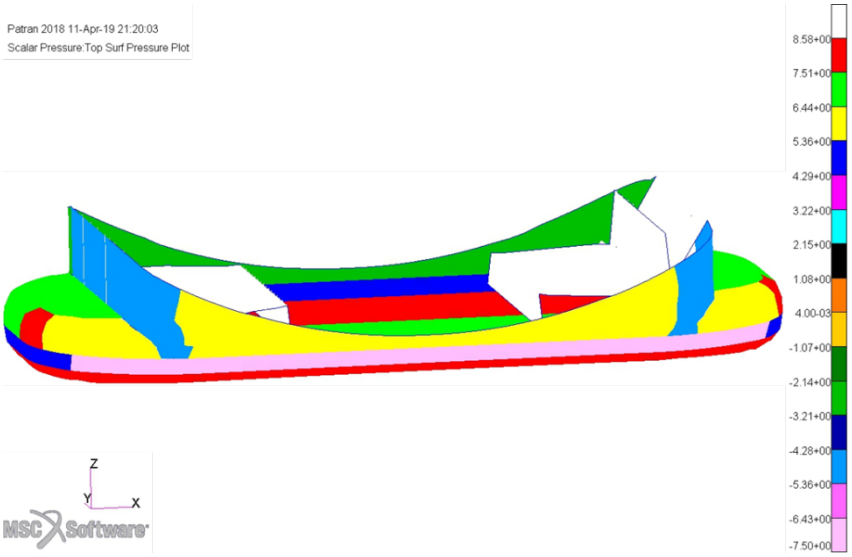

Figure 9: Pressure Map on Current Radome

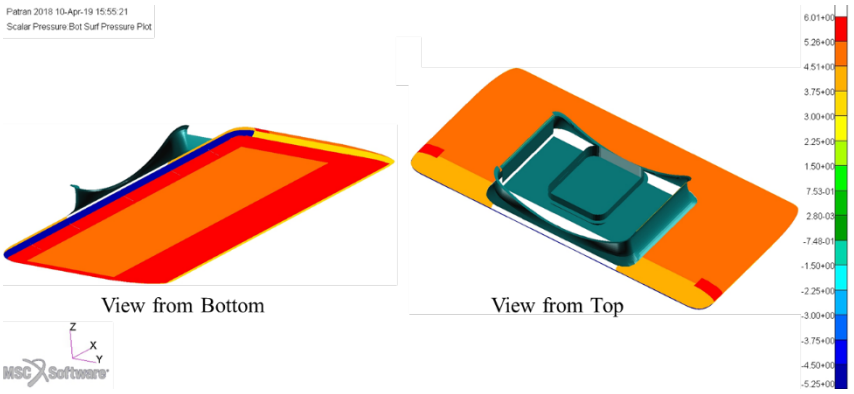

Figure 10: Pressure Map on New Radome Top and Bottom Surfaces

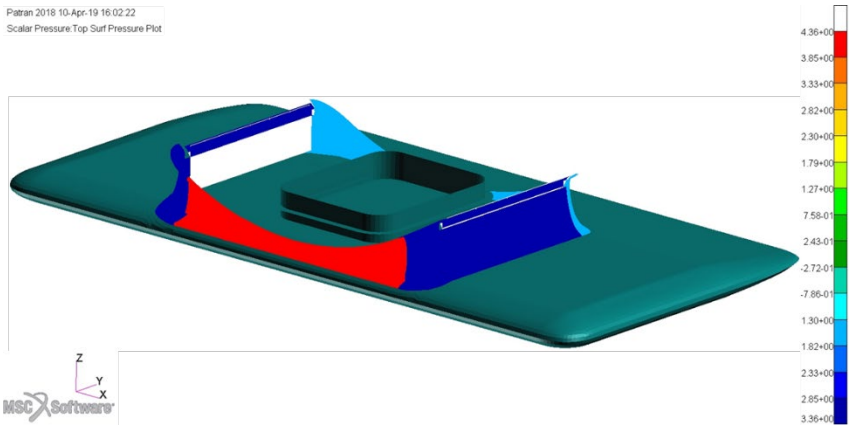

Figure 11: Pressure Map on New Radome Fairing and Fuselage Supports

This mapping of pressures to similar regions may not be fully applicable since the current radome has taller blunt leading and trailing edges which could result in higher aerodynamic loads than those of the new radome. The new radome has a smaller depth and a long trailing edge that gently tapers down in thickness. Thus, the pressure loadings on the new radome in these regions could be smaller than those applied to the model. On the other hand, the span of the new radome is larger than the span of the current radome which could result in higher loading at the upper skin and end tips depending on how influential the reduction of the depth of the new radome is.

2.1.4. Manufacturing Considerations

All components of the new radome shown in the exploded view have 8HS weave S2 glass epoxy cloth properties with the exception of the ground plane, top skin, fairing ribs, outboard and nadir

sill supports, and ground plane stiffeners which have 2024-T3 or 2024-T351 metal properties. Specific locations on the bottom skin, leading and trailing edges and fairing have sandwich type layups with Rohacell 71 IG-F foam core. The bottom skin has the maximum number of fiberglass plies (38), the leading edge has the maximum core thickness (1in. or 25.4 mm), and the nadir sill supports have the maximum metal thickness (0.25 in. or 6.35 mm). These thicknesses were obtained by tailoring the position of fiberglass and metallic reinforcements, and the location of sandwich type regions to avoid interference with ribs and spars. Thus, the resulting structure poses manufacturing challenges due to the highly specific locations of multiple components, the large number of custom tools required to fabricate fiberglass components, and the large size of the radome.

Table 6: Summary of New Radome Components

Components that require custom tools	**No. of Custom Tools**
Fairing (fwd and aft)	2
Leading Edge	1
Trailing Edge	1
Trailing Edge Ribs	1
Trailing Edge Spar	1
Aft Inserts	1
Main Ribs	1
Main Spars	1
Radome End Tips (port and starboard)	2
Total	*11*
Components that require machining or bending sheet metal	
Fairing Ribs	
Fuselage Supports	
Leading Edge Ribs	
Off-the-shelf Components	
Ground Plane	
Upper Skin	
Ground Plane Supports	
Fairing L-brackets	
Doublers	
Fasteners	

Table 6 provides a summary of the components that need custom tools to be fabricated, components that need machining or bending sheet metal, and off-the-shelf items. Manufacturing this number of custom tools and large amounts of metal machining can be cost prohibitive and

should be taken into account for the final design of the radome if the project continues to full scale production.

The aerodynamic pressure loads transferred from the current radome design and used in the preliminary structural analysis of the new radome result in a structure that is three times heavier. However, the stiffened and heavier structure still shows negative margins of safety and requires a large number of custom made components as shown above. Therefore, aerodynamic analyses on the new radome are required to unequivocally determine the feasibility of the design with eight UWB MCoRDS antenna elements.

The following sub-chapter presents two-dimensional aerodynamic analysis results performed on the new radome shape and on a blunt trailing edge variation of this shape. These are analyzed in detail and compared to the current radome aerodynamic results.

2.2. Aerodynamic Studies of Cross-Section Profiles with Flat Top and Bottom Regions but with Varying Trailing Edge Shapes

Two dimensional aerodynamic studies were performed on the shape analyzed in the previous sub-chapter to determine if the pressure loads being used for structural sizing were appropriate for the new design. A thinner shape with longer trailing edge could result in lower aerodynamic and structural loads which could allow reducing the weight of the structure.

A second cross-sectional shape with a deeper and shorter trailing edge was also analyzed under the assumption that a shorter trailing edge decreases the radome weight, is easier to manufacture, and can reduce critical stresses and bolt loads. This shape also facilitates manufacturing since the chord of the first shape does not fit horizontally in the oven of the KU Composite Laboratory, and would thus need to be tilted at an angle during cure with the support of an additional fixture. This second shape was evaluated for changes in aerodynamic performance compared to the first shape. Figure 12 presents the two shapes analyzed.

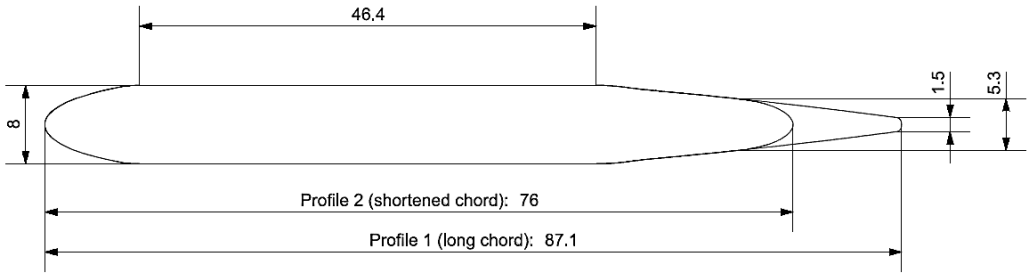

Figure 12: Profiles Used for 2D Aerodynamic Analyses. Scale 1:16 (inches).

The 2D aerodynamic studies were performed in collaboration with DARcorporation using Siemens STAR-CCM+ v.13.02.011 software. These were done with the assumptions listed below following the requirements in References 5 and 7. The assumptions are unchanged with exception of the AoA which is reduced from 5° to 3.5° based on the feedback of the lead flight test engineer for the DC-8, who noted that the worst case dynamic pressure and high Mach analysis could be limited to 3.5° AoA (Ref. 5). This was not implemented in the current radome because the design had already been conservatively done with an AoA of 5°; however, applying this change is crucial to generating a feasible design for a radome with longer span.

- Condition: Cruise at altitude = 30,000 ft (9.14 km);
- Mach = 0.8 (q = 282 psf);
- Highest AoA = 3.5°.

2.2.1. 2D Pressure Coefficient Distributions

Figure 13 and Figure 14 show the 2D pressure coefficient distributions over profile 1 resultant of the analysis conditions previously stated. These show that a significant change in pressure occurs at the transition of the leading edge to the flat top region. This also occurs on both sides of the flat bottom region, but with a smaller magnitude.

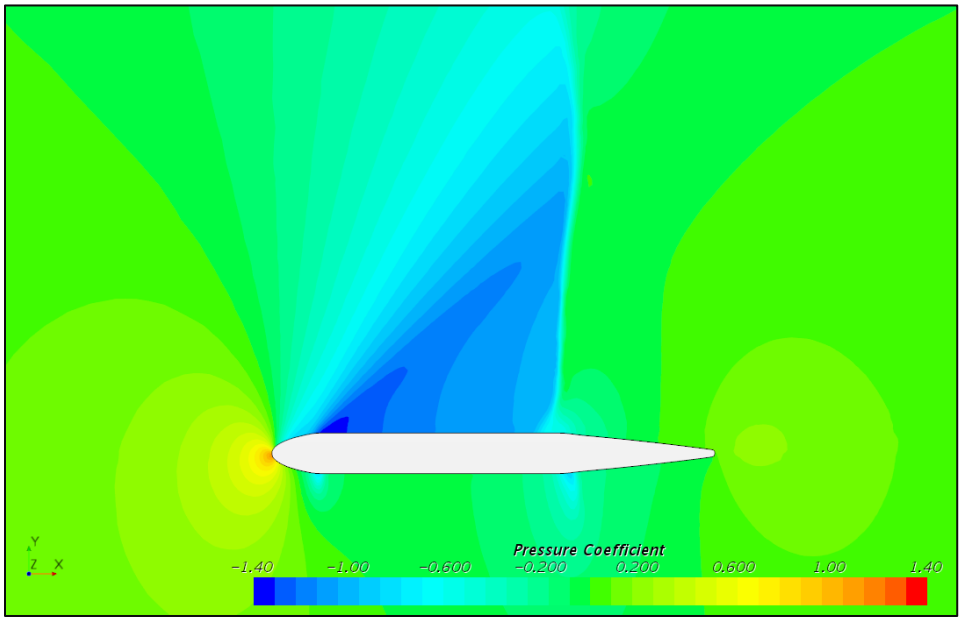

Figure 13: Snapshot of 2D Pressure Coefficient over Profile 1 (long chord) (Ref. 10)

Figure 14 shows the pressure coefficient values along the chord for the top and bottom regions of profile 1. This shows changes in pressure coefficient of 0.4-0.8 units at the transitions between flat and curved regions. However, at the trailing edge region (approximately 1.6-2.2 m or 5.25-7.2 ft.) the pressure distribution is more uniform and the difference between top and bottom regions is small. This is a favorable result since large differences between top and bottom trailing edge regions induce a moment (rotation of the trailing edge) which can negatively increase stresses in the main-to-trailing edge structure.

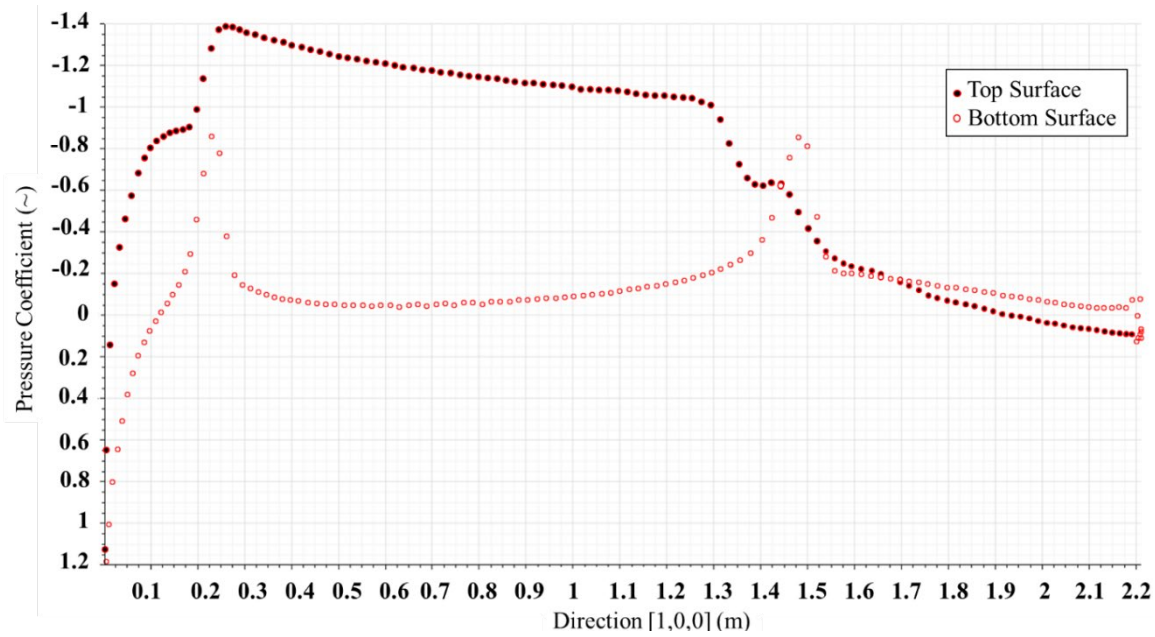

Figure 14: 2D Pressure Distribution over Profile 1 (long chord) (Ref. 10)

Figure 15 and Figure 16 show the two dimensional pressure coefficient distributions for profile 2 (shortened chord and deeper trailing edge).

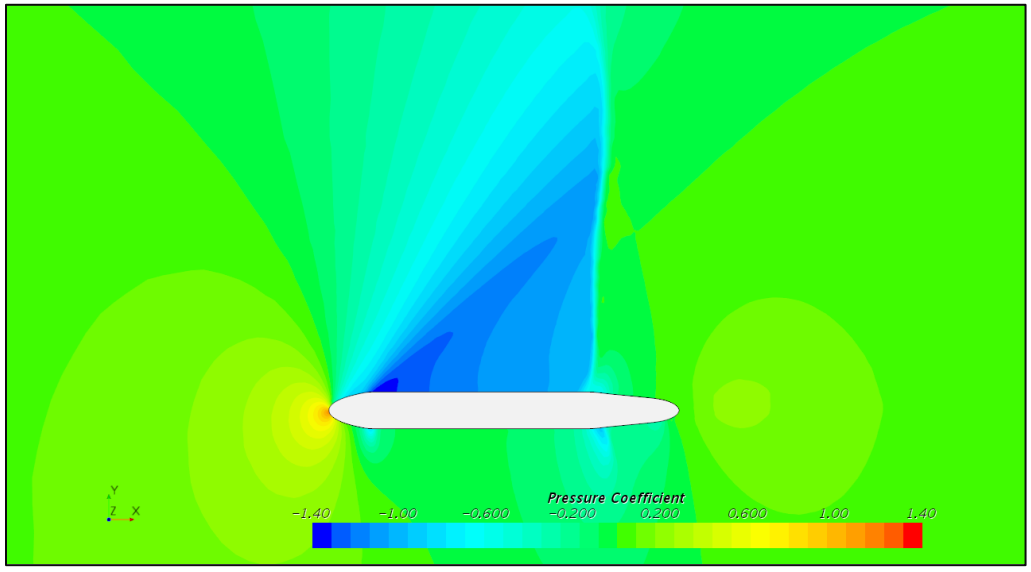

Figure 15: Snapshot of 2D Pressure Coefficient over Profile 2 (shortened chord) (Ref. 10)

The results are similar to the results for profile 1 up to the transition from flat regions to the trailing edge (approximately 1.4 m or 4.6 ft from the leading edge). Aft of this location, the peak of the

transition from flat to trailing edge at the bottom increases in magnitude, and the pressure coefficient differential between bottom and top regions at the trailing edge also increases (mainly between the 1.6-1.88 m or 5.25-6.17 ft.). This is a negative change as it can induce a higher rotation of the trailing edge and higher stresses. The sudden and large changes in magnitude along the chord are also undesired aerodynamic characteristics.

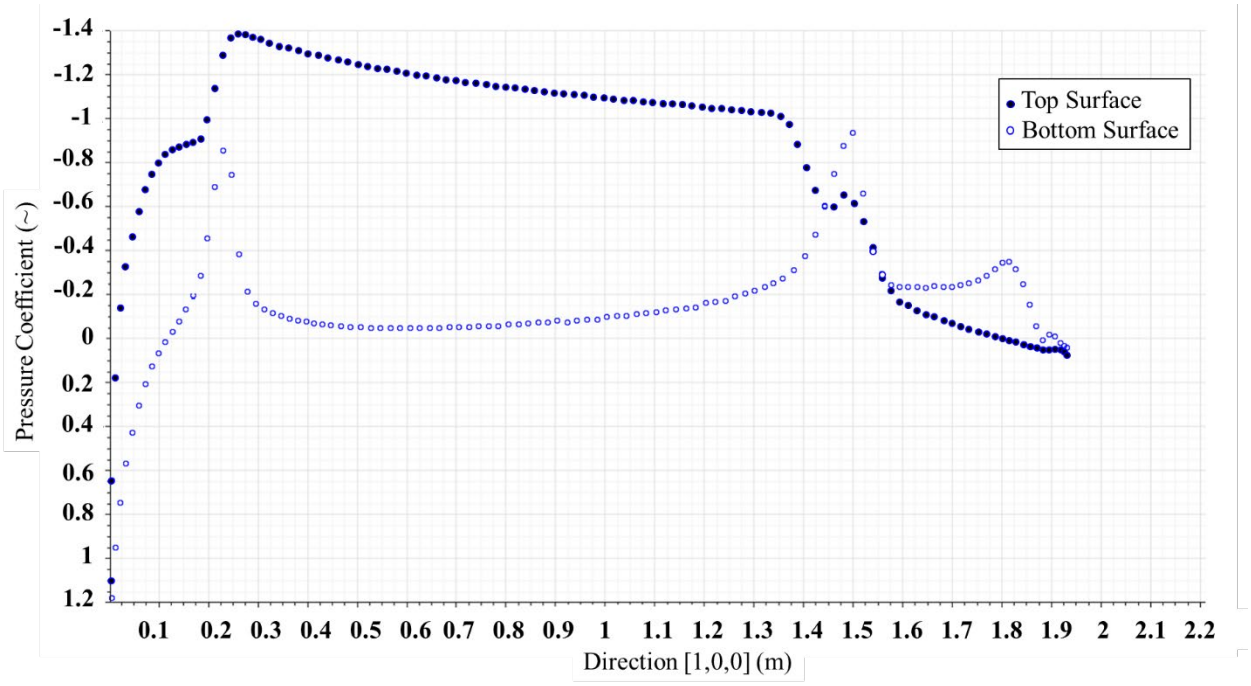

Figure 16: 2D Pressure Distribution on Profile 2 (shortened chord and thicker TE). (Ref. 10)

2.2.2. Mach Number of 2D Profiles

The Mach number was also evaluated for profiles 1 and 2. Figure 17 shows the Mach number plot for profile 1. This shape generates a maximum Mach number of 1.5 right after the transition from the leading edge to the top flat region. In addition to this strong shockwave, smaller shocks are generated at the transition regions on both sides of the bottom flat region.

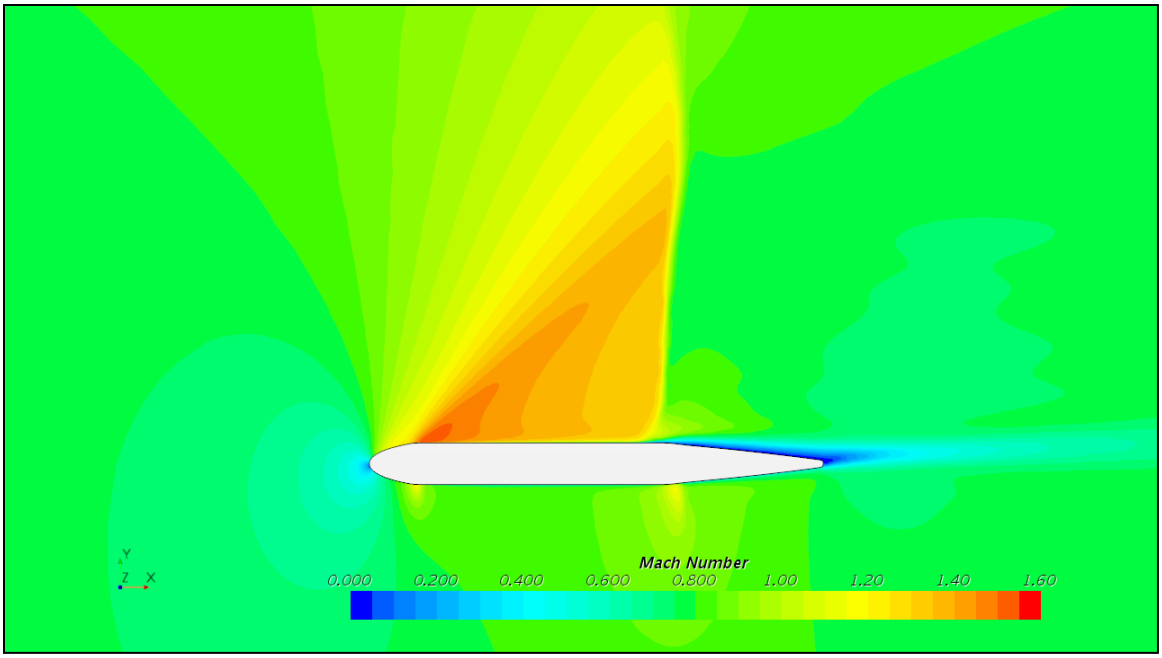

Figure 17: Snapshot of Mach Number of Profile 1 (Ref. 10)

The trailing edge is sufficiently long and thin to not cause any shedding vortices as shown in Figure 18.

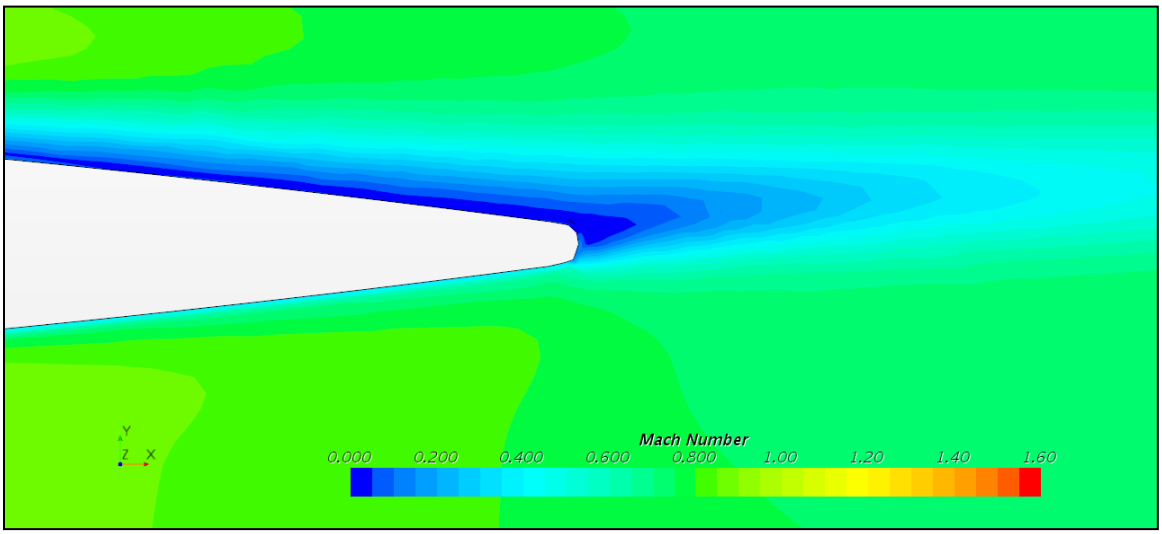

Figure 18: Snapshot of Mach Number of Trailing edge of Profile 1 (Ref. 10)

Figure 19 shows the Mach number plot for profile 2. The intensity and location of the shockwaves are equal to those generated by profile 1, with the exception of the trailing edge region.

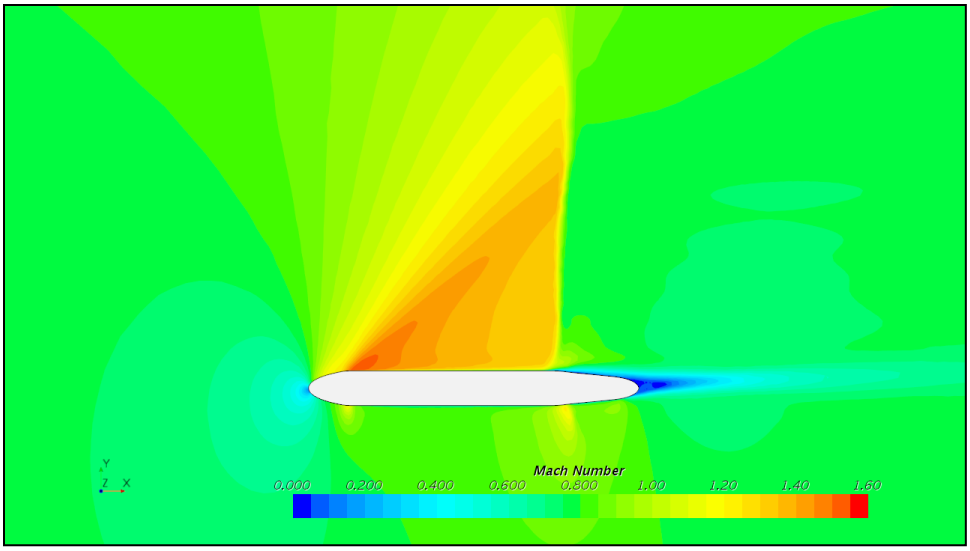

Figure 19: Snapshot of Mach Number of Profile 2 (Ref. 10)

Profile 2 generates inconsistent turbulent pockets aft of the trailing edge which results in possible shedding vortices as shown in Figure 20. This occurs due to the large thickness of the trailing edge and how rapidly the thickness of the profile tapers down. Profile 1 minimizes the thick end with the longer trailing edge, hence it eliminates the chances of vortex shedding (Ref. 10). An additional transient analysis would be required to determine the shedding frequency which is significant in structural sizing.

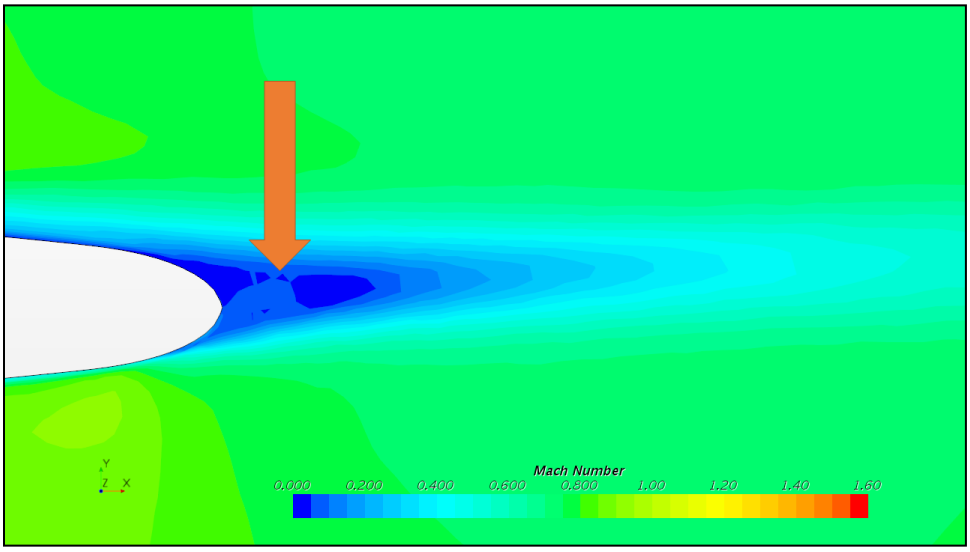

Figure 20: Snapshot of Mach Number of Trailing Edge of Profile 2 (Ref. 10)

2.2.3. Drag Coefficient

The aerodynamic analyses of the two profiles were also performed to determine the amount of drag produced, how the two profiles compare to each other, and also in comparison to the current radome. This section presents a comparison between profile 1 and profile 2 as shown in Table 7.

Table 7. 2D Drag Coefficient Comparison for Profiles 1 and 2 (Ref. 10)

	Profile 1	**Profile 2**
	Long TE	Shortened TE
Pressure	0.120	0.122
Shear	0.009	0.009
Net	0.129	0.131

At Mach 0.8 in combination with the blunt geometry of the leading edge of both profiles, the shockwave on the upper region is the main contributor to drag (93%) while the influence of the trailing edge length is small. This can be observed above where the pressure component of the drag coefficient only increases by 0.002 when the trailing edge is shortened (this is due to the vortex shedding).

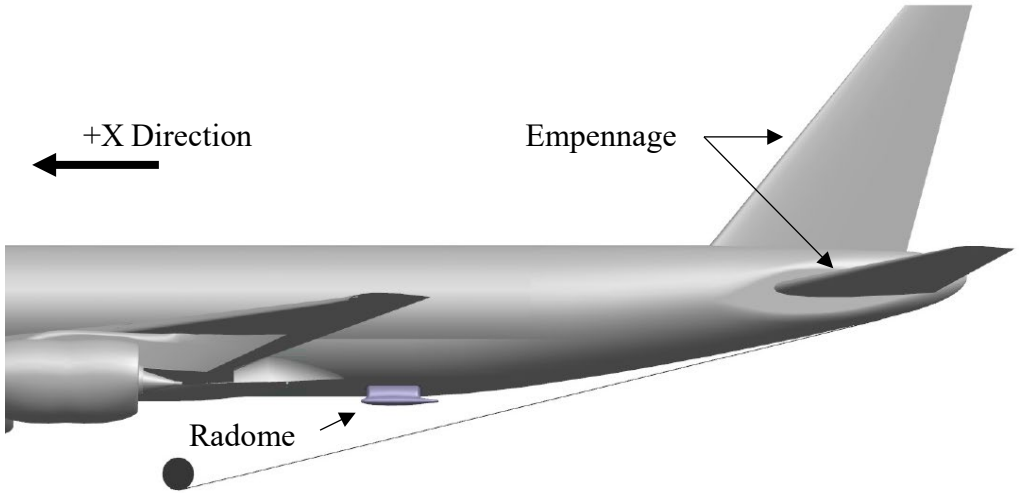

Figure 21: Side view of DC-8 with radome. Fuselage and empennage are away from the shedding vortices of the trailing edge of the radome.

Shortening the trailing edge could reduce the weight of the radome, but increases drag and could result in a vortex shedding frequency that negatively affects the radome. The effect of the vortex shedding is mainly of concern for the radome rather than for the already existing aircraft structure

since the fuselage tapers up and away from the path of the vortices, and the empennage is far away as shown in Figure 21.

2.2.4. Comparison to Current Radome Profile

Only 3D aerodynamic studies were performed on the current radome. Thus, only approximate comparisons for pressure coefficient distribution and maximum Mach number can be made between profiles 1 and 2, and the current radome profile. Available results from the 3D aerodynamic studies on the current radome were performed with the following assumptions.

- Condition: Cruise at altitude = 30,000 ft. (9.14 km);
- AoA = 0 degrees;
- Maximum Mach number = 0.8;

Figure 22 shows significant changes in pressure at the transitions between flat and curved regions. The minimum pressure coefficient observed is -1.4 which is similar to the values for profiles 1 and 2. The maximum pressure coefficient is approximately 1 which is smaller by 0.2 compared to profiles 1 and 2.

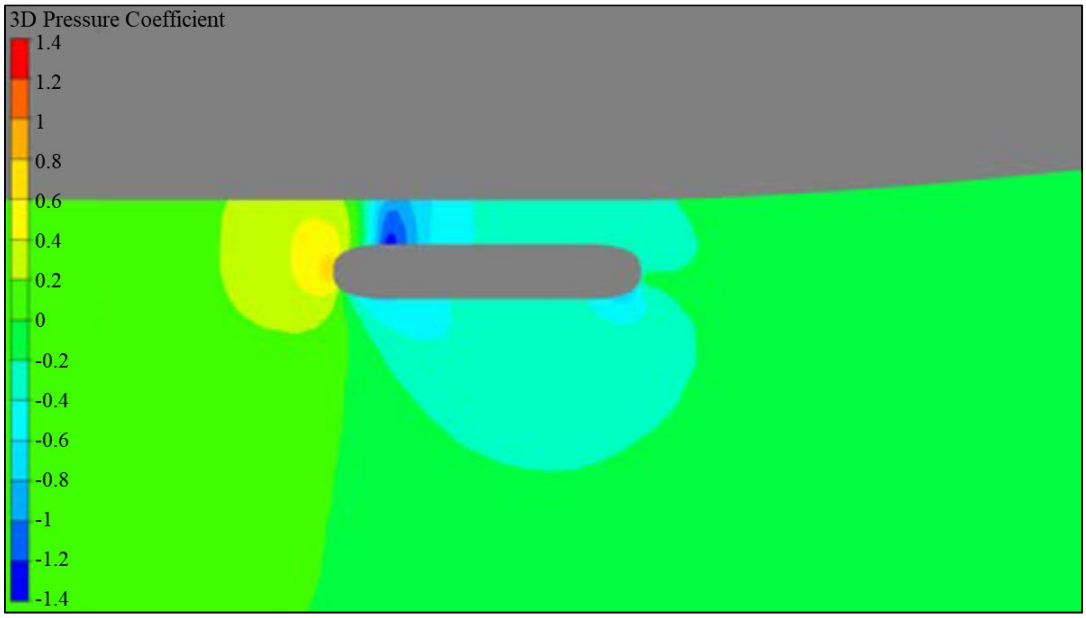

Figure 22: 3D Pressure Coefficient over Current Radome at XZ Cut Plane 2.8 ft. (0.85 m) off Centerline (Ref. 10)

Figure 23 shows supersonic flow over the top region of the current radome profile with a maximum Mach number of 1.2 after the transition of the leading edge to the top flat region. This is lower than the maximum for profiles 1 and 2 (M =1.5); however, the studies on these profiles were performed with an AoA of 3.5° which justifiably results in a higher Mach number.

The results for the current radome were obtained using Blue Ridge Numerics CFdesign v.10 software which is not as sensitive in capturing the shockwave compared to Siemens STAR-CCM+ v.13.02.011 (Ref. 10).

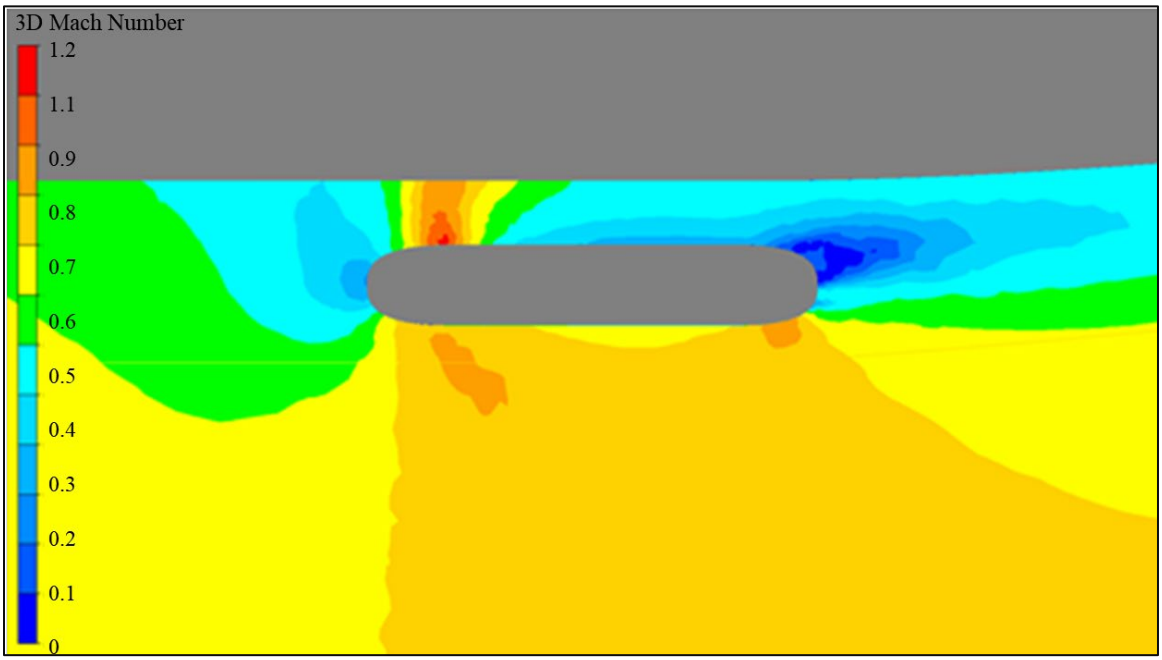

Figure 23: 3D Mach number over Current Radome at XZ Cut Plane 2.8 ft. off Centerline (Ref. 10)

2.2.5. Summary of 2D CFD Studies and Solution Strategies Discussion

Vortex shedding is important as it may excite the structure at undesired frequencies and adds one more issue to prevent during the design process. Although this can be overcome, it is preferable to avoid it by improving the shape of the radome.

As observed above, the shockwaves and Mach number distributions along both profiles are high. To reduce these, the total depth of the radome can be reduced or other aerodynamic shapes can be

used. Thus, these background studies identify that the driving parameter to allow this and future installations of larger arrays onto transonic aircraft is the magnitude of the aerodynamic loads and drag. Drag reductions are associated with geometric features like the ground plane separation distance, and the curved to flat transitions which were driven by assumptions of requiring flat sections for effective antenna performance. The following chapters address both alternatives and the corresponding antenna performance effects.

Two options are considered to reduce the total depth of the radome:

- Reduce the ground plane distance only (from antenna to ground plane). This would reduce the total radome depth by a few inches or fractions of an inch;
- Extreme reduction of depth. This approach assumes that the ground plane can also act as the top skin (essentially removes the top skin). Since the transition to flat regions are observed to cause large shock waves, the analysis is then performed for curved ground planes (assuming the ground plane takes the shape of the top region of the airfoil).

The effect of the geometry of the cross-sectional radome profile is studied in two steps:

- Include the curvature of the airfoil shape in the radome cross-section. This affects the top and bottom skin. Thus, to not disturb the shape of the airfoil, the bottom skin and the antennas would need to conform to the airfoil shape. Analyses are performed to determine the effect of curvature on the antenna performance;
- Selection of a supercritical airfoil profile that minimizes the negative effects of curvature on the antenna performance (if any), and that minimizes the length of the trailing edge for manufacturing purposes.

The improvement of the design of the outer geometry of the radome depends on:

- Ground plane distance. This limits the reduction in depth of the radome profile. Electrical equipment to feed each antenna also limits the reduction of depth as this needs to be in close proximity to each antenna and protected from the environment;

- Sensitivity of the antenna performance to curvature of antenna and of ground plane. This limits type of airfoil used and defines chord length. For example, symmetrical supercritical airfoils can have relatively flat top and bottom regions but result in large chords.

2.3. Conformal Antenna Literature Review

This section presents a summary of a literature review performed on conformal antennas. The findings are used to define the parameters to evaluate changes in antenna performance due to variations in ground plane distance and curvature, and antenna curvature. The following provides a brief overview of conformal antenna technology and a review of curvature effects on antennas and antenna arrays.

2.3.1. Definition and Overview of Conformal Antenna Technology

Conformal antennas are antennas that conform to a prescribed shape. Reference 11 states that this shape is defined by aerodynamic considerations for airborne applications, or by electromagnetics requirements to improve specific aspects of the antenna performance. In regards to the first case, aircraft carry a large number of antennas for navigation, communication, and position tracking among other reasons. The antennas can protrude from the structure and create additional drag which reduces the fuel consumption and range of the aircraft. Therefore, conforming or integrating the antennas to the existing aircraft structure is highly desirable (mainly for antennas with large apertures which are often used for remote sensing and satellite communication applications). In the second case, the application or desired capability can require a specific antenna beam shape and angular coverage, which can be controlled with the shape given to the antenna (Ref. 11).

Antennas and antenna arrays have been conformed to multiple shapes as shown in Figure 24. These include cylinders, cones, spheres, and others as shown below. Ref. 11 states that the shape to which the antenna conforms would ideally be a smooth curved surface, but as an alternative the surface can also consist of smaller planar facets which can each contain a few or several radiators.

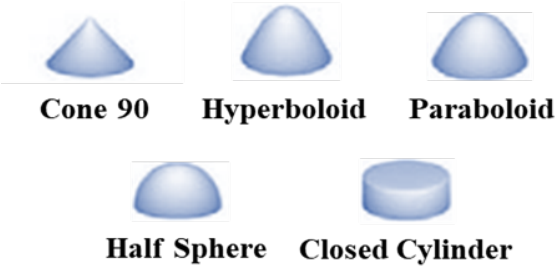

Figure 24: Shapes for Conformal Antennas and Antenna Arrays (Ref. 11)

Although significant progress on analysis and design of conformal antennas has been made in the last years, more development is needed to obtain higher understanding of the performance of antennas on curved surfaces (Ref. 11-12). General observations of conformal antennas by Ref.11-15 indicate that these provide the advantage of increasing the field of view compared to planar antennas.

The geometry and design complexity of the antenna define the type of analysis technique that can be used to determine its electromagnetic properties. There exist various different methods for analysis, some of which are only applicable to specific shapes. Ref. 11 generally defines that analysis methods for conformal antennas can be classified based on two shapes: electrically large and electrically small surfaces. These are defined in accordance with the frequency of interest, the size of the antenna, and the bandwidth. Despite relatively simple mathematical expressions exist for specific antenna designs, complex shapes require more powerful and capable techniques such as the finite element methods (FEM) which solve boundary value problems. For example, the commercial ANSYS HFSS finite element software is recommended to study conformal antennas by Ref. 11.

2.3.2. Review of Curvature Effects on Single patch Antennas and on Antenna Arrays

Reference 13 presents results associated with curving a rectangular patch antenna (one of the most common types of microstrip antennas) that is placed in two different types of dielectrics and that were selected such that the antenna has a 2.45 GHz center frequency. The paper studies the effects on the antenna performance by curving the antenna to various circular and elliptical shapes. In general, it is observed that circular curvatures improve the radiation efficiency (relates to gain), broaden the main beam width, and help on suppressing the back lobes. However, the resonant frequency is detuned randomly and the return loss degrades as the circumferential coverage (higher curvature) is increased.

Because of the resulting increase in the main beam width due to curvature, it is stated that curvature is mostly beneficial to systems that require greater coverage area rather than range. However, for large antenna arrays such as the one addressed in this thesis, the widening of the main beam of a single antenna is not expected to have significant effect on the array results due to the larger

influence of the number of elements in the directivity of the main beam. Additionally, Ref. 13 indicates that the magnitude and frequency range of the changes due to curvature are dependent on the substrate material properties.

Reference 14 presents theoretical and experimental results performed on a rectangular patch antenna with an approximate 3GHz resonant frequency. Contrary to Ref. 13, Ref. 14 indicates that conforming the patch antenna to the surface of a cylinder as shown in Figure 25 does not change the resonant frequency. For example, it is shown that a patch antenna conformed to a cylinder of 5 cm radius has the same resonant frequency as a cylinder with infinitely large radius (flat surface), despite that the experimental results show a lower frequency than theoretical results (3.17 GHz and 3.232 GHz respectively). However, it does support the finding that the pattern broadens with curvature.

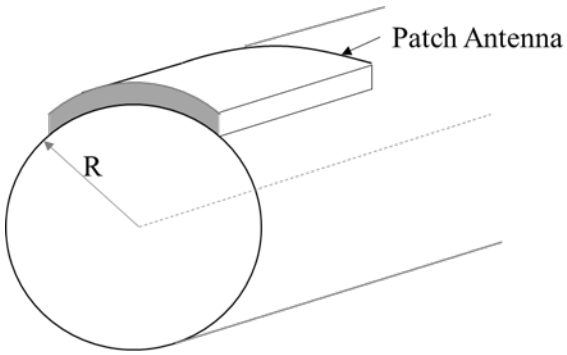

Figure 25: Rectangular Patch Antenna Conformed to a Cylinder (Ref. 14)

Reference 15 performs theoretical and experimental studies on a linear antenna array to evaluate methods that allow increasing its adaptive beam forming capabilities. The publication states that radiation patterns of phased arrays can have high efficiency if the side lobes are low and the main beam is narrow (higher signal to noise ratio). However, the gain is degraded when the main beam is steered from boresight and curving the antenna array can be helpful to maintain the same gain.

The half power beam width (HPBW), side lobe level (SLL) and gain are performance parameters used in the study of different shapes to evaluate the impact on adaptive beam forming capability of the array. Ref. 15 shows that by curving the array the main beam width is widened (which is in accordance with the general findings from other sources), the side lobe levels increase, but also

that the beam can be steered up to 70 degrees (12 degrees more than the planar array) from boresight with less than 10% degradations in gain.

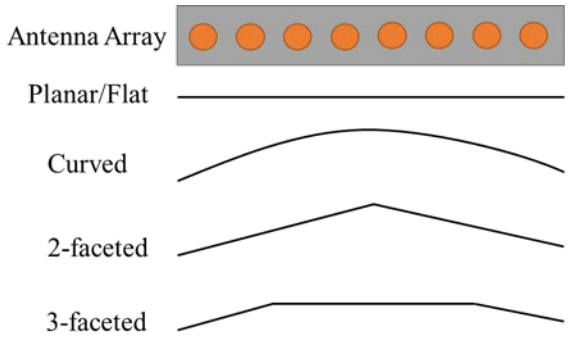

Figure 26: Linear Antenna Array Conformed to Various Shapes (Ref. 15)

The authors of Ref. 15 also studied using two and three faceted surfaces as shown in Figure 26. These result in increased performance compared to the flat array and smaller increase in HPBW and SLL than the curved array. However, the curved array provides the highest capability of steering. Hence, it is concluded by Ref. 15 that conforming the array to a curved or multifaceted surface is best suited for applications that require wide angle scanning applications due to low main beam degradation and reduced mutual coupling when steering the beam. However, flat arrays are preferred if the requirement is to have the highest gain at one specific direction (boresight).

3. Ground Plane Distance Studies

This chapter presents the studies performed through electromagnetic simulations about the impact of the distance between the antenna element and the ground plane on the antenna performance. Reducing the ground plane distance decreases the depth of the radome cross-section. Shorter cross-sections could result in a weaker shockwave (less wave drag) and lower structural loads. However, reducing this distance could also be detrimental to the antenna by causing excessive reflections that reduce the energy transmitted.

The baseline ground plane distance is 5.96 in or 151.4 mm, which had been previously defined by other authors based on previous applications of the UWB MCoRDS radar system. This was modified in adjustments of 0.197 in or 5 mm. The effects on antenna performance are evaluated using return loss, radiation patterns, and total realized gain plots. Return loss plots are analyzed using a -10dB (90% through power) threshold for acceptable changes in antenna performance. Antenna patterns are examined by comparing the half power beam width (HPBW) and shape of the main lobe. Negative changes in these latter plots include reduction of the main lobe level, and distortion of the nominal main beam shape. Lastly, the usable frequency ranges for ice sounding applications are limited to gain levels higher than 0 dB; however, the author analyzes the results by quantifying the relative changes in gain as a function of frequency and keeping in mind that the effect of changes in antenna gain is doubled based on the monostatic radar range equation for extended targets as shown in Chapter 8.

The following sub-sections present the electromagnetic model characteristics and assumptions, the simulation results, and the analysis of the effect of ground plane distance on antenna performance.

3.1. Model Set-Up

The electromagnetic model was set up in ANSYS Electronics Desktop 2016.1 software and analyzed using the HFSS solver (Ref. 16). Figure 27 shows the HFSS model which includes a vacuum box, the antenna on a substrate, and the ground plane. The vacuum or air box defines the 3D solution space. Its faces are at least λ/4 away, using 179 MHz as reference (frequency with most negative S11 value for the model with the original ground plane distance), from any

conductive surface. The antenna has copper material properties and is embedded on a Duroid substrate (shown in gray color), and the ground plane has aluminum material properties. The material properties are summarized in Table 8.

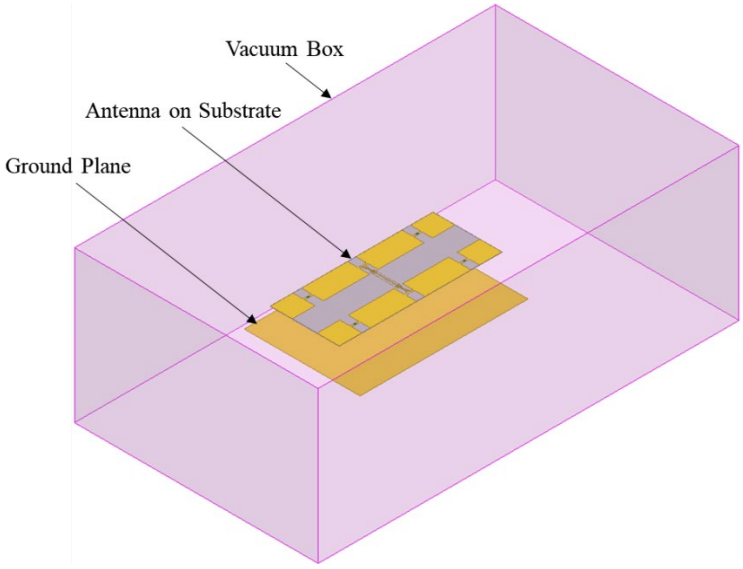

Figure 27: Isometric View of HFSS Model

Table 8. Material Electromagnetic Properties of HFSS Model Components

Property	Antenna	Substrate	Ground Plane	Vacuum Box
Material	Copper	Rogers RT/Duroid 5880 (tm)	Aluminum	Air
Relative Permittivity (~)	1	2.2	1	1
Relative Permeability (~)	0.999991	1	1.000021	1
Dielectric Loss Tangent (~)	0	0.0009	0	0
Bulk Conductivity (siemens/m)	58×10^6	0	38×10^6	0

The dimensions of the antenna and the ground plane are shown in Figure 28. The feed port of the antenna faces the ground plane as shown in Figure 29. This is because the antenna is fed within the radome through an access hole in the ground plane, and radiates to the space below the aircraft.

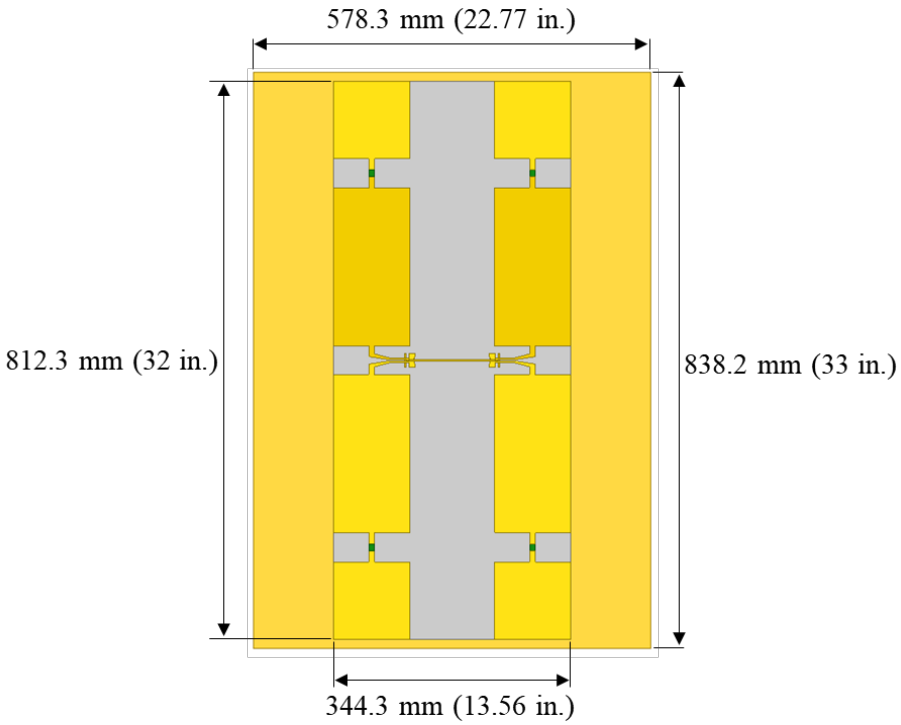

Figure 28: Top view of Antenna and Ground Plane (not to scale)

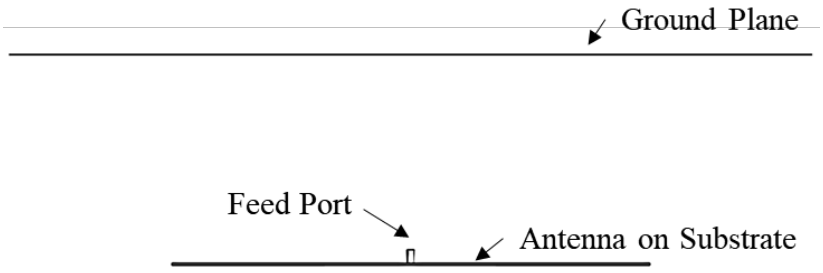

Figure 29: Front view of Antenna and Ground Plane showing Feed Port

The ground plane distance studies are performed based on the schematic shown in Figure 30. The ground plane distance is defined as the separation between the antenna and the face of the ground plane in closest proximity to the antenna (both modeled as surfaces in HFSS). This distance is originally set to 5.96 in. (151.4 mm) and is reduced in 0.197 in. (5 mm) modifications up to 1.18 in. (30 mm). Different models are created for each ground plane distance. All simulations are performed for the 150-600 MHz frequency range.

Figure 30: Schematic of Ground Plane Distance Definition

3.2. Return Loss

The reduction in ground plane distance generally decreases the antenna performance (lower S_{11} magnitude or higher amount of reflections) as shown in Figure 31. Exceptions occur at 165-280 MHz and 560-600 MHz where improvements in most cases are observed.

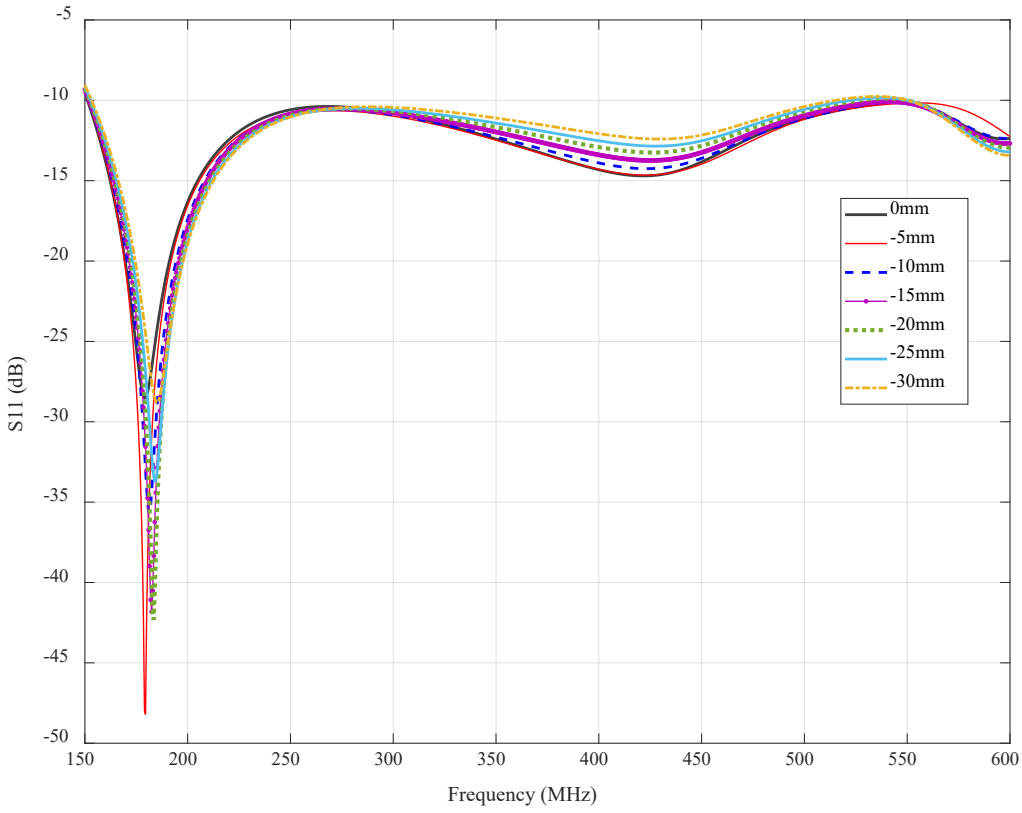

Figure 31: Return Loss Results at Increasingly Smaller Ground Plane Distances

The return loss is generally below or minimally violates the -10dB level for changes in ground plane distance between -15 and +30 mm (-0.59 in. and +1.18 in.) by a maximum change to -9dB in the lower frequency regions and -9.75 dB in the higher frequency regions. Hence, the bandwidth remains the same. The return loss results are still practical and changes in ground plane distance do not have a significant effect on the antenna performance. The next section assesses the change in gain at different frequencies.

3.3. Total Realized Gain

The total realized gain at nadir for larger and smaller ground plane distances are compared with the nominal ground plane distance in Figure 32. Larger ground plane distances improve the gain in the 150-463 MHz frequency range while smaller ground plane distances improve the gain in the 463-600 MHz range. The change in gain is approximately linear with the change in ground plane distance at each frequency.

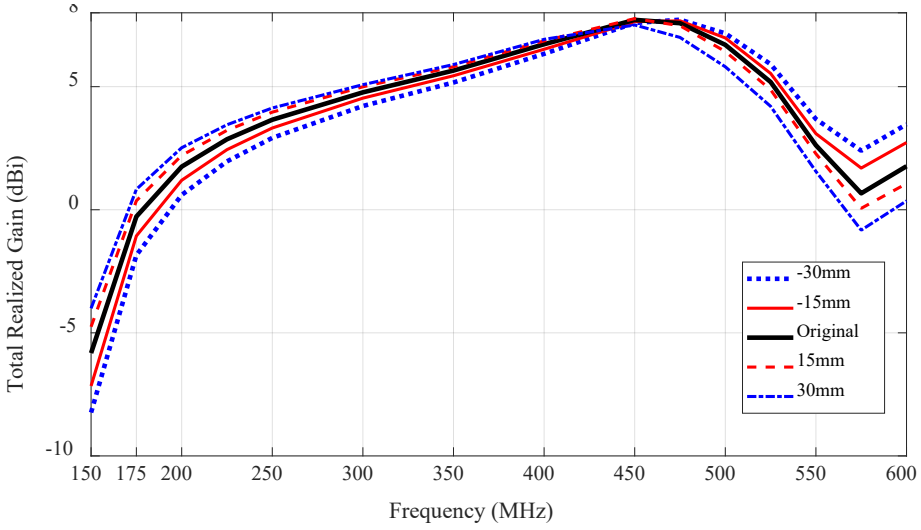

Figure 32: Total Realized Gain at Nadir for Different Ground Plane Distances

An increase in ground plane distance of 30 mm (1.18 in.) improves the gain by 1.8 dBi at 150 MHz, but worsens it by 1.49dBi (from 0.66dBi to -0.83dBi) at 575 MHz. Similarly, a reduction in ground plane distance by 30 mm worsens the gain by 2.4dBi at 150 MHz, but improves it by 1.7 dBi at 575 MHz. In general, an increase in ground plane distance by 15 mm results in the least changes in total realized gain from the "Original" trace.

Figure 32 is useful to define the frequencies at which the radiation patterns are analyzed in more detail in the following section. The frequencies used are: the limits of the frequency range of interest (150 and 600 MHz), 175 MHz due to the steep change in gain from 150 to 175 MHz, 450 MHz where the maximum gain of 7.7 dBi is observed for the "Original" trace in Figure 32, and 575 MHz which is an inflection point as shown above.

3.4. Radiation Intensity Patterns

The plots below show antenna patterns at different frequencies and elevation angles. For clarity, only five ground plane distances are presented in the main body of this document for -60°≤θ≤60°: original, +/- 15 mm (0.59 in.) and +/- 30 mm (1.18 in.). Figure 33 shows the radiation patterns at azimuth angle φ = 0° (along-track axis). The shape of the main beam is generally maintained as the ground plane distance is varied.

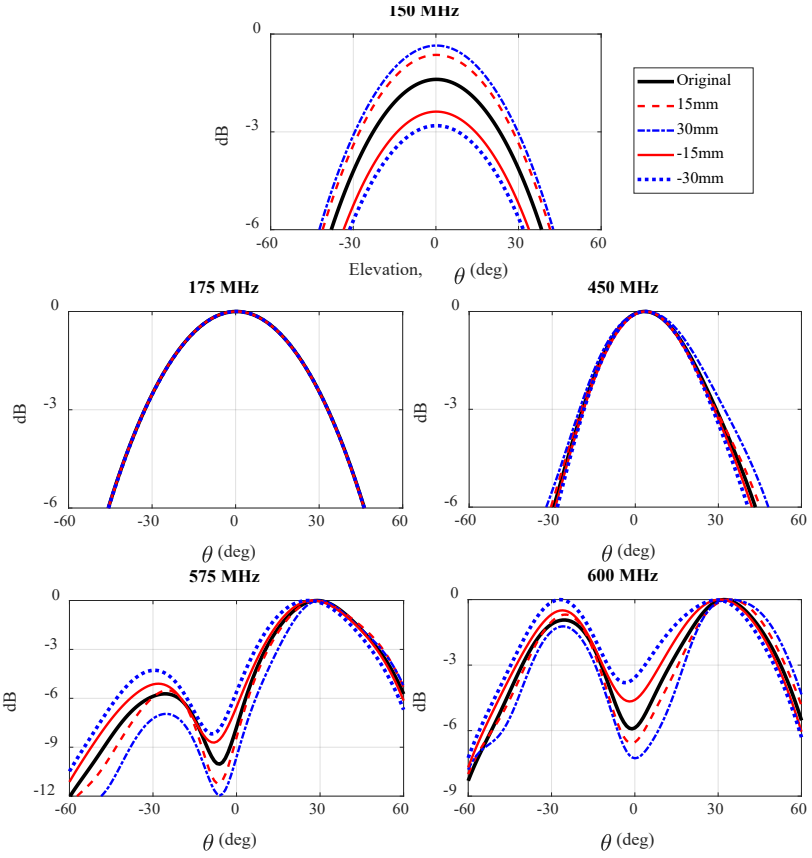

Figure 33: Simulated Normalized Pattern at φ = 0° (along track) at Different Ground Plane Distances

At 150 MHz, the main lobe has a lower peak level than the back lobe. Increasing the ground plane distance causes the main lobe to widen and its peak to rise. The opposite occurs when the ground plane distance is decreased. The largest changes in dB level occur from 0 to +/- 15 mm compared to smaller changes from +/- 15 to +/- 30 mm.

No changes are observed at 175 MHz. At 450 MHz, the main lobe peak does not change with respect to the rest of the radiation pattern, but increasing ground plane distance marginally widens the beam. At 575 and 600 MHz, the opposite of the response of at 150 MHz occurs as larger ground plane distances generally reduce the dB levels.

Figure 34 shows the patterns at azimuth angle (φ) of 90° (cross-track axis) for different frequencies.

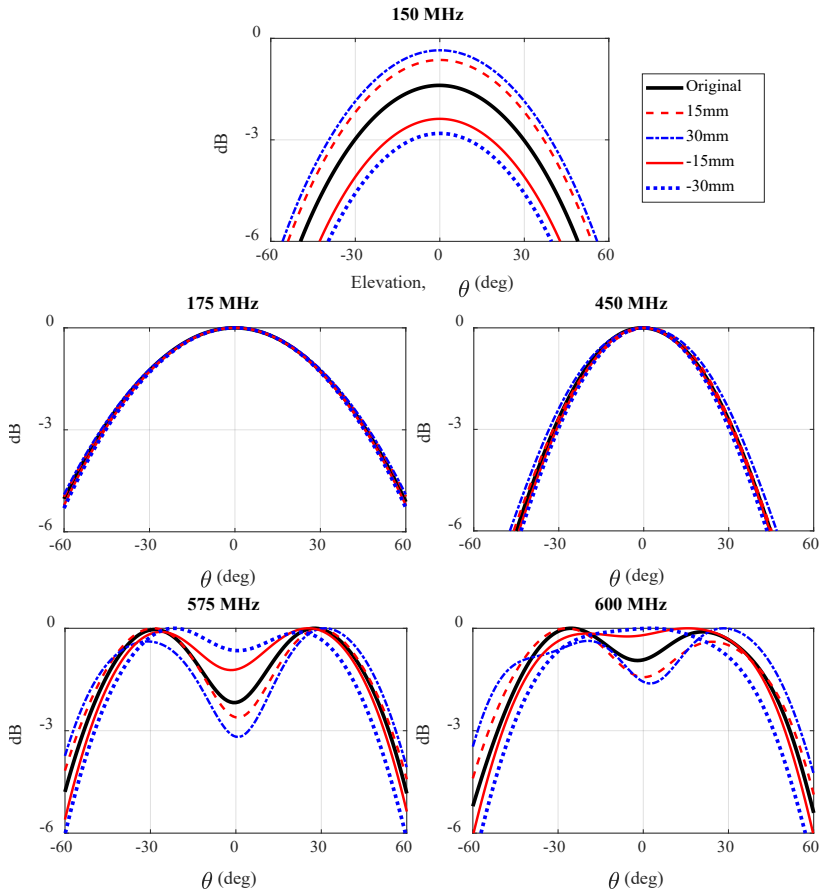

Figure 34: Simulated Normalized Pattern at φ = 90° (cross-track) at Different Ground Plane Distances

Similar observations are made as for Figure 33, with the exception that at higher frequencies larger ground plane distances result in widening of the beam, but reduction of the dB level at nadir. The opposite occurs for smaller ground plane distances. The patterns of 575 and 600 MHz, have a dip at nadir that becomes more even with the peaks at +/- 30˚ as the ground plane distance is reduced.

The motion of the array over the extended target due to the motion of the aircraft creates a large synthetic antenna aperture. This allows creating high-resolution images by combining successive radar echoes recoded from multiple antenna positions as the relative location of the aircraft (hence the antenna) changes with time. Hence, the synthetic-aperture radar (SAR) characteristic of the system is not dependent on the along-track HPBW of the antenna. Thus, along-track HPBW results are not addressed in this thesis.

The following Figure 35 shows the HPBW (-3 dB reference) for the cross-track information presented in Figure 34. In Figure 34, reducing the ground plane distance causes reductions in the HPBW across the full frequency range of interest, and the opposite occurs for larger ground plane distances. The HPBW plots presented in this document are calculated with respect to the peak value of the main lobe in the -60˚ to 60˚ elevation angle range.

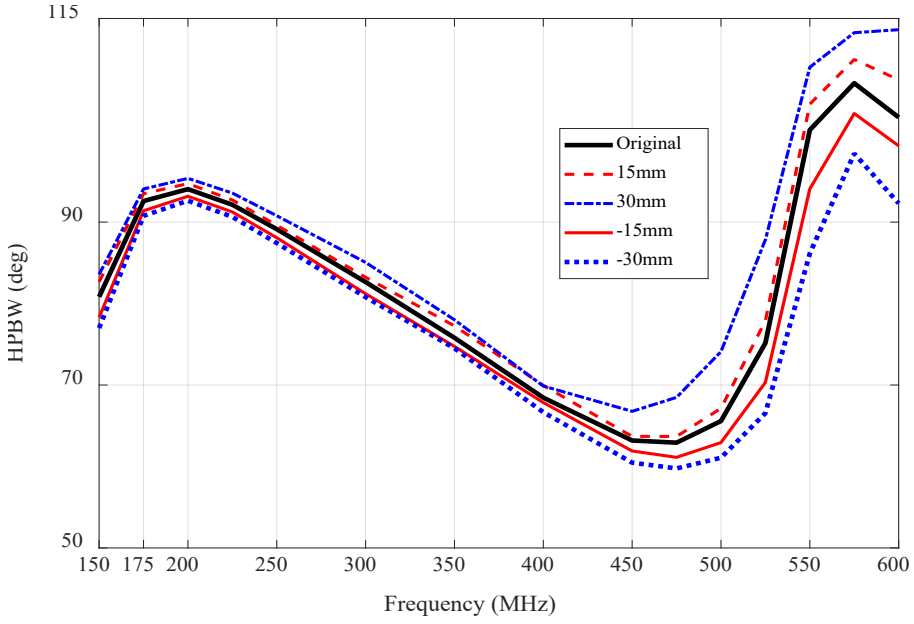

Figure 35: HPBW at φ = 90° (cross-track) at Different Ground Plane Distances

In 150-400 MHz frequency range, differences in HPBW due to different ground plane distances are small or negligible. The changes in HPBW due to changes in ground plane distance are significant again after 400 MHz (+9° for +30 mm and -9° for -30mm).

3.5. Summary of Ground Plane Distance Findings and Influence on Feasibility of Radome

The reduction in ground plane distance is beneficial to the return loss in the 165-280 MHz and 560-600 MHz range, but worsens the antenna performance in the 150-165 MHz and 280-560 MHz range. Ground plane distance reductions up to 15mm (0.59 in.) result in a response that does not trespass the -10 dB threshold, while reductions up to 30 mm (1.18 in.) minimally violate it. Thus, the reductions in magnitude in S_{11} due to smaller ground plane distances are still practical.

The total realized gain of a single UWB MCoRDS antenna with the original ground plane distance of 151.4 mm (5.96 in.) has a limited useful lower frequency range as its gain increases above 0 dBi only after 175 MHz. Reducing the ground plane distance further limits the useful lower frequency range by shifting the 0 dBi crossing to higher frequencies, and also lowers the realized gain up to 450 MHz. After 450 MHz, smaller ground plane distances increase the gain and expand the useful higher frequency range. Increasing the ground plane distance has the opposite effects. Hence, the change in ground plane distance is dependent on the need for higher performance at either lower or higher frequency ranges. This means that the performance of the antenna in terms of gain is unsatisfactory (at or below 0 dBi) due to ground plane distance changes depending on the frequency range of interest. The performance at lower frequencies is mainly important to measure ice bottom topography and internal layering. Deep penetration is a vital function of this antenna as part of the radar depth sounder (RDS) of CReSIS (Ref. 2).

The radiation intensity patterns support these findings. These indicate that the decrease of ground plane distance results in a reduction of the main lobe peak level at 150 MHz. The HPBW and the cross-track and along-track beam patterns are not significantly sensitive to changes in ground plane distance for 175-400 MHz. The antenna response is more sensitive to the ground plane distance at higher frequencies. These observations define a frequency range (175-400 MHz) in which deformations of the structure due to flight loads and tolerances in manufacturing will have minimal impact, if any, on the performance of the radar system.

Limiting the decrease of ground plane distance by 15 mm (0.59 in.) or less could result in insufficient reduction in structural loads. Structurally, reducing the profile depth would decrease the lateral bending stiffness of the radome as well. If reducing the depth failed to reduce the aerodynamic loads sufficiently, then the radome could experience higher deformation of the tip ends along the cross-track axis. This would add phase offsets to the measurements, and considerably increase the loads on the spars and bolts that attach the radome to the aircraft.

Although, valuable information can still be obtained even with reduced gain at lower frequencies due to reductions in ground plane distance, the author explored other methods to lower the aerodynamic loads while causing less negative effects on the antenna performance. These include using an airfoil shape more appropriate for transonic speeds and maintaining the airfoil shape in the region where the antenna is located (not flattening). This would prevent the development of shocks at the curved-to-flat transitions as shown in the previous chapter, and could also reduce the loads in the trailing edge. The next chapters study the effects on antenna performance due to the incorporation of curvature into the ground plane and the antenna.

4. Curved Ground Plane Studies

Previous radar systems developed by CReSIS have used antenna concepts that were flat. The aircraft platform and application did not require conforming the antenna to any shape in order to achieve higher performance. However, due to the transonic speed of the DC-8 and the large dimensions of the proposed radome, the realization of this project is highly dependent on the aerodynamic shape of the radome. Thus, the author studied the effects on antenna performance due to conforming the antenna and the ground plane to the curvature of an airfoil section.

Conforming to the curvature of an airfoil eliminates the sharp transitions from curved to flat surfaces, which cause significant changes in pressure and shockwaves as observed in Chapter 2.2. This chapter studies the consequences of adding curvature to the ground plane. The curvature is varied from low to high, and is defined as shown in Figure 36. The results are presented in terms of maximum vertical distance change from the nominal ground plane separation. A positive change results in a concave ground plane cross-section with respect to the antenna, and a negative change results in a convex shape.

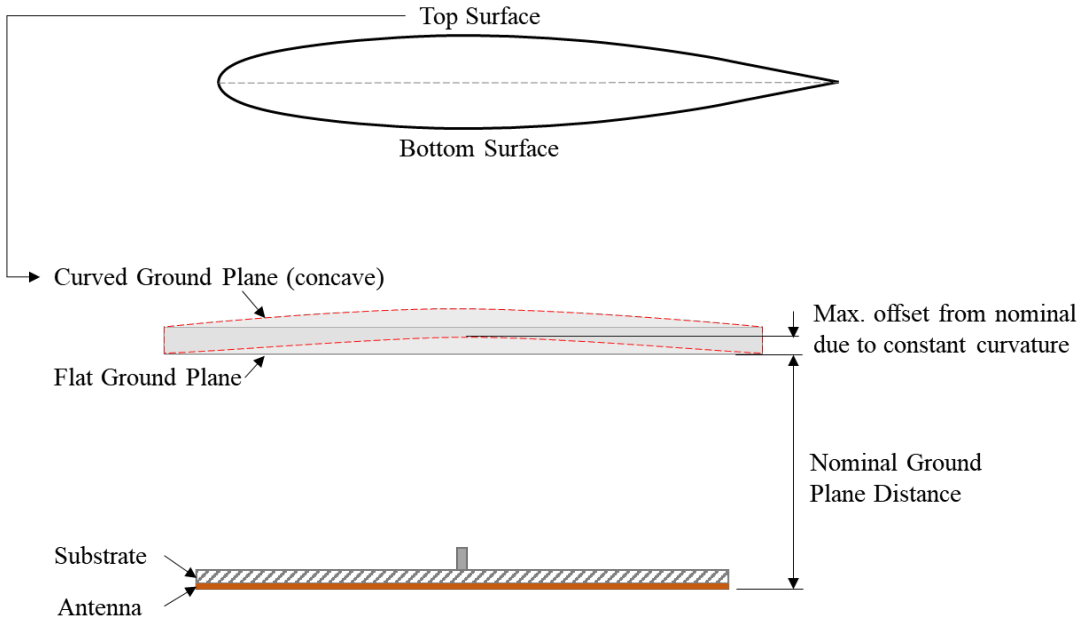

Figure 36: Diagram of Concave Ground Plane Definition

As shown in Figure 36, concave ground plane shapes (dashed red lines) are of interest assuming that the top surface of the radome would also act as the ground plane. This would allow decreasing the depth of the radome by approximately half, hence resulting in lower aerodynamic loads. The author also investigated the effect of convex ground planes for completion. The corresponding results are in Appendix B.

The curved ground plane results are compared to the flat ground plane results to determine differences in performance that are added by the curvature rather than by the maximum vertical offset. The following sub-chapters present the results of these studies, and address the feasibility of curving the ground plane.

4.1. Concave Ground Plane Return Loss

Figure 37 shows the return loss of different concave curvatures added to the ground plane only.

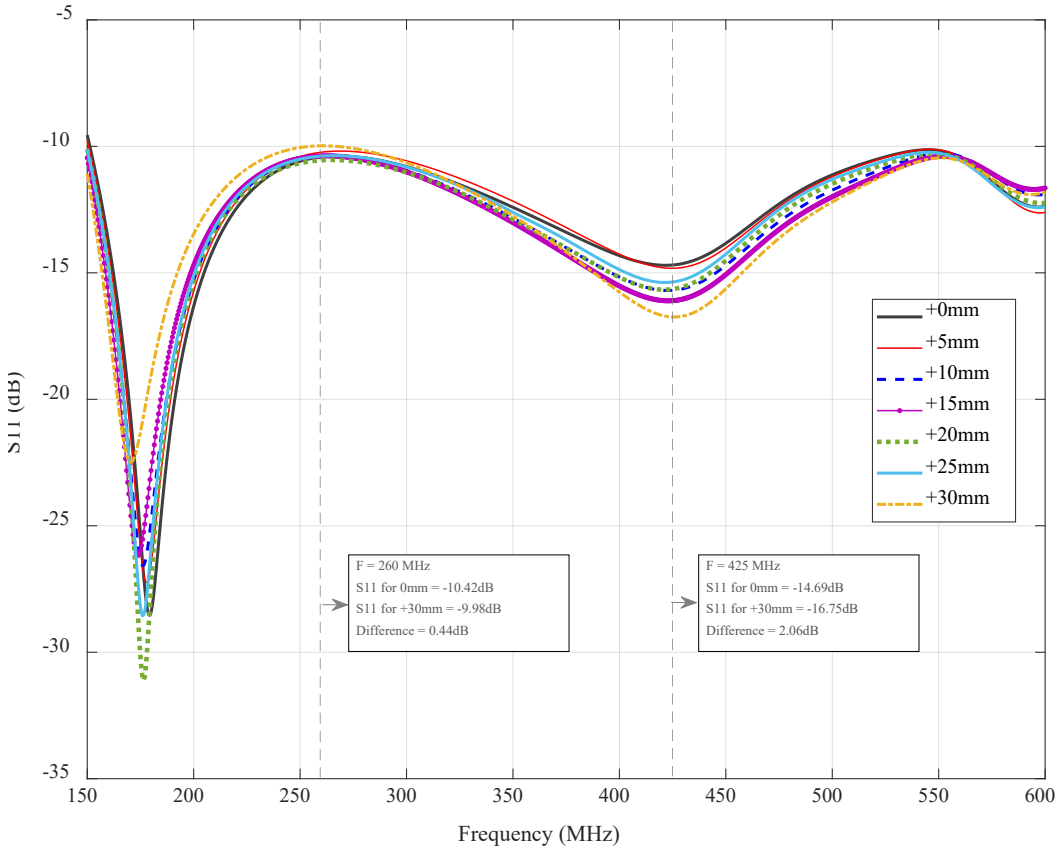

Figure 37: Simulated Return Loss for Increasing Concave Ground Plane Curvatures

The curvature increases the ground plane distance at the center of the antenna as shown in Figure 36, while the ground plane distance is unchanged at the edges of the ground plane (remains at the nominal value). The traces in Figure 37 correspond to the maximum vertical change from the nominal ground plane distance.

The change in ground plane distance causes either improvements or negligible detriments to the S_{11} (maximum of +4.8dB for +20 mm and - 0.7dB for +15mm). These results indicate that high amounts of concave curvature could be added while maintaining the response close to or under the -10 dB level. The following sections analyze the ground plane curvature effect on antenna gain and on the radiation patterns.

4.2. Curved Ground Plane Total Realized Gain

Figure 38 shows the total realized gain results at nadir for different curved ground planes. Similar to the results in Chapter 2.3, larger ground plane distances (in this case concave curvatures) increase the gain of the antenna across most of the frequency range. The opposite is true for convex shapes. However, the changes in gain above 200 MHz are significantly smaller or negligible compared to the "original" results.

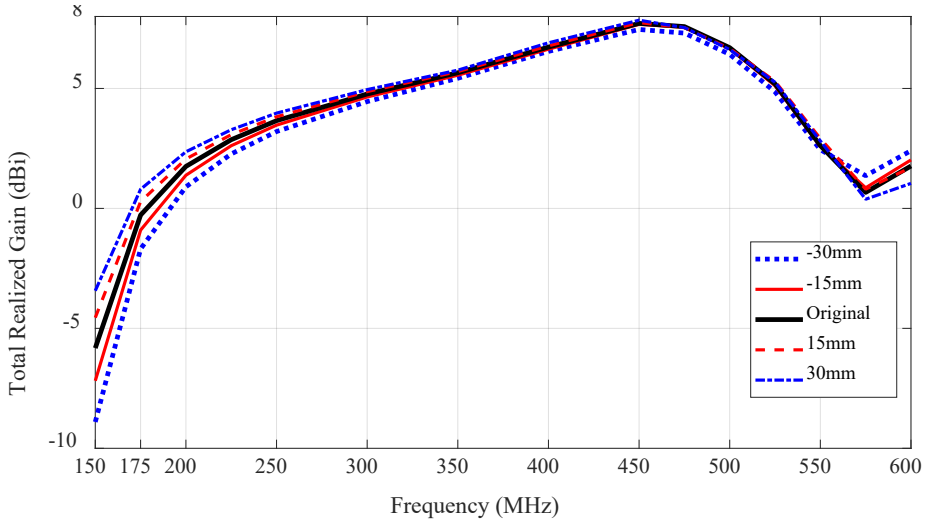

Figure 38: Simulated Total Realized Gain of Antenna for Various Curved Ground Planes

4.3. Curved Ground Plane Pattern and HPBW

Figure 39 shows radiation intensity plots of the antenna with different curved ground planes. At 150 MHz, concave (larger ground plane distance at feed port location) ground planes widen the beam and increase the peak level. The opposite occurs with convex ground planes. This is in accordance to the results shown in the previous chapter. However, a +30mm (1.18 in.) change widens the marginally more than +15mm (0.59 in.) , whereas a -30 mm change narrows and reduces the peak much more than a -15 mm change.

The 175 MHz and 450 MHz results show small or negligible changes in beam width and peak level due to the curvature of the ground plane.

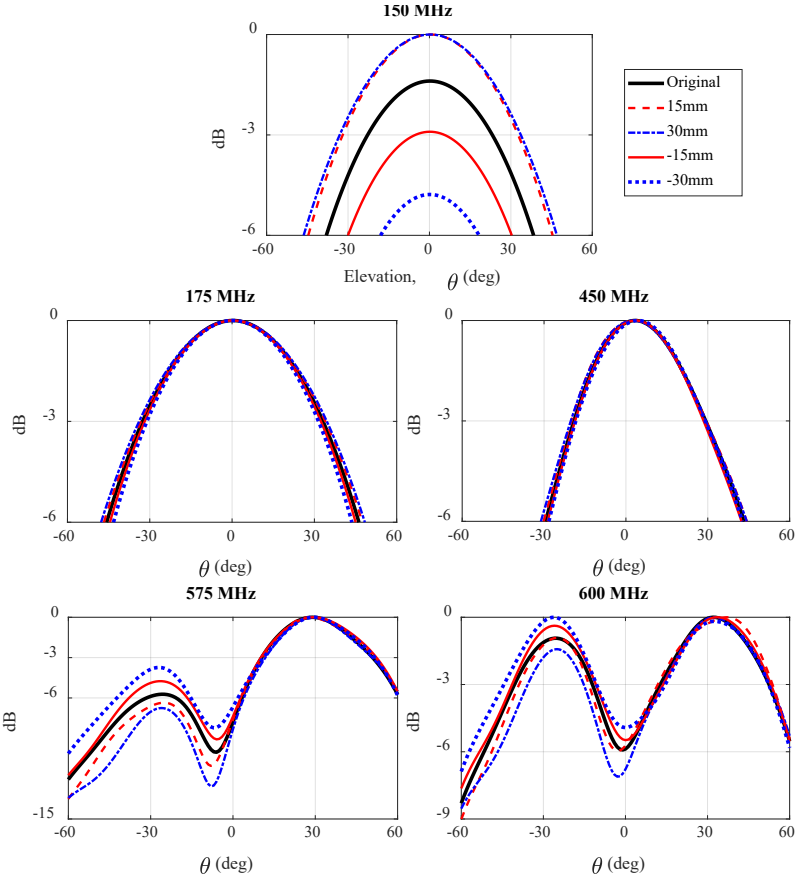

Figure 39: Simulated Normalized Pattern at φ = 0° for Different Curved Ground Planes

The 575 MHz results show that the right beam (0˚-60˚) is not sensitive to the various type of ground planes analyzed. The left beam (-60˚-0˚) is sensitive to these changes and shows that concave

shapes cause a decrease in the nadir level and narrow the beam (contrary to the results at 150 MHz). Similar observations can be made for 600 MHz.

The cross-track antenna patterns shown in Figure 40 have similar response to ground plane curvatures as the along-track patterns shown in Figure 39. Exceptions are observed at higher frequencies. At 575 MHz, larger concave curvatures do not significantly change the peaks at +/-30˚, but decrease the value at nadir (θ=0˚). On the other hand, convex curvatures increase the value at nadir with -30mm almost eliminating the dip at nadir. At 600 MHz, convex ground planes more evidently narrow the width of the beam, and the -30mm model fully removes the nadir dip from the pattern.

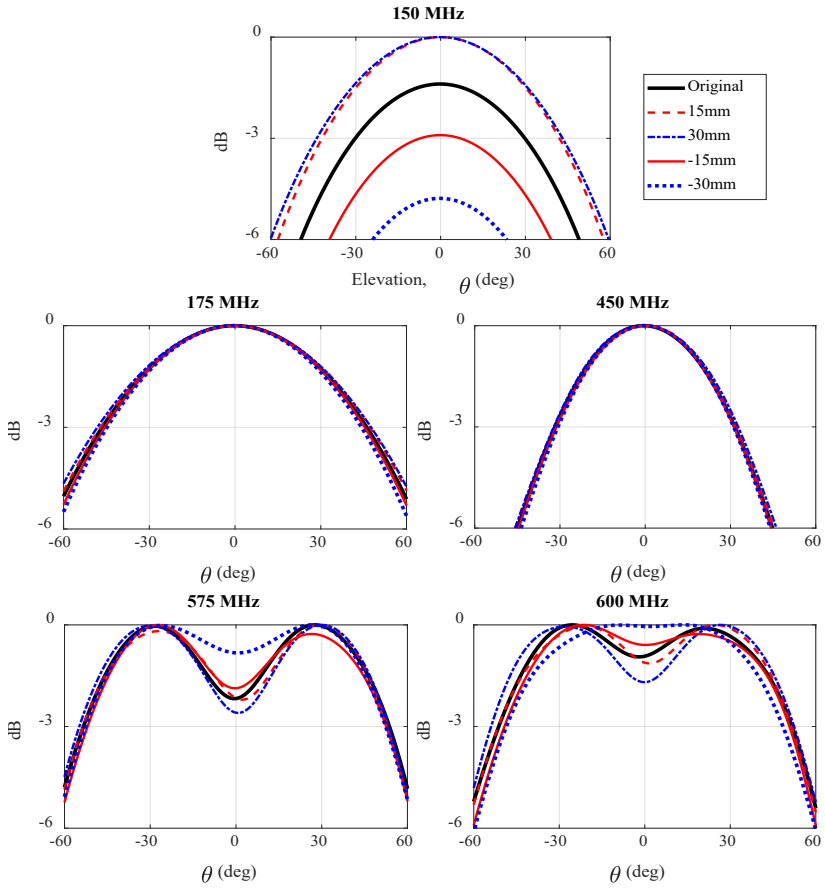

Figure 40: Simulated Normalized Pattern at Azimuth Angle φ = 90° for Curved Ground Planes

Figure 41 shows that the cross-track HPBW is minimally sensitive to different curved ground planes for a majority of the frequency range. The low and high ends of the frequency range are the most sensitive with +/- 4 to 8 degrees of maximum difference due to curvature.

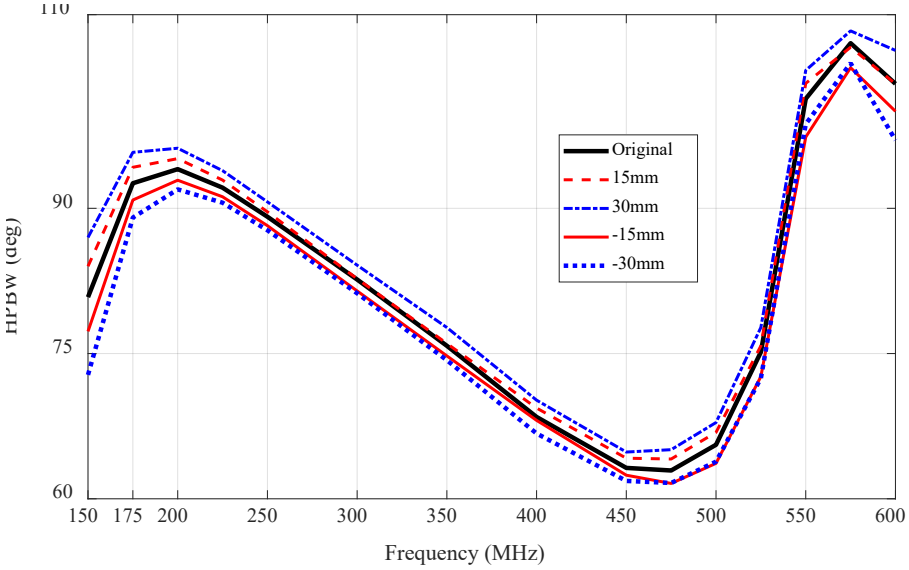

Figure 41: HPBW at φ = 90° (cross-track) for Different Curved Ground Planes

Along-track HPBW results are not shown because of the system addressed herein utilizes SAR technology as explained in the previous chapter. The following sub-sections compare in more detail the flat and curved ground plane results in an effort to differentiate maximum ground plane distance versus ground plane curvature effects.

4.4. Curved vs. Flat Ground Plane Return Loss

In this sub-chapter, the differences in return loss of curved ground planes in comparison to appropriate flat ground planes are evaluated.

Figure 42 and Figure 43 show +/- 5mm (0.196 in.) and +/- 30 mm (1.18 in.) curved ground plane results with the corresponding flat ground plane results in the same plots to help evaluate the differences between curved and flat models. Maximum vertical distance changes of 5 and 30 mm are selected for comparison for clarity, and to evaluate the effects due to minimum and maximum changes. As shown below, small maximum vertical offsets (+/- 5mm) added to curved and flat models result in approximately the same return loss. The curved and flat traces mostly differ in the

250-450 MHz region. These are acceptable variances. The differences between curved and flat models become more evident with larger maximum vertical offsets.

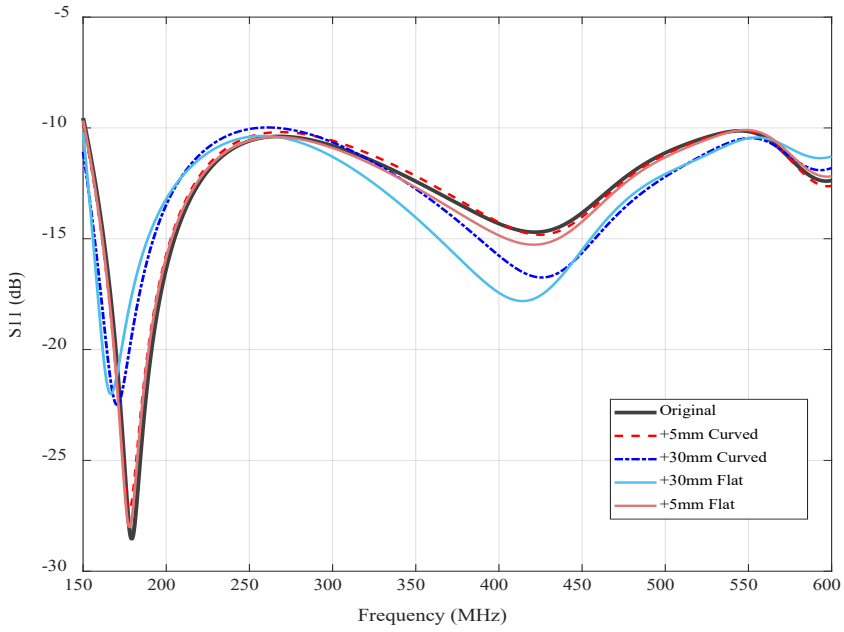

Figure 42: Return Loss of Flat vs. Concave Ground Planes

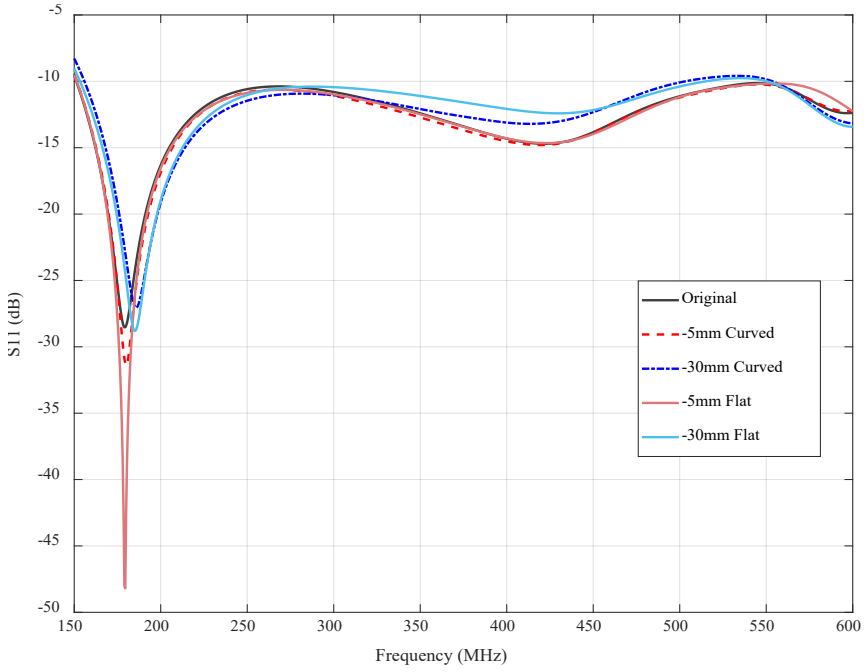

Figure 43: Return Loss of Flat vs. Convex Ground Planes

Figure 44 below shows the difference of curved to the corresponding flat ground plane results (Difference = Curved – Flat). Thus, for return loss, results above 0 dB mean curved results are worse than flat results. Below 0 dB means curved results are better than flat results.

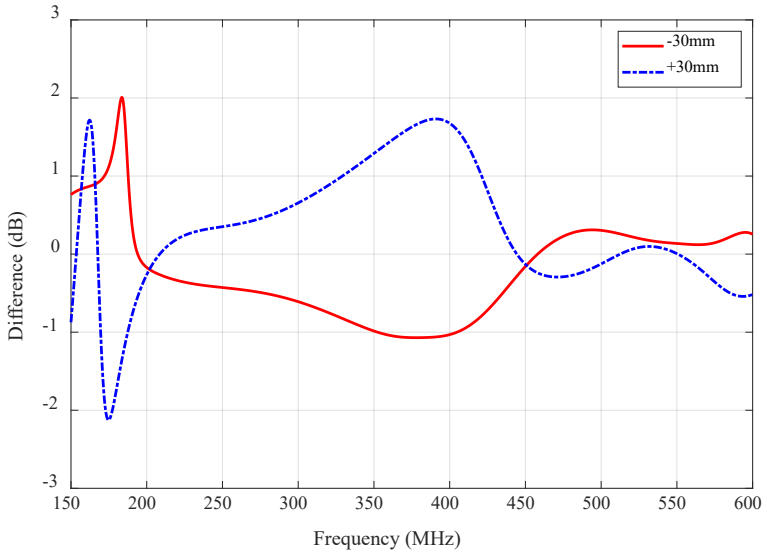

Figure 44: Curved to Flat Ground Plane Comparison of Return Loss

As shown above, the advantages or disadvantages in return loss of a curved compared to a flat ground plane are frequency dependent. Three frequency regions are identified: 150-200 MHz, 200-450 MHz, and 450-600 MHz. At these regions, the +30 mm results assimilate a mirror image of the -30 mm results. However, the S_{11} results for all curved and flat traces are below or near the -10 dB limit. Thus, these differences are considered acceptable.

The differences between curved and flat model results could be attributed to the influence of the performance characteristics at the forward and aft edges of the antenna (along the long dimension of the antenna) as illustrated below. Figure 45 shows that the ground plane distance at the feed port is the same for both curved and flat ground planes, but it is either closer or further away at the antenna edges (concave or convex ground plane respectively).

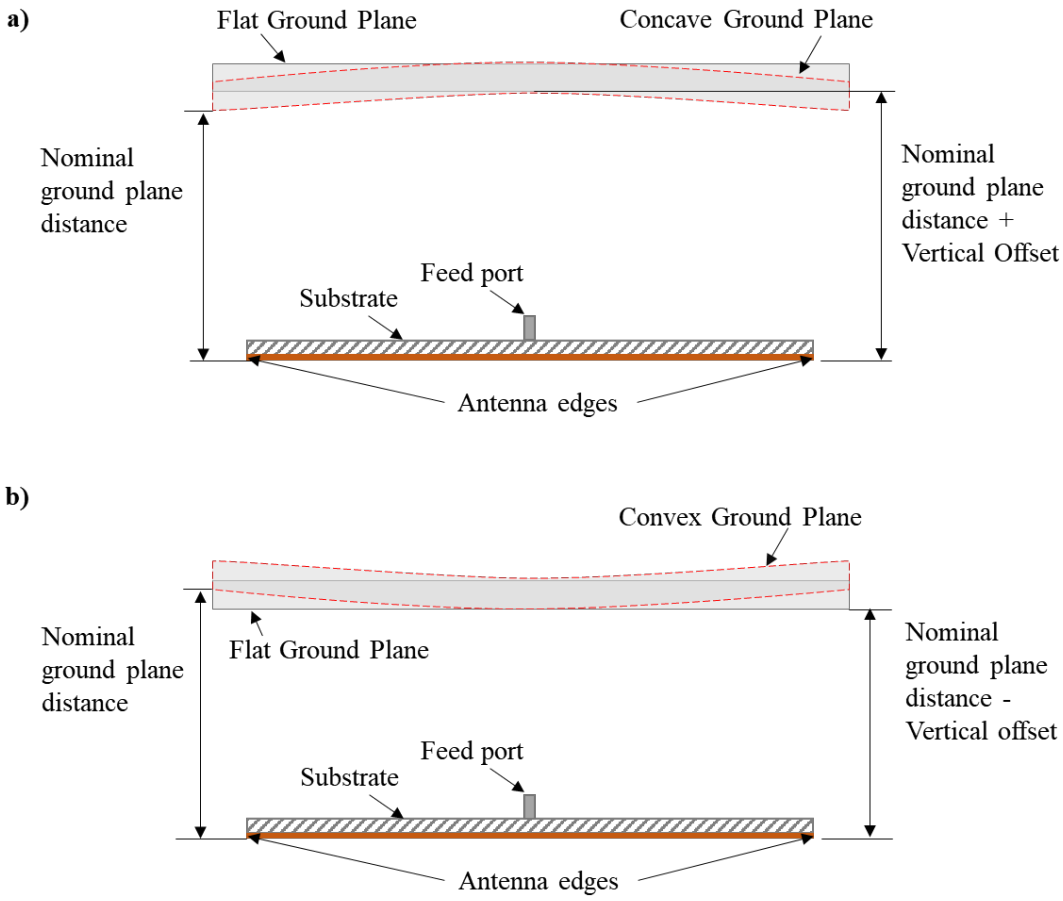

Figure 45: Edge effects illustration for Concave (a), Convex (b) and Flat Ground Planes with equal maximum vertical offset

The "edge effects" influence differently the three frequency regions previously identified. This influence is stronger with larger changes in ground plane distance. Curvatures that decrease the ground plane distance at the edges of the antenna (concave) result in worse performance in the second region, but better, by a smaller magnitude, in the third. The opposite is observed for curvatures that increase the ground plane distance at the edges of the antenna (convex). The next sub-chapter evaluates the differences between curved and flat model total realized gain results.

4.5. Curved vs. Flat Ground Plane Total Realized Gain

Three distinct regions are also observed in Figure 46. In this case, results above 0 dB mean that the model with curved ground plane performs better than the model with the flat ground plane.

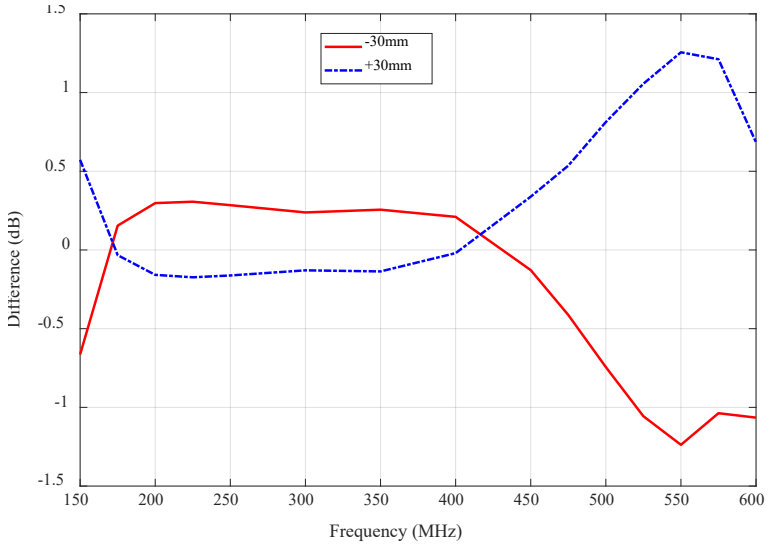

Figure 46: Curved to Flat Ground Plane Comparison of Total Realized Gain

Results below 0 dB mean the opposite. The regions are 150-172 MHz, 172-416.5 MHz, and 416.5-600 MHz. These are approximate to the regions identified in the return loss comparison. Similar to the results shown in the previous sub-section, a concave ground plane results in better performance in the first and third regions, but minimally worse in the second. The opposite occurs for a convex ground plane.

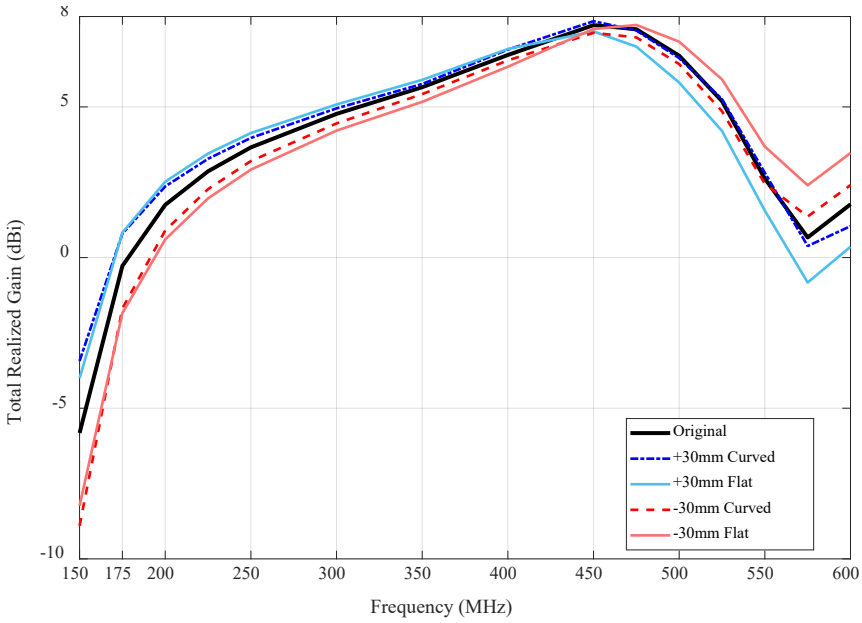

Figure 47: Total Realized Gain for Flat vs. Curved Ground Plane

Curvature or the “edge effects” have higher influence on the total realized gain for frequencies higher than 450 MHz (results in differences equal to 0.5 dB or higher). Changes in gain of 0.5 dB at 150 MHz are unimportant since the realized gain at 150 MHz for both flat and curved ground planes is significantly below zero as shown in Figure 47. Changes less than 0.5 dB in 175-450 MHz range are not considered to improve or deteriorate the performance significantly.

4.6. Curved vs. Flat Ground Plane Pattern

This sub-chapter compares the antenna pattern for flat versus curved ground planes. Figure 48 shows the along-track results.

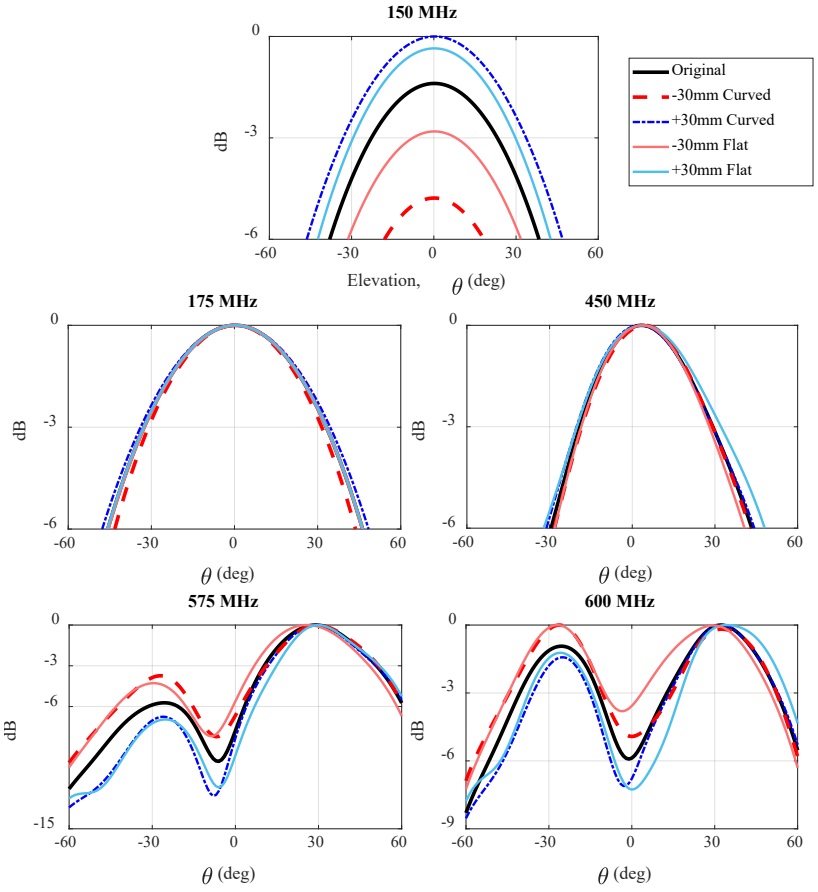

Figure 48: Simulated Normalized Pattern at φ = 0° for Curved vs. Flat Ground Planes

At f≤175 MHz, the concave models result in wider main lobe than corresponding flat ground plane results, but the differences are small or negligible. At 450 MHz, the flat ground plane results

diverge more from the "original" trace than the models with curved ground planes. However, the differences between flat and curved for this frequency and 575 MHz are very small. The same applies to 600 MHz with the exception that at nadir the curved ground plane results in smaller differences than flat ground planes.

Similar observations apply to the antenna pattern results shown below where the curved ground plane results show higher influence on the lower frequency range (150-400 MHz), and the flat ground plane model results show larger influence on the higher frequency range (400-600 MHz).

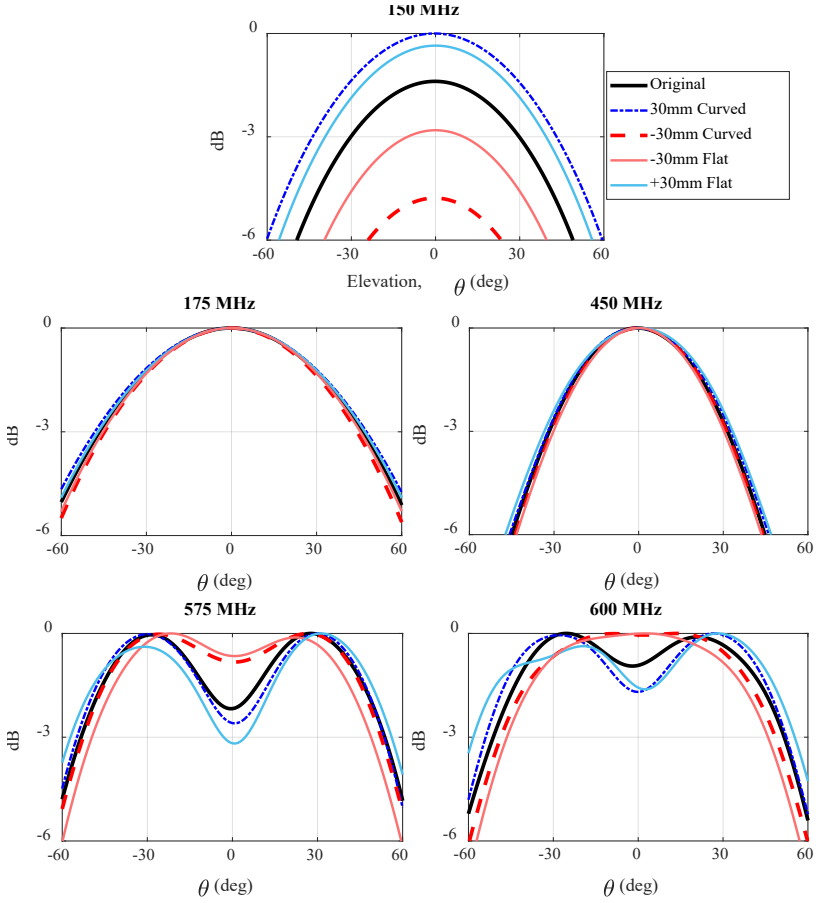

Figure 49: Simulated Normalized Pattern at φ = 90° for Curved vs. Flat Ground Planes

4.7. Curved vs. Flat Ground Plane HPBW

The observations for the antenna patterns are further substantiated by the trends observed in Figure 50. This indicates differences between curved and flat ground plane results. Positive differences

indicate that curved models widen the main beam more than corresponding flat models, and narrow it if differences are negative.

Cross-track results have three main regions: 150-250, 250-400, and 400-600 MHz. In the first region, the main beam also widens due to concave curvature. The changes in the second region are negligible (less than 0.5˚), and in the third region the concave curvature of the ground plane results in narrower beam. It is observed that convex ground plane results are an approximate mirror image of the concave results about the 0 degree crossing.

The largest changes (5-12 degrees) occur at 150 MHz and above 400 MHz. These are frequencies affected more noticeably by the added curvature compared to the 175-400 MHz region which is minimally affected. This is also in accordance with the total realized gain and beam pattern results.

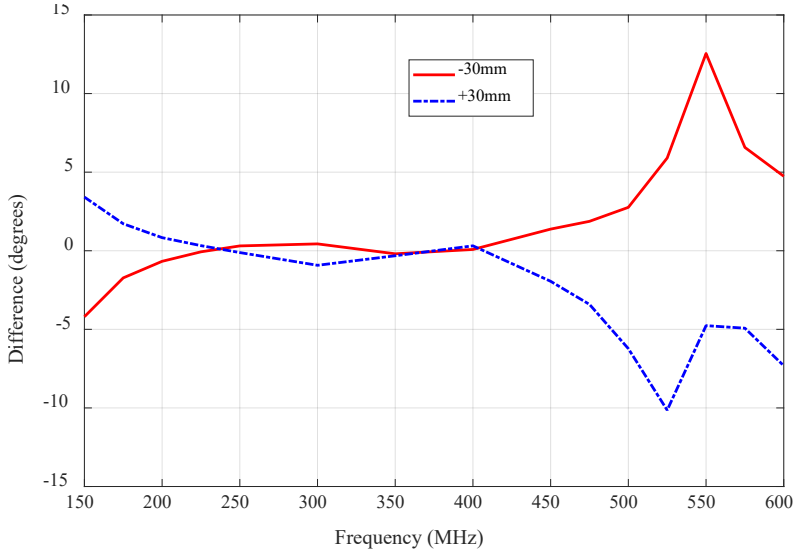

Figure 50: Curved to Flat Ground Plane Comparison of Cross-Track HPBW

4.8. Assessment of Advantages and Disadvantages of Curved Ground Plane Results

The results presented in this chapter indicate that the preference of a concave ground plane versus a flat plane due to improved electromagnetic performance is frequency dependent. General observations of curved compared to the corresponding flat models for maximum changes in ground plane distance of +/- 30mm (1.18 in.) are summarized in Table 9. The “model” column describes the type of curved ground plane.

The main electromagnetic advantage of a concave versus a flat ground plane can be seen in the high frequency range of the total realized gain where improvements up to 1 dB are observed. However, this frequency range (150 MHz bandwidth) is smaller than the low frequency range (300 MHz bandwidth). In previous applications of the same antenna, the radar was operated only in the 190-450 MHz frequency range to sound outlet glaciers and map deep internal layers with fine resolution (Ref. 3). If the same range was selected for this concept, then the addition of a concave curvature does not provide significant benefits to the performance.

Table 9: General Electromagnetic Performance for Ground Planes with +/- 1.18 in. or 30 mm Offsets

						Cross Track	
Model	**Distance @ antenna edges**	**Distance @ antenna center**	**S_{11}**	**Gain LF**	**Gain HF**	**HPBW LF**	**HPBW HF**
Concave	less	more	negligible	negligible	better	wider or same	narrower
Convex	more	less	negligible	negligible	worse	narrower or same	wider

LF = low frequency band (150-450 MHz)
HF = high frequency band (450-600 MHz)

Adding curvature to the ground plane also complicates its manufacturing process considering an 8-element array which has a large ground plane size in the spanwise direction. Bending a sheet of metal of such large size is possible; however, tolerances may not be met if curvature is small and also could be cost prohibitive to manufacture. Hence, alternative ground plane designs or fabrications methods would need to be explored. The next chapters study the aerodynamic performance of a supercritical airfoil and the electromagnetic effects of conforming an antenna to this shape.

5. Supercritical Airfoil Aerodynamic Results

Two dimensional aerodynamic analyses are performed to determine the characteristics of the SC0010 airfoil (Ref. 17) compared to the characteristics of cross-section shapes studied in Chapter 2.2. The supercritical airfoil is scaled to have a 93 in. chord (profile 3), but modified to have a rounded trailing edge of 2.2 in. (55.9 mm) thickness as shown in Figure 51. For aerodynamic analysis, this cross-section is thickened assuming 25 S-2 fiberglass layers of 0.0101 in. (0.26 mm) cured ply thickness as shown in Figure 52. This is comparative to similar sections on the current radome which have 12-24 layers (Ref. 5). Thickening the cross-section allows obtaining more accurate aerodynamic loads, despite that some sections of the new radome may need more or less than 25 layers.

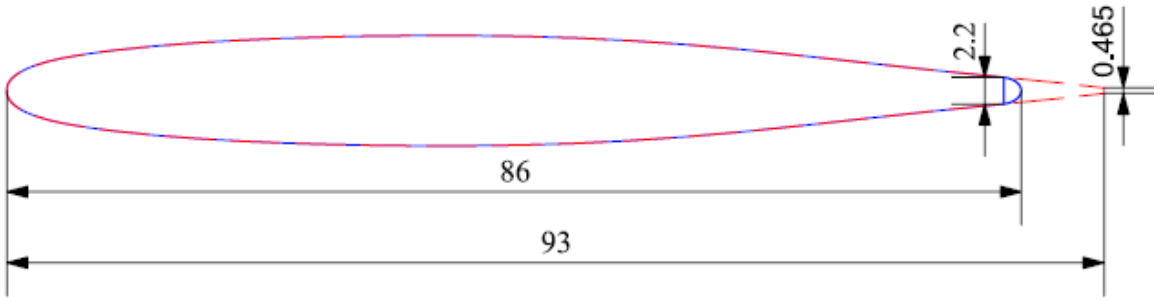

Figure 51: SC0010 airfoil scaled to a 93 in. chord (dashed red) and modified to an 86 in. chord with rounded TE (blue). Scale 1:16 in.

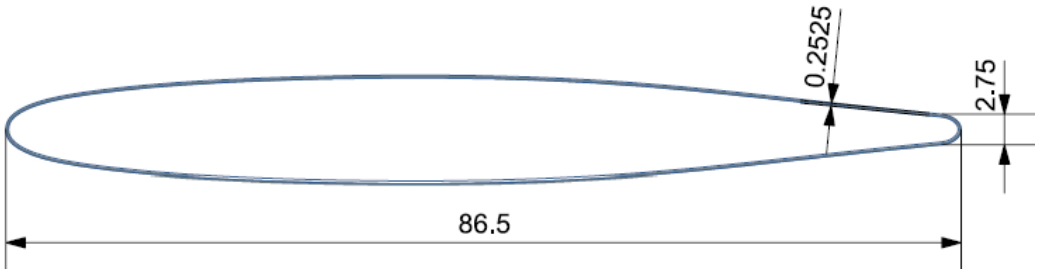

Figure 52: Modified SC0010 airfoil and thickened to 25 fiberglass layers

The analyses were also performed in collaboration with DARcorporation using Siemens STAR-CCM+ v.13.02.011 software. Chapter 2.2 assumptions were used in the analysis set up.

5.1. 2D Pressure Coefficient Distribution

Figure 53 and Figure 54 show that the pressure coefficient distribution is more uniform than profiles 1 and 2.

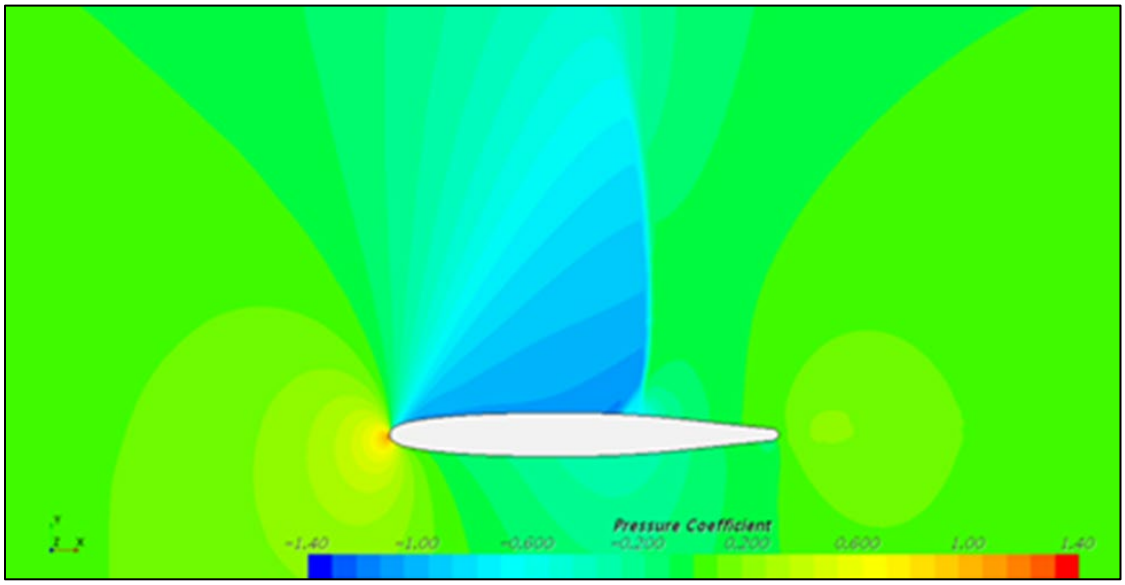

Figure 53: Snapshot of 2D pressure coefficient over profile 3 (SC0010) (Ref. 10)

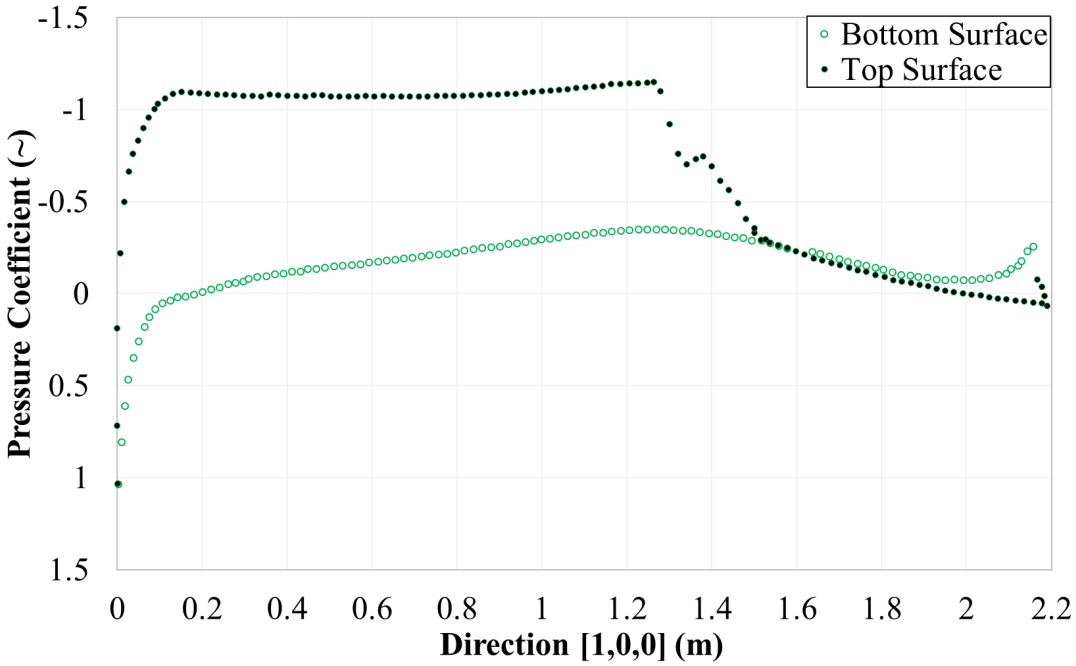

Figure 54: 2D Pressure distribution over profile 3 (Ref. 10)

The magnitude of the pressure coefficient is smaller and uniform across the bottom surface. In profiles 1 and 2, sudden changes in pressure were observed at the curved-to-flat transitions. These are not observed using the SC0010 profile.

5.2. Mach Number of 2D Profile 3

Profile 3 produces a weaker shockwave compared to profiles 1 and 2 as shown in Figure 55. This is significantly lower near the leading edge and results in lower wave drag. Weaker shocks on the lower surface that were observed on profiles 1 and 2, are not observed on profile 3 since no drastic changes in curvature are not present in the SC0010 shape. The lower surface also stays below Mach 1.

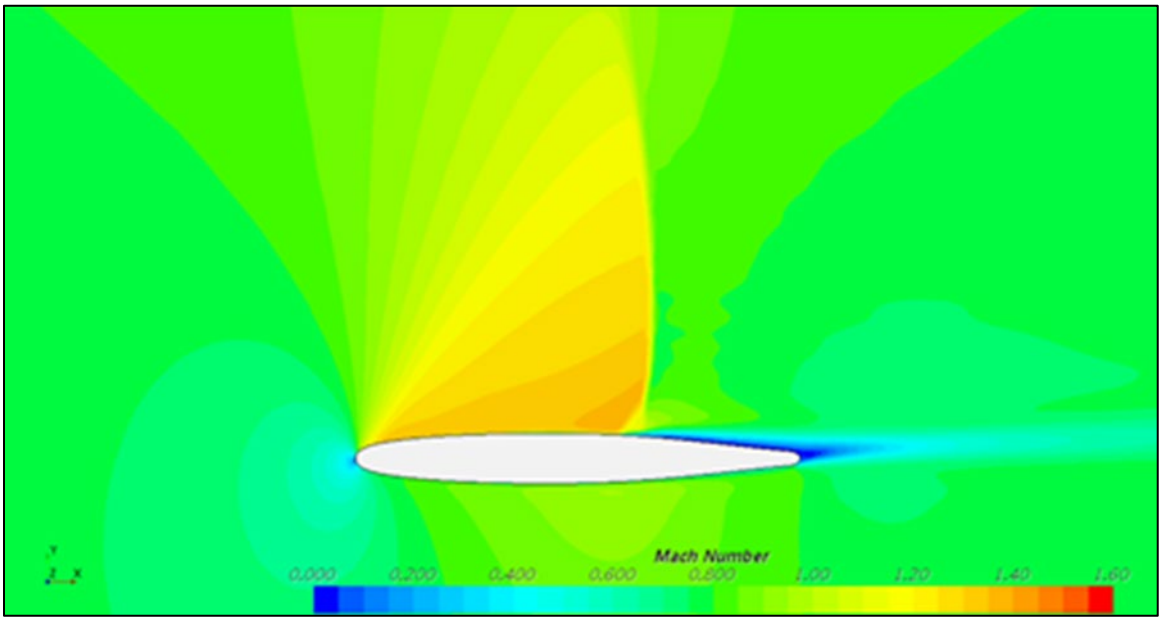

Figure 55: Snapshot of Mach number of profile 3 (Ref. 10)

The rounded trailing edge results in possible vortex shedding as shown in Figure 56. This is not as significant as for profile 2, but would still need to be further analyzed.

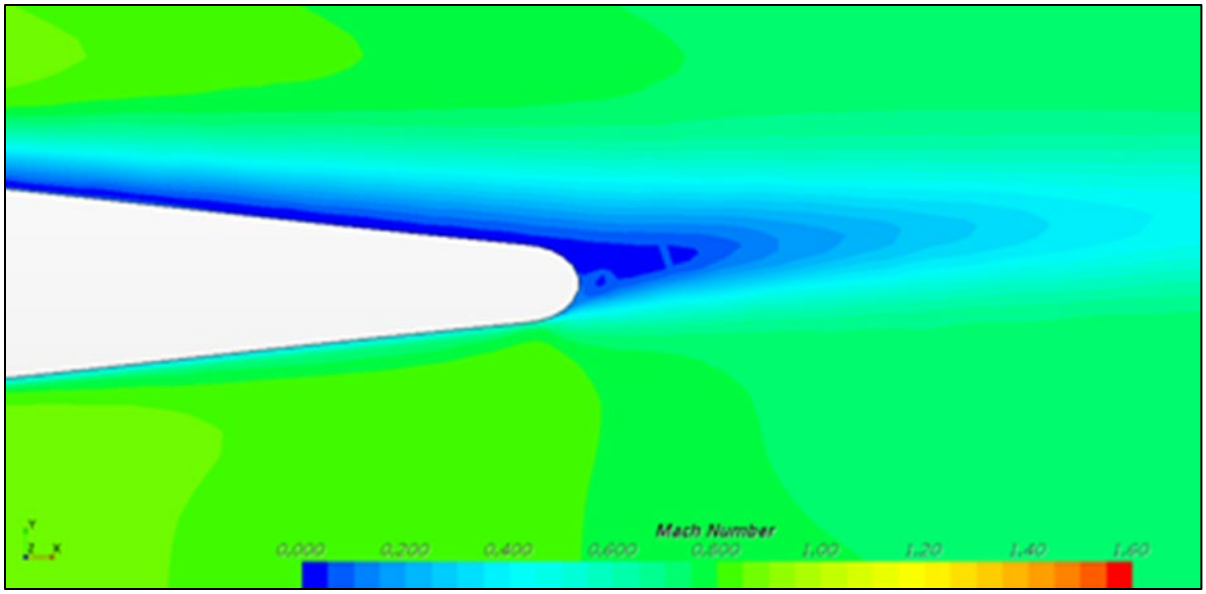

Figure 56: Snapshot of Mach number of trailing edge of profile 3 (Ref. 10)

5.3. Drag Coefficient

Profile 3 (SC0010) results in 22% less drag than profile 1 (long TE) and profile 2 (short TE) as shown in Table 10. This is accordance with the pressure coefficient and Mach results previously shown. Although the shear drag is the same for all profiles due to covering approximately the same surface area, the pressure drag is significantly reduced by eliminating the sharp transitions between curved-to-flat surfaces.

Table 10: 2D Drag coefficient comparison among all profiles (Ref. 10)

Drag Coefficient Breakdown	SC0010	Short TE	Long TE
Pressure	0.092	0.122	0.120
Shear	0.009	0.009	0.009
Net	0.101	0.131	0.129

5.4. Summary of Aerodynamic Analyses and Comparison of All Studied Profiles

Using the SC0010 supercritical airfoil profile results in less drag, lower magnitude shock waves, less shocks on the bottom surface, and a more uniform as well as lower magnitude pressure

coefficient distribution than the other profiles studied. The results of all studies are generally summarized in Table 11.

Table 11: General comparison among all profiles

Model	**Profile 3 SC0010**		**Profile 2 Short TE**		**Profile 1 Long TE**	
Chord	86.5 in.	2.2 m	76 in.	1.93 m	91 in.	2.31 m
TE Depth	2.75 in.	0.07 m	5.3 in.	0.13 m	1.5 in.	0.048 m
Max. Pressure Coefficient (~)	1.2		1.4		1.4	
Max. Mach No.	1.4 closer to TE		1.6 closer to LE		1.6 closer to LE	
Shedding vortices?	Yes, small		Yes, large		No	

Profile 3 has a smaller chord than profile 1, and shows better results except it produces small shedding vortices. The SC0010 profile was rounded at the trailing edge to reduce the chord and facilitate manufacturing. Since profile 1 results in no shedding vortices, profile 3 could be edited to have a similar trailing edge depth as profile 1.

The encouraging aerodynamic studies of profile 3 are complemented with electromagnetic studies performed using UWB MCoRDS antenna conformed to the bottom surface of this shape. The corresponding results are shown in the following chapter and compared to a shape of 2.5 times the curvature of a SC0010 airfoil.

6. Conformal Antenna Simulations

This chapter studies the alternative of having an aerodynamic cross-section similar to the schematic shown in Figure 57 where the ground plane remains flat, but the antenna is conformed to the curvature of the cross-section. In this case, both top and bottom surfaces would be fabricated with composite materials using foam tooling that accurately captures the curvature of the radome.

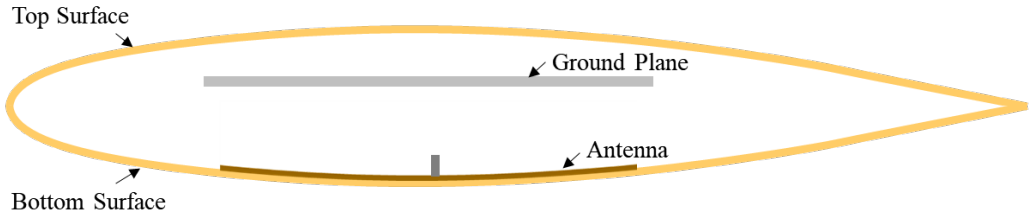

Figure 57: Schematic of Curved Antenna in Airfoil Cross-Section

The antenna is located on the bottom surface of the radome as shown above. Hence, it acquires a concave shape with respect to the ground plane. The ground plane distance is maximum at the feed port of the antenna, and minimum (nominal) at the forward and aft edges of the antenna as shown in Figure 58.

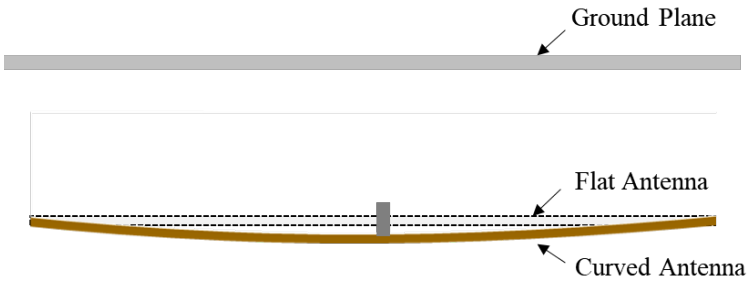

Figure 58: Schematic of Curved vs. Flat Antenna

The antenna is conformed to two shapes shown in Figure 59 below.

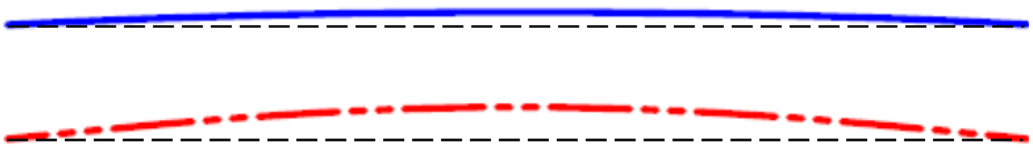

Figure 59: Top – Supercritical Airfoil. Bottom –1 in. (25.4 mm) Shapes. Scale 1:6 (in.)

The first shape (blue) is obtained from the bottom section of the supercritical airfoil SC0010 scaled to have a 91 in. (2.31 m) chord. This curvature results in a maximum vertical offset of 0.4 in. (10.16 mm). The geometry for the aerodynamic analysis was modified to have a 93 in. (2.36 m) chord rather than a 91 in. chord to better accommodate structural components within the radome after electromagnetic analyses were performed. The curvature at the region of the antenna for a 93 in. chord only differs by a negligible 3% (0.33 mm or.0.013 in. of vertical offset at the edges of the antenna) compared to a 91 in. chord; hence the electromagnetic results are not affected by this change.

The second shape (red) results in a maximum vertical offset at the center of the antenna of 1 in. or 25.4 mm and is created based on Equation 1 where l is the long side of the antenna in inches, and x is the position along the length. This shape is defined in Ref. 18 where the same antenna was curved using a custom software. Thus, this shape was selected for this study to evaluate the attainability of conforming all elements of the antenna correctly to obtain useful results.

$$z = \alpha x(l^3 - 2lx^2 + x^3)$$

$$\alpha = 3.0516x10^{-6};\ l = 32$$

Equation 1: Explicit Equation for 1 in. (25.4 mm) Maximum Vertical Deformation (Ref. 18)

The antenna under study has various components that lie in different planes as shown in Figure 60. The antenna components are held in place using a substrate which was included in the simulations for the previous chapters. However, intersections occur between the substrate and the conductive surface when the antenna is conformed. These impede the studies, thus the substrate is not modeled for the simulation analyses in this chapter. The substrate has a noticeable effect on antenna performance. This does not hinder the current analyses since the differences in performance due to the substrate are known and assumed to be constant due to the consistency kept between models. Supplemental information on substrate effects is provided in Appendix C.

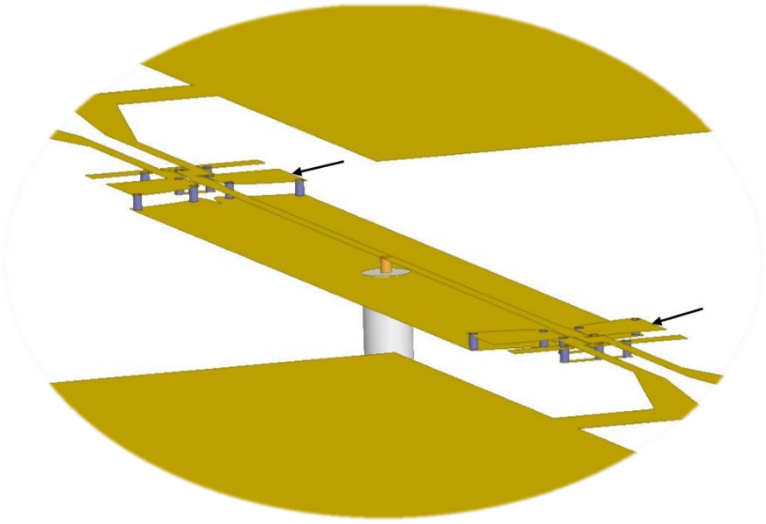

Figure 60: Antenna Components in Different Planes

The antenna was curved using in Siemens NX 12 (Ref. 19). To curve the antenna, a continuous spline that has the desired curvature and one that extends through the length of the antenna were aligned as shown in Figure 61. Then, the "Global Shaping" tool with the "By Curve" option was used to curve the antenna to the shape of the spline.

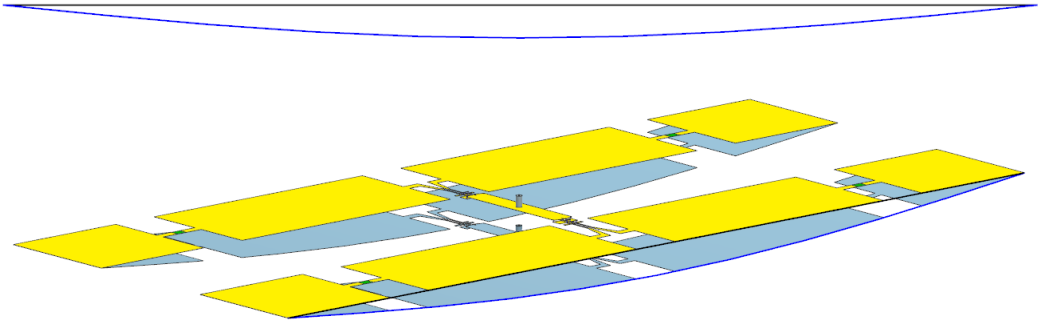

Figure 61: Top – Side view of Aligned Flat (black) and 1 in. (blue) Curves. Bottom – Flat (yellow) and 1 in. Curved Antenna (light blue). Not to scale.

The center section of the antenna remained approximately flat as shown in Figure 62. No undesired surface intersections resulted from the process of conforming the antenna, except for the center connector. This was manually and easily corrected.

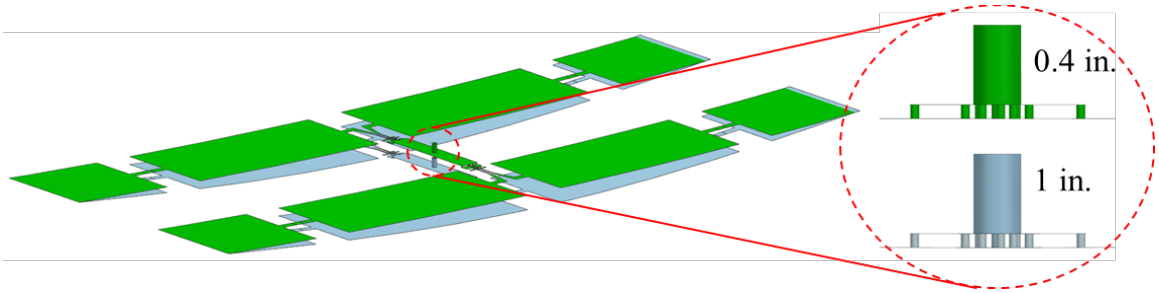

Figure 62: Center section of curved antennas. Top – Supercritical Airfoil Shape. Bottom – 1in. Shape. Not to Scale.

The following sub-chapters present the results of the curved antennas and compare to the flat antenna results by examining the same antenna performance parameters as in previous chapters. All results presented next correspond to models where the substrate was not modeled unless otherwise stated.

6.1. Conformal Antenna Return Loss

Figure 63 shows the return loss for models where the antenna is flat (0 in.), curved following Equation 1 (1 in. or 25.4 mm), and conformed to the shape of a supercritical airfoil section (0.4 in. or 10.16 mm). The legend corresponds to the maximum vertical offset of the antenna with respect to nominal ground plane distance.

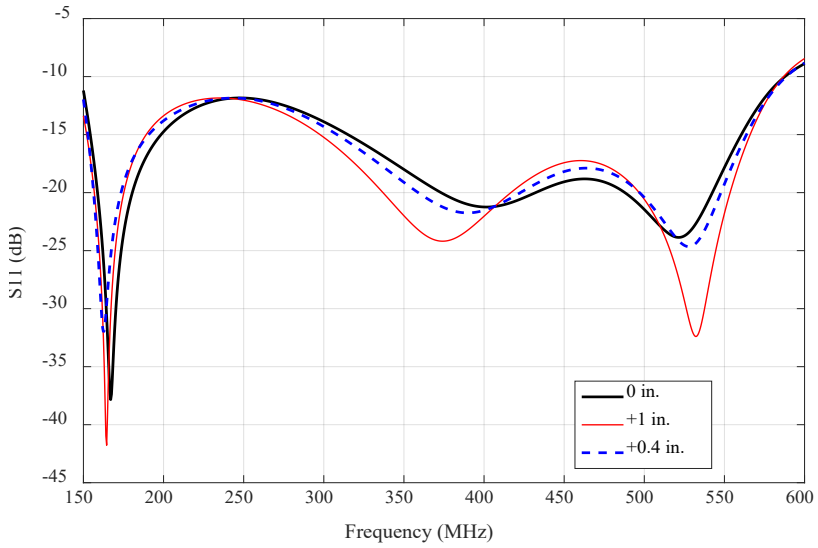

Figure 63: Simulated Return Loss for Curved Antennas

Increasing the curvature on the antenna causes the peaks and dips to be more prominent. The magnitude of these changes and the corresponding locations would not cause the S_{11} to go above the -10 dB level if the substrate was modeled. The supercritical airfoil shape results in minimal changes to the S_{11} trend, and no changes to the bandwidth.

6.2. Conformal Antenna Total Realized Gain

Figure 64 shows that curving the antenna minimally improves the total realized gain in the 175-312 MHz range, and decreases it in the 312-600 MHz range.

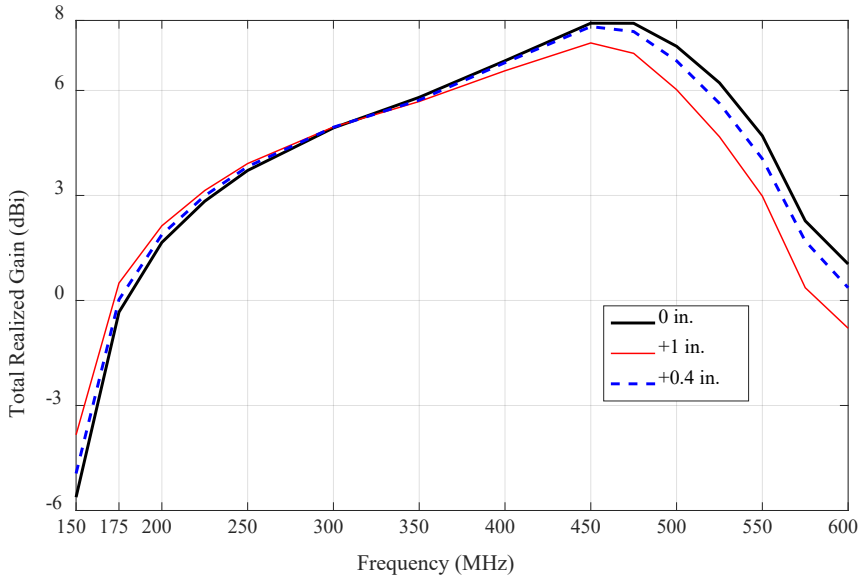

Figure 64: Simulated Total Realized Gain of Curved Antennas

Similar to previous gain results, 450 MHz remains as the frequency with highest gain, and the largest changes are observed at both ends of the frequency range as shown in Figure 65. The changes overall are minimum in the 200-450 MHz range.

Smaller deviations from the flat antenna result in less changes in performance as expected. Conforming the antenna to the supercritical airfoil shape results in changes less than 0.7 dB across the full frequency range. Conforming the antenna to have larger vertical offsets from nominal as the “1 in.” trend shows, could be prohibitive if the higher frequency range was of interest.

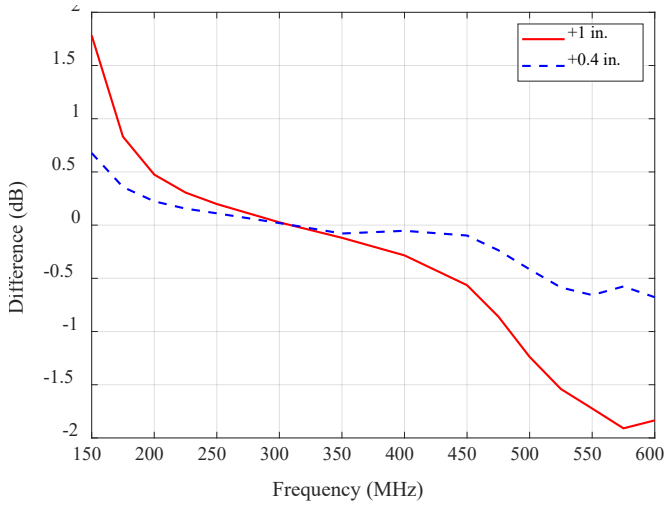

Figure 65: Curved to Flat Antenna Comparison of Total Realized Gain

6.3. Conformal Antenna Radiation Patterns and HPBW

The trends observed due to the change in maximum vertical offset by curving the antenna are similar to those observed with concave ground planes in Chapter 4. Figure 66 shows that conforming the antenna such that its center is further from the ground plane than the nominal distance results in the following:

- The main lobe widens and its peak increases at 150 MHz;
- No significant changes at 175-450 MHz;
- The main beam narrows with increasing maximum vertical offsets, and the nadir and left peak reduce at 600 MHz.

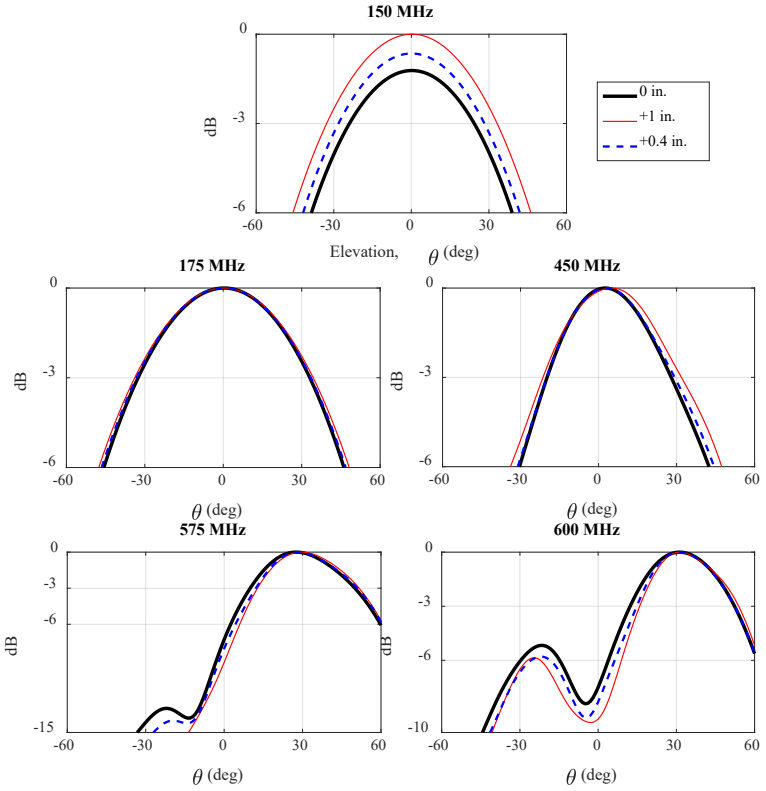

Figure 66: Simulated Normalized Pattern at φ = 0° for Curved Antennas

The effect of the substrate in the normalized results below show acceptable variance for the 150-450 MHz range as shown in Figure 67. For frequencies higher than 450 MHz, the right peak remains unchanged but the left peak reduces significantly due to the absence of the substrate. Thus, the normalized results above could be directly associated, in the specified regions, with the changes in performance of antenna models that include the substrate.

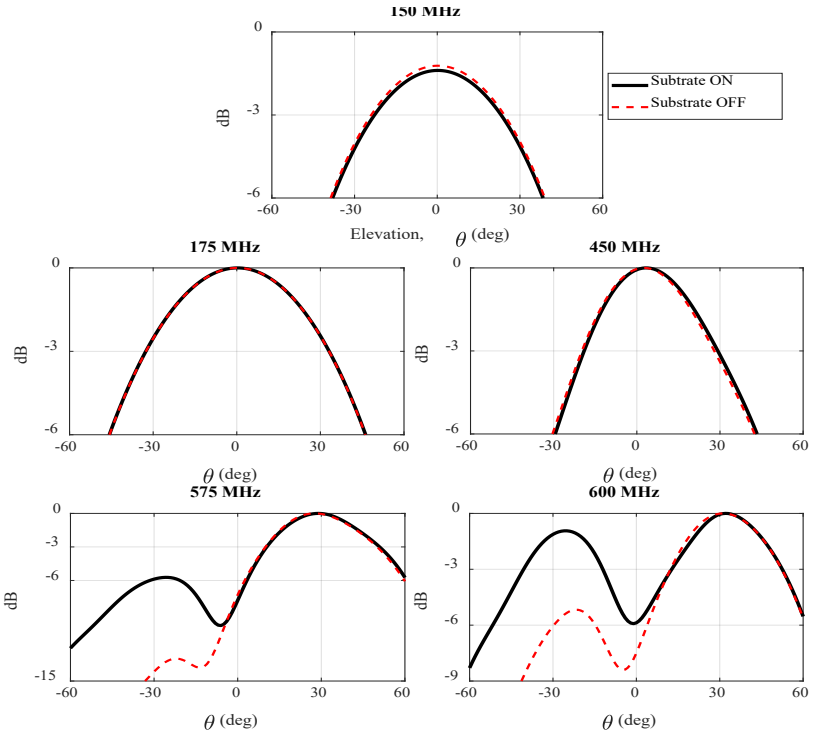

Figure 67: Substrate Effects on Patterns φ=0°

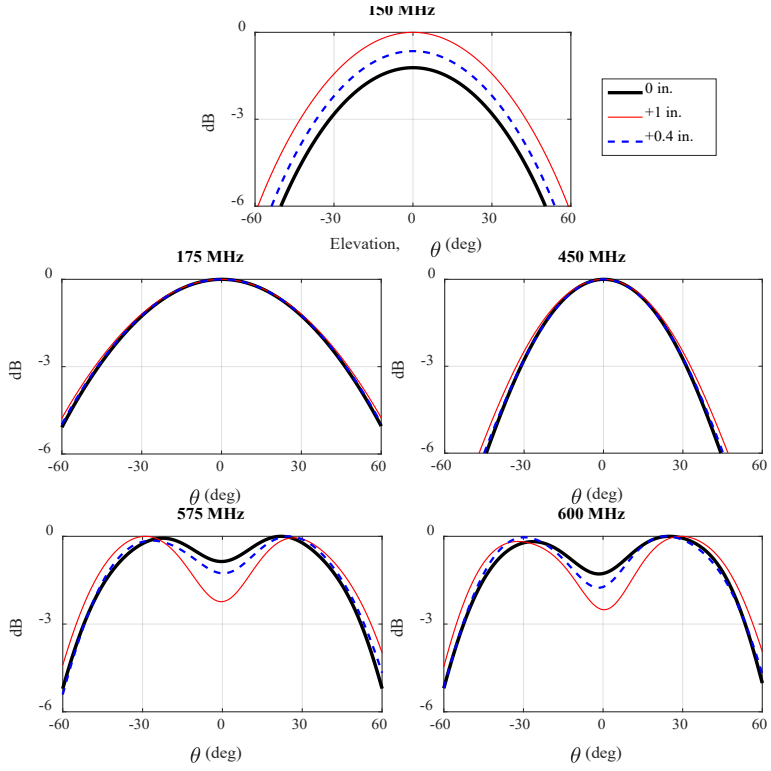

Figure 68: Simulated Normalized Pattern at φ = 90° for Curved Antennas

Similar observations can be made for the cross-track results shown Figure 68. Exceptions occur at higher frequencies (575-600 MHz) where the increase in maximum vertical distance widens the main beam, but still reduces the nadir level.

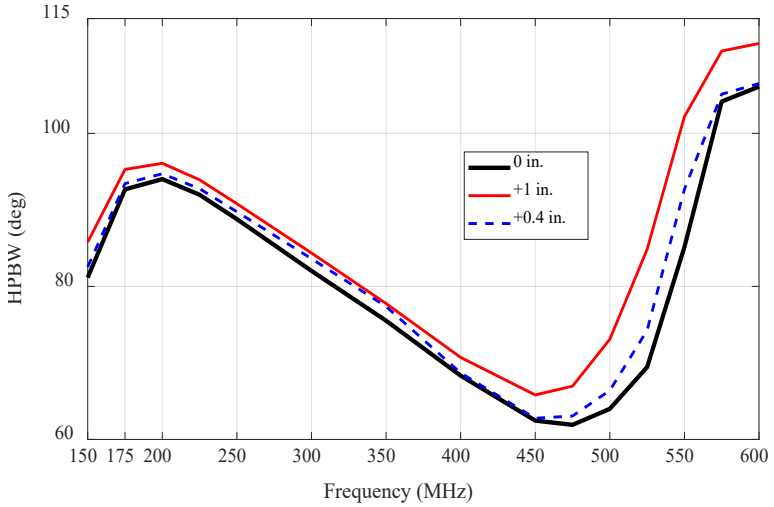

Figure 69: Simulated HPBW at φ = 90° for Curved Antennas

These are supported by the HPBW results shown in Figure 69. Adding curvature to the antenna increases the HPBW across the full frequency range. The differences of curved to flat results are shown in Figure 70. The 0.4 in. results are negligible are overall negligible across the full frequency range.

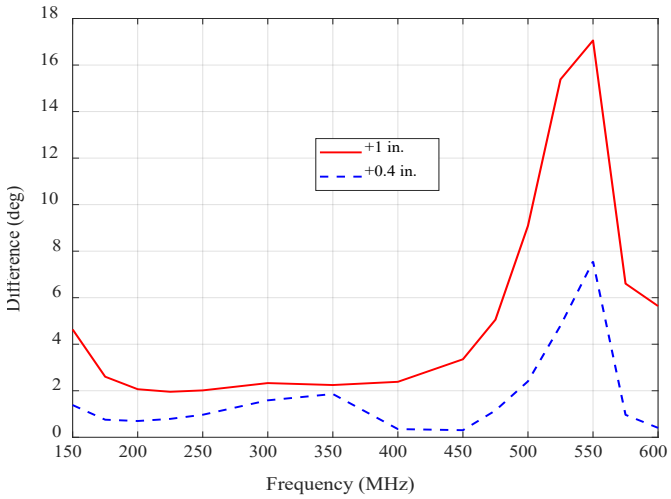

Figure 70: Curved to Flat Antenna Comparison of HPBW at φ = 90°

All results can be directly related to the results expected from models that include the substrate for 150-475 MHz since the substrate effects are unimportant in this range as shown in Figure 71.

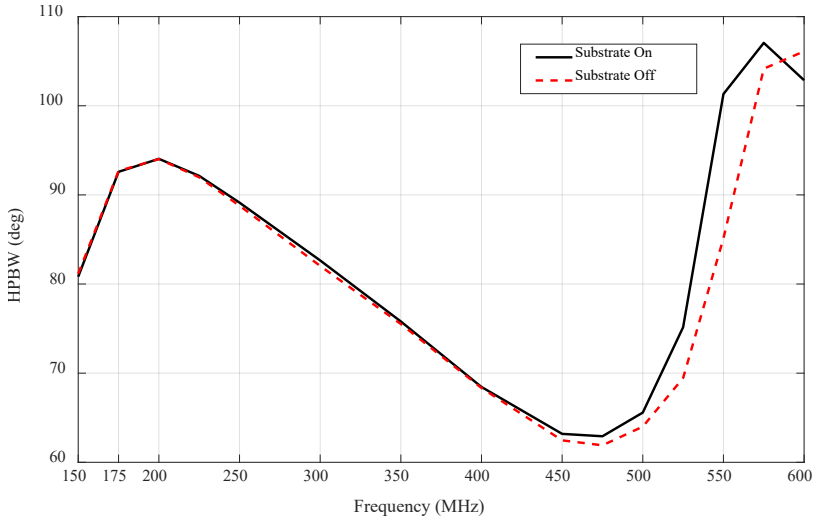

Figure 71: Flat Antenna - Substrate Effects on HPBW φ=90°

6.4. Summary of Electromagnetic Simulation Results of Conformal Antennas

The UWB MCoRDS antenna under study can be conformed to the SC0010 airfoil shape scaled to a 91 in. chord without resulting in significant changes in performance. The general changes on electromagnetic performance due the added curvature, disregarding the magnitude of the change, are summarized in Table 12 below.

Table 12: General Electromagnetic Performance for Curved vs. Flat Antenna

						Cross Track	
Model	**Distance @ antenna edges**	**Distance @ antenna center**	**S_{11}**	**Gain LF**	**Gain HF**	**HPBW LF**	**HPBW HF**
0.4 in.	same	more	negligible	same or better	worse	wider or same	wider

LF = low frequency band (150-450 MHz)
HF = high frequency band (450-600 MHz)

The influence of antenna curvature on the results is frequency dependent which agrees with results presented in previous chapters. This is small due to the small maximum vertical offset added by the supercritical airfoil shape.

Increasing the ground plane distance at the feed port with the addition of curvature to either the antenna or to the ground plane result in similar trends. However, conforming the antenna could be performed effortlessly since the substrate has sufficient flexibility, and the dielectric radome would accurately capture the curvature by being fabricated using CNC molds.

Experimental return loss, gain and radiation intensity patterns are presented in the following chapter to verify the effects of conforming the UWB MCoRDS antenna to specific curvatures.

7. Verification of Electromagnetic Performance of the UWB MCoRDS Antenna

Electromagnetic tests were performed in the Anechoic Chamber of the University of Kansas to verify the performance of the different conformal antenna configurations studied in this document. Return loss and antenna pattern measurements were taken using a bare UWB MCoRDS antenna (with substrate, but not embedded in fiberglass).

The relative changes in performance due to curvature are evaluated and compared to the simulation results. In the previous chapter, the antenna was analyzed without the substrate due to surface-to-solid intersection issues. Only the flat configuration was analyzed with and without the substrate. Thus, only the flat antenna test results can be directly compared with simulation results. The following sub-sections present the test set-up and analyze the results.

7.1. Test Set-Up

Figure 72 shows the relative position of the antenna under test (AUT) during the experiments performed in the KU anechoic chamber.

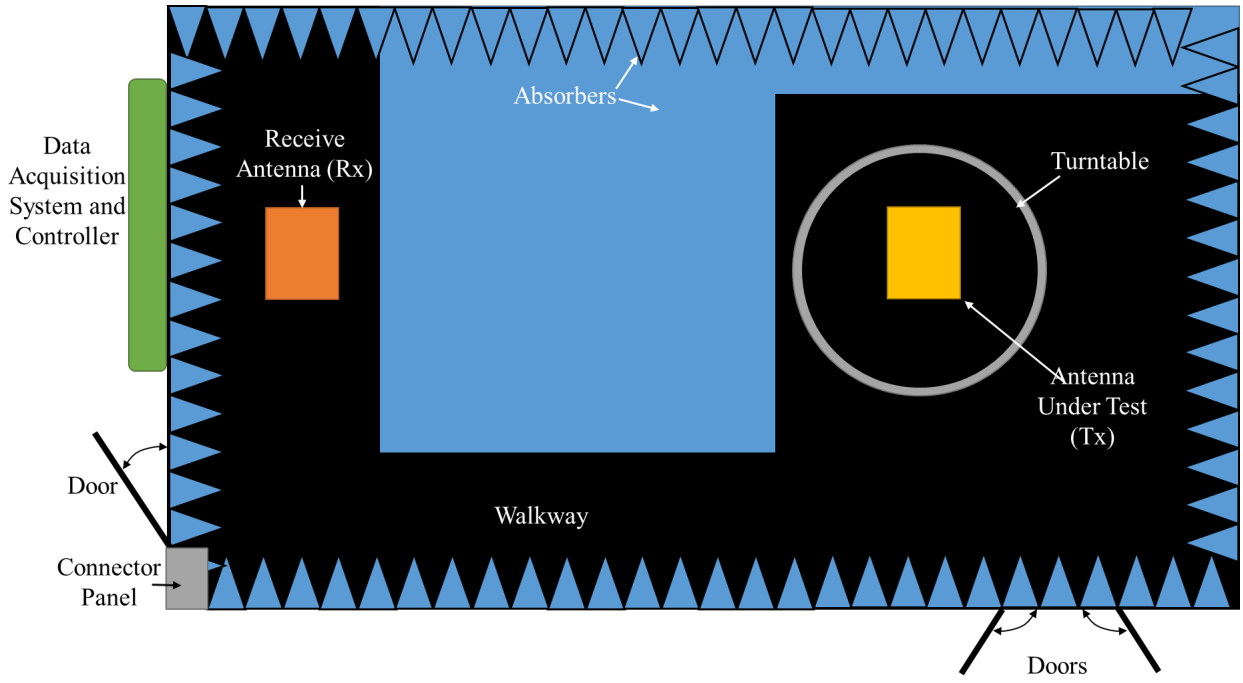

Figure 72: Relative Position of Test Components in KU Anechoic Chamber

The return loss measurements were performed with only the antenna under test (UWB MCoRDS) inside the chamber. Along-track and cross-track pattern measurements were obtained with the receive antenna at the front end of the room and the UWB MCoRDS on the turntable. The phase centers of the antennas were aligned with respect to each other and positioned 50 in. (1.27 m) above chamber floor. S_{21} measurements were recorded with the data acquisition system while the AUT performed a 360° on the turntable. The S_{21} parameter refers to the ratio of the output signal from port 2 on the AUT (Tx) to the input signal on port 1 (Rx) on the receive antenna as illustrated in Figure 73. The receive antenna used is the Mini-Bicon 3180B with conical elements, which is rated for a 30MHz-3GHz frequency range (Ref. 20).

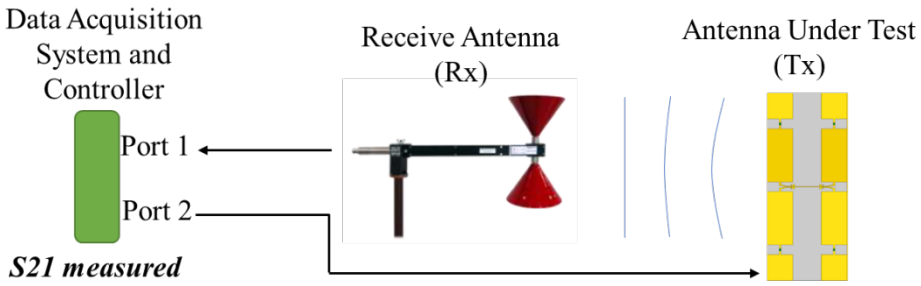

Figure 73: S_{21} Measurement Test Set Up Schematic

The gain of the UWB MCoRDS antenna was calculated using Equation 2. The S_{21} was measured between the AUT and receive antennas, and between a reference antenna and the receive antenna. This equation is applicable since the gain of the reference antenna is known, and because the receive antenna, the frequency range and the distance between antennas are kept the same. The reference antenna used was the 3142C BiConiLog which is rated for 26 MHz-3 GHz frequency range (Ref. 21).

$$Gain_{AUT} = Gain_{reference} - 20\log_{10}(|S21_{reference\ to\ receive}|) + 20\log_{10}(|S21_{AUT\ to\ receive}|)$$

Equation 2: UWB MCoRDS Antenna Gain Calculation in dB Units (Ref. 22)

The curvature of the antenna was controlled with three electromagnetically transparent foam test stands, each with different curvature (1 in. or 25.4 mm, 0.4 in. or 10.2 mm and flat). These set the antenna at the ground plane distance used in simulations as shown in Figure 74, which provides consistency between experimental and simulation analyses.

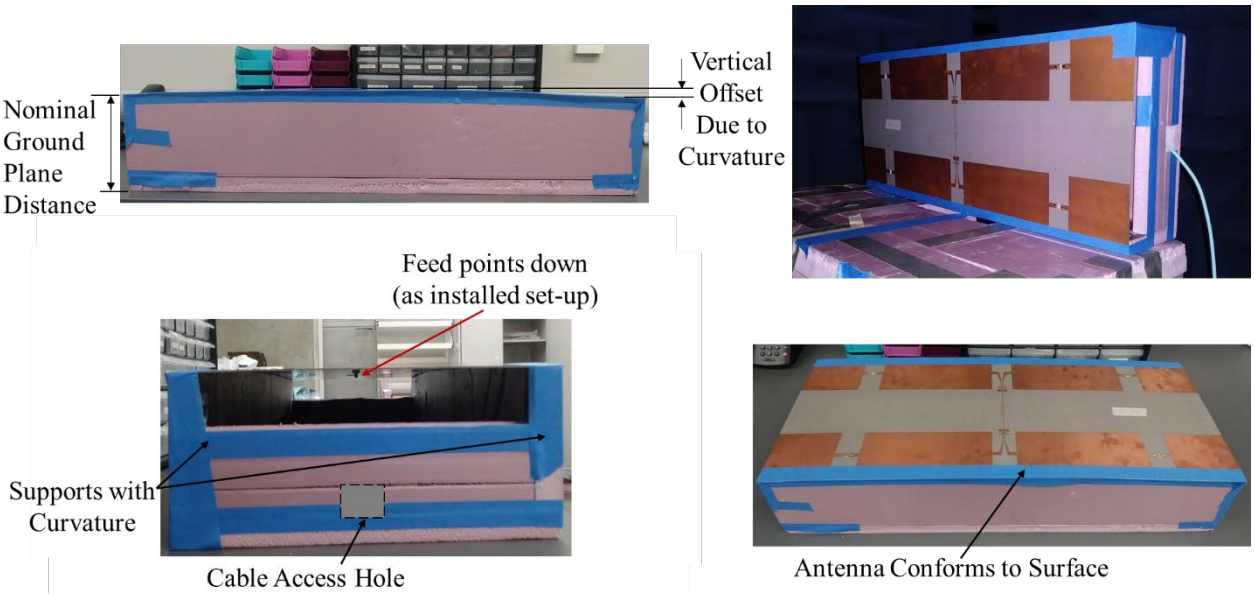

Figure 74: Test Stands to Conform Antenna

A ground plane made of foam and aluminum tape on one surface was attached to the back and flat surface of the test stand. The author positioned the ground plane with respect to the antenna as close as possible to the HFSS positions shown in Figure 28.

7.2. Experiment Return Loss

The return loss measurements were obtained using 1601 points in the 30MHz-1GHz frequency range. The signal cable was calibrated using an N4433A electronic calibration kit. Figure 75 presents the experiment and simulation return loss results for a flat antenna including the substrate and the ground plane.

The experiment results indicate that the antenna is less than 90% effective in transmitting power in the 202-298 MHz range, with a minimum of -8.4 dB (86%) at 245 MHz which is still practical. The differences between experimental and simulation results could be attributed to errors introduced with the test set-up (i.e. the presence of cables to provide power to the antenna and of the test stand to support the antenna, and the condition of the cable and connectors that could cause undesired reflections and reductions in performance), and ideal material properties assumed in simulations.

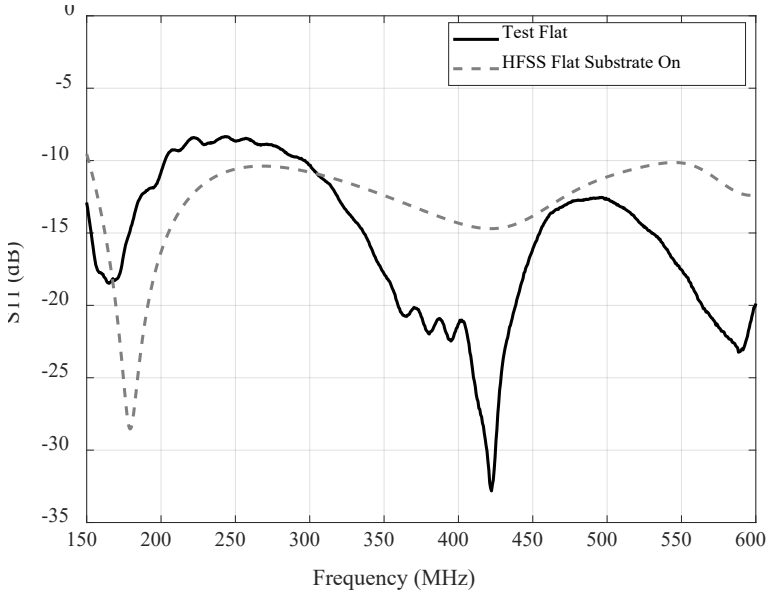

Figure 75: Measured vs. Simulated Return Loss of UWB MCoRDS Antenna

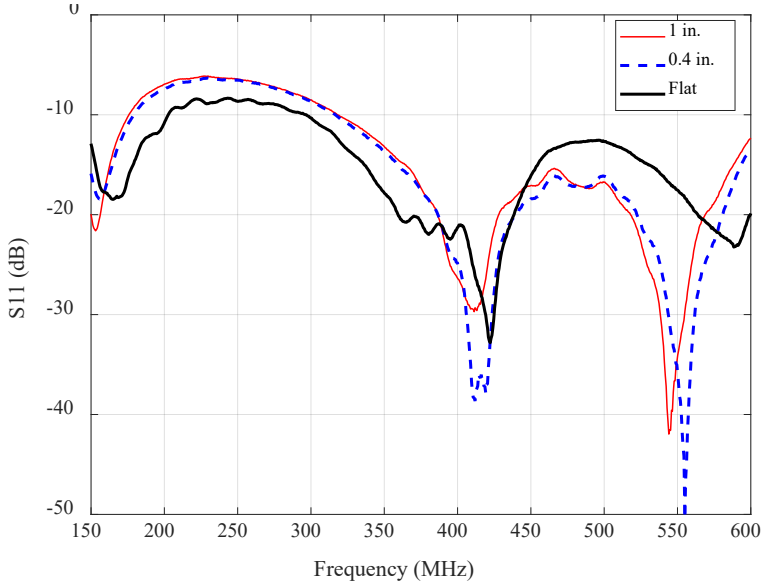

Figure 76: Measured Return Loss of Bare UWB MCoRDS Antenna

Figure 76 shows the experiment return loss results for all curved antenna configurations. It is observed that curving the antenna by any amount, the signal shifts to the left. This is in accordance with the simulation results. This shift is larger for the 1in. configuration than the 0.4 in. Curving the antenna also results in a reduction in the 175-316 MHz range where the maximum amount of energy transmitted is 76% (-6.125 dB) which is not preferred, but can be overcome with solution

strategies discussed in the following chapters. Overall, the response of the 1 in. and 0.4 in. experiment results approximate highly.

7.3. Calculated Gain from Experiment Measurements

The experimental antenna gain at nadir is calculated using Equation 2, the pattern measurements shown in the following sub-chapter, and the gain of the reference antenna. The experimental pattern results were carefully evaluated to identify the actual nadir direction since during the tests the antenna can be easily offset a few degrees from nadir. The orientation of the pattern results for each test was corrected with the corresponding offset angle to obtain actual nadir results. However, although this was carefully performed, it is also possible source of error. The following figures show the calculated gain at the same frequencies analyzed in previous chapters. Figure 77 shows the calculated versus the simulated gain results for a flat UWB MCoRDS antenna with a ground plane and an active substrate.

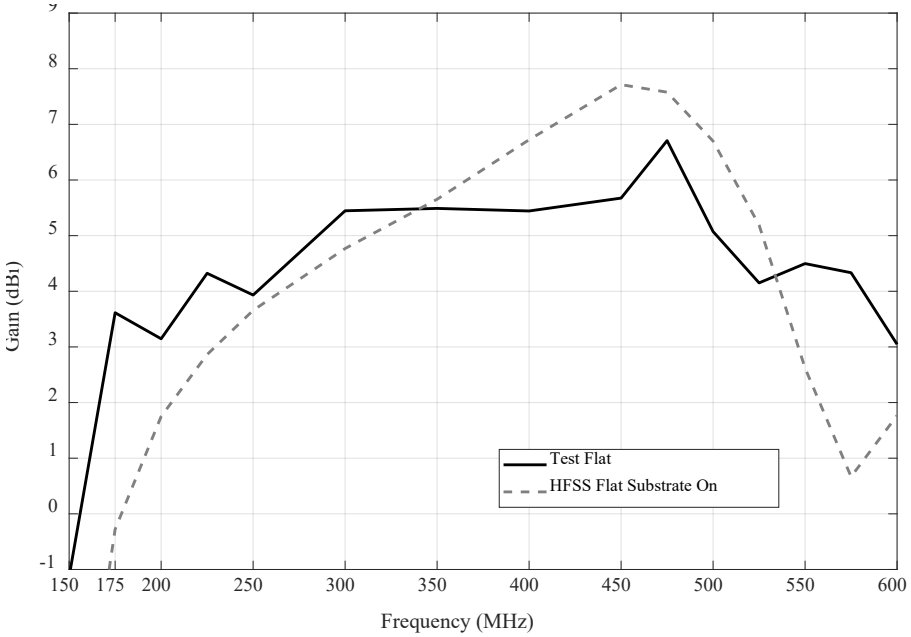

Figure 77: Calculated vs. Simulated Gain of UWB MCoRDS Antenna at Nadir

The calculated gain or "test flat" trend has a similar trend compared to the simulation results. The experiment results show larger gain in the 150-350 MHz and 525-600 MHz range. The useful frequency range is increased by 25 MHz since the gain is 0 dBi shortly after 150 MHz, and no

sudden drops in gain are observed at 575 MHz. The calculated gain results show a maximum at 475 MHz with 6.7 dBi whereas the simulation results show a maximum of 7.7 dBi at 450 MHz. The difference between experimental and simulation results are also attributed to errors introduced with the test set-up, ideal material properties assumed, post-processing errors to find the actual nadir orientation, and the accuracy of the gain values of the reference antenna used in the calculations.

Figure 78 shows the calculated gain results for the different curved antenna configurations. It can be observed that adding curvature to the antenna increases the gain below 225 MHz, for 325-400 MHz and above 575 MHz. Curvature has negligible effects in the 225-325 MHz frequency range and is detrimental to the antenna performance in the 400-575 MHz range. Additionally, smaller changes in gain are observed for 0.4 in. (10.2 mm) compared to 1 in. (25.4 mm). Finally, the curved antenna results diverge from the flat antenna results more significantly at or near 350 MHz. These observations are in accordance with the simulation results.

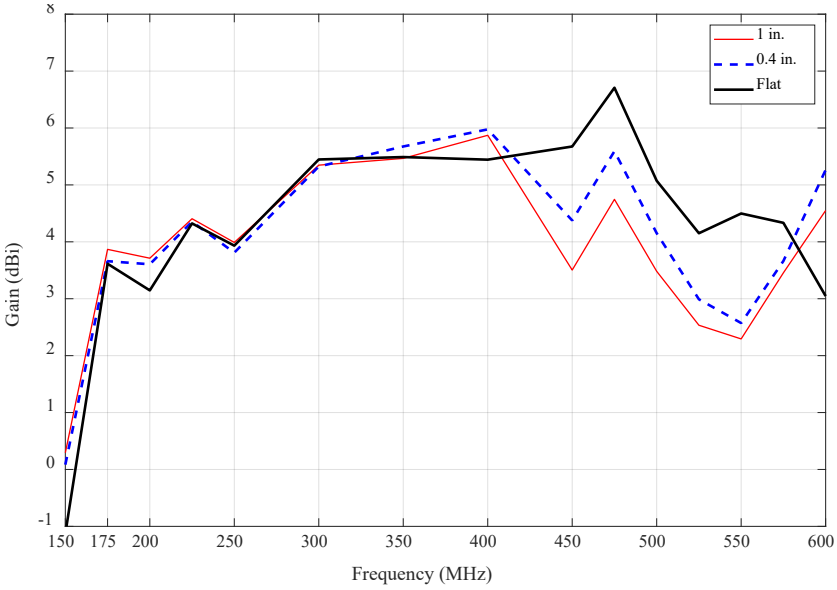

Figure 78: Calculated Gain of UWB MCoRDS Antenna

7.4. Experiment Radiation Intensity Patterns and HPBW

Antenna patterns were obtained at frequencies specified by the author of this thesis to also aid in the calculation of gain results shown in the previous sub-chapter. The long dimension of the UWB

MCoRDS antenna was oriented horizontally to obtain the along track patterns, and rotated by 90° (long dimension oriented vertically) to obtain cross-track radiation patterns. In all cases, the phase center of the antenna was maintained at 50 inches and all measurements include the effect of the ground plane.

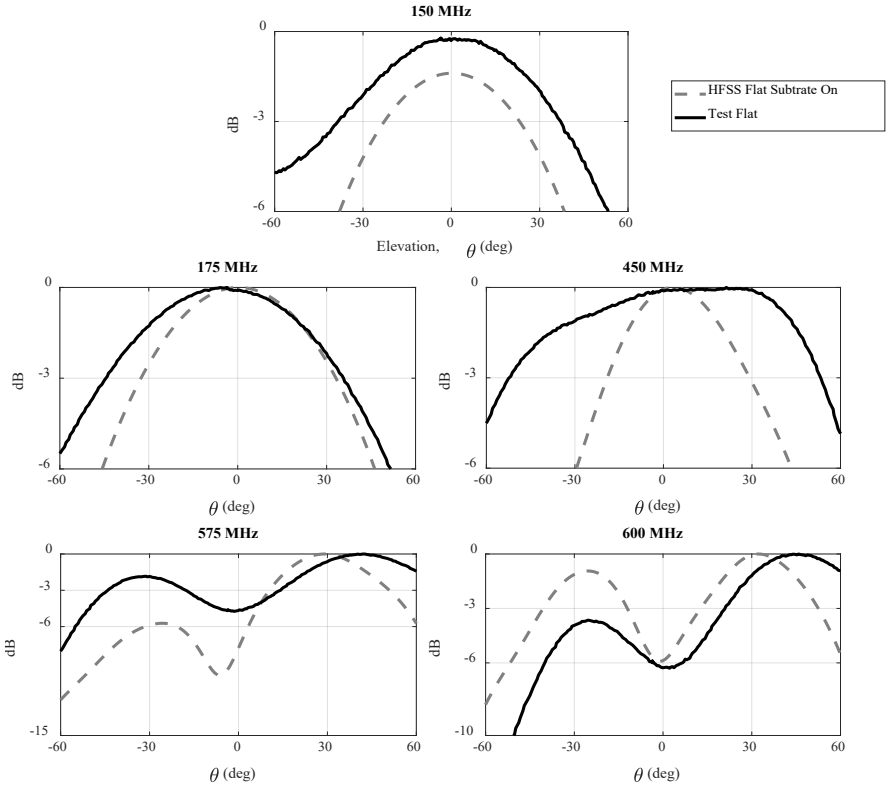

Figure 79: Measured vs. Simulated Normalized Pattern at φ = 0° (along-track)

Figure 79 shows the normalized measured and simulated flat antenna pattern results in the along-track orientation. It is important to notice that all results are normalized with respect to the maximum dB value which is equal to the nadir value at most frequencies. The exception is evident at the frequency of 150 MHz, at which the maximum dB value occurs in the direction opposite to nadir (back lobe).

The general form of the main beam is similar between measured and simulated results at all frequencies. However, for frequencies below 450 MHz, the measured results show that the antenna has a wider beam. At 575 MHz, the test results show that the left peak at -30° does not reduce as

significantly with respect to the right peak at 30° as in the simulation results. The opposite occurs at 600 MHz. In both measured and simulation results, the right peak at 30° has the least variation.

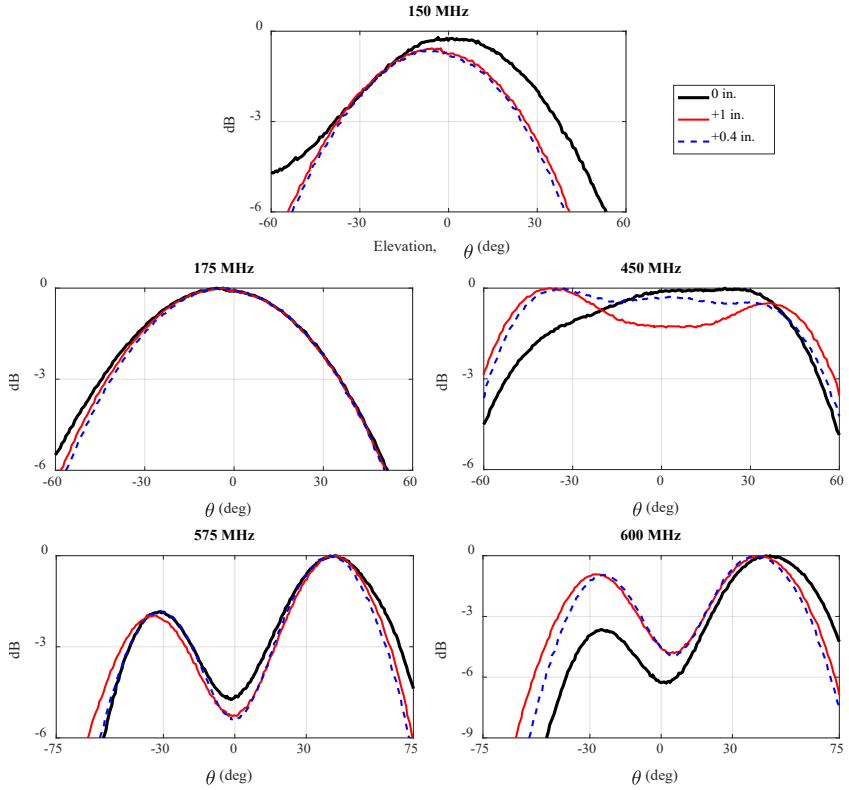

Figure 80: Measured Normalized Pattern at φ = 0°

Figure 80 shows the measured along-track patterns for different curved antenna configurations. Generally, the curved antenna patterns follow similar trends as the flat antenna results. At 150 MHz, the incorporation of any curvature reduces the main beam width and peak level. Differences between 0.4 in. and 1 in. are negligible. At 175 MHz, differences between the different curved antenna configurations are negligible. At 450 MHz, adding curvature to the antenna widens the main beam and reduces the dB level at nadir which results in peaks at approximately +/- 40°. The reduction is larger for 1in. than for 0.4 in. At 575 MHz, the two curved antenna cases result in approximately the same reduction of the dB level at nadir and narrowing of the beam at 40°. The left beam at -35° remains unchanged for 0.4 in. but is widened for 1 in. curvature. Finally, at 600 MHz the dB level at nadir increases when the antenna is curved with negligible differences

between the 0.4 in. and 1 in. cases. The left peak at -30° increases significantly and also widens (higher effect with larger curvature). The right peak at 45° becomes narrower.

Figure 81 presents the test and simulation antenna pattern results at the cross-track orientation. Similar to the along-track results, the general shape of the main beam is similar between test and simulation results for 450MHz or lower. The test results indicate that the main beam is wider, mostly at 150 MHz frequency at which also a significant increase in the peak level is observed.

For 575 MHz and 600 MHz, the antenna pattern obtained from measurements has a different shape than that obtained from simulations. One peak instead of two are observed in the test results. However, this peak approximates the right peak of the simulation results. At both frequencies, the main beam width is significantly lower compared to the simulation results.

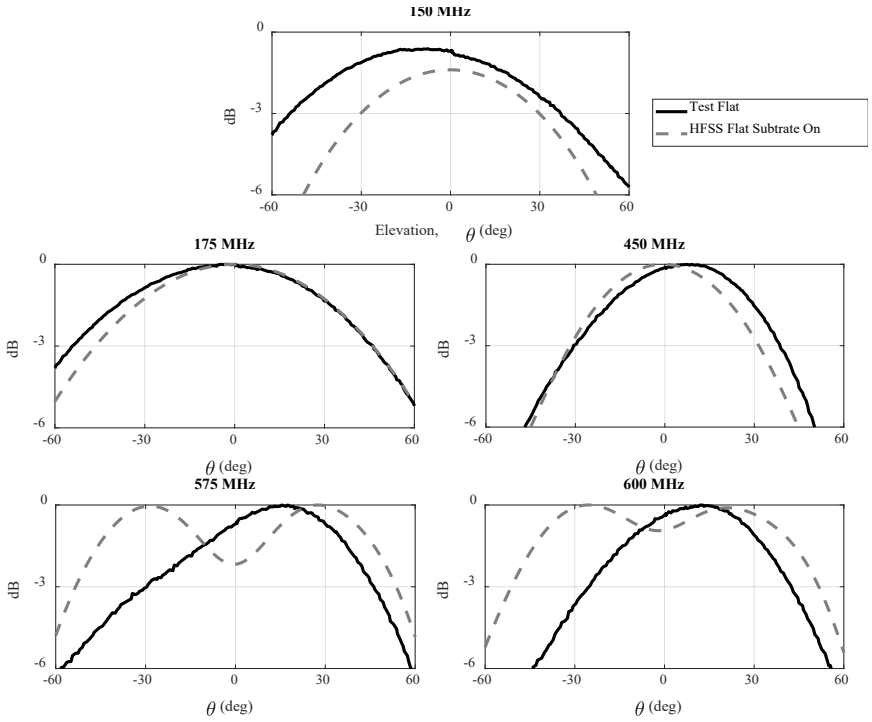

Figure 81: Measured vs. Simulated Normalized Pattern at φ = 90° (cross-track)

Figure 82 shows the HPBW corresponding to the cross-track antenna patterns shown above. The changes in HPBW are negligible in the 225-500 MHz range, large below 225 MHz, and considerable above 500 MHz. The latter one is caused by the difference in shape of the main beam.

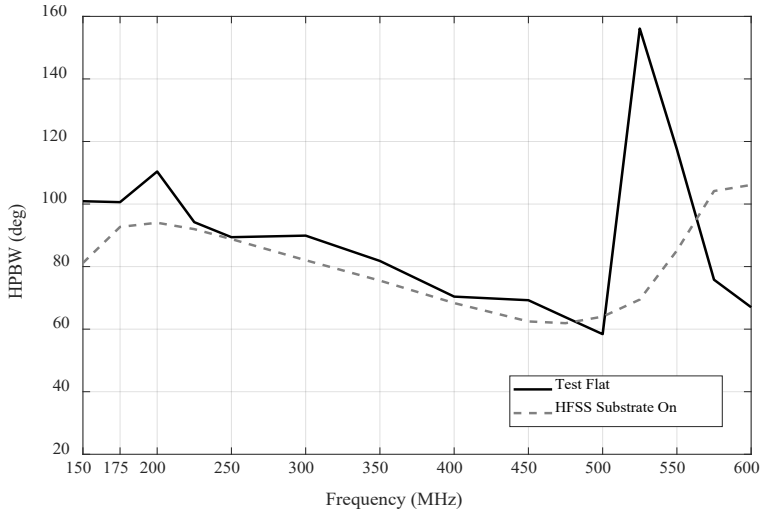

Figure 82: Measured vs. Simulated HPBW at φ = 90°

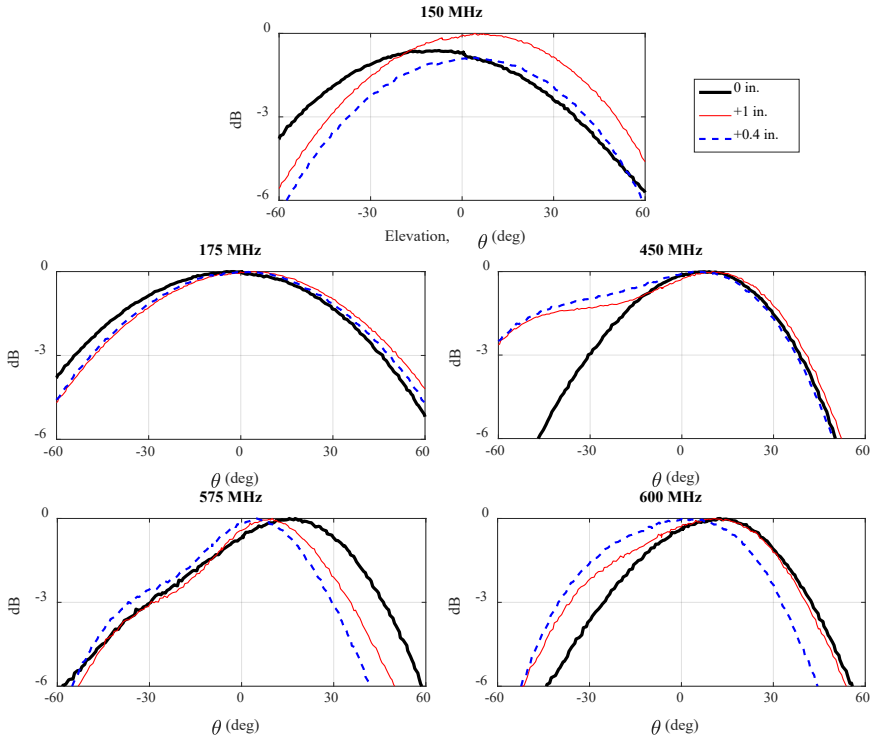

Figure 83: Measured Normalized Pattern at φ = 90°

Figure 83 shows the antenna pattern results for all curved antenna cases. The shapes of the main beams between the curved cases and the flat case at all frequencies are similar except at 450 and 600 MHz. At these frequencies, the main beam widens significantly on the left side. This effect is

much more significant at 450 MHz than at 600 MHz. At 150 MHz, the normalized main beam level either remains the same or increases with curvature, but it is approximately unchanged for all other frequencies. At 175 MHz, the differences between the curved and flat cases are negligible. At 575 MHz, the main beam width is reduced when the antenna is curved.

Figure 84 shows the HPBW at the cross-track orientation for all curved antenna cases. These agree with the observations written above and show that the HPBW for curved antennas varies by small amounts or negligibly at the 200-400 MHz range. In this range, these observations are also in accordance with the results presented in Chapter 6 since the change in HPBW due to a 0.4 in. curvature was small or negligible.

The largest differences occur above 400 MHz. At 475-500 MHz, the curvature widens the beam by more than 20°. For 500-500 MHz, the curvature reduces the beam width by 20°-60°. These observations are not consistent with the simulation results of Chapter 6 since curvature was expected to increase the beam width at all frequencies.

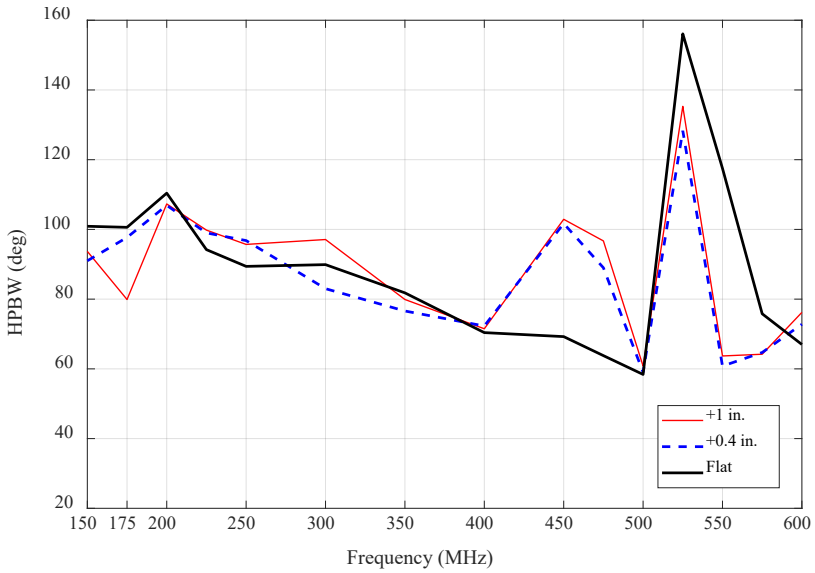

Figure 84: Measured HPBW at φ = 90°

7.5. Summary and Assessment of Experimental Results

The experimental results are approximate to the simulation results. The differences between curved and flat cases observed in simulations are generally the same as those observed in the test results.

The main deviation from the simulation results is observed for the cross-track antenna pattern at frequencies higher than 475 MHz. The deviations from the simulation trends are attributed to the following factors:

- Manufacturing tolerances on the fabrication of the antenna;
- Ideal properties assumed in HFSS which do not take into account possible experimental impedance mismatch losses among others;
- Possible misalignments when placing the transmitting antenna into position and when correcting the orientation of the pattern results to show the actual nadir direction;
- Presence of other components, such as cables, connectors, and the test stand, during the test which were not included in the simulations;
- Sensitivity of the antenna model to the other the frequency solution defined in HFSS and to the size of the vacuum box.

The experiment results show that the change in antenna performance due to curvature is frequency dependent, and that the antenna is less sensitive to changes in performance in approximately the 175-400 MHz range which is in agreement with all the results previously observed in this document. These results are evaluated using the radar range concepts presented in Chapter 8 to determine the curvature effect on the radar system rather than on the single antenna.

8. Assessment of Influence of UWB MCoRDS Antenna on Radar System Performance

The performance of the radar system is dependent on the various characteristics of the system. These include the components of the radar range equation, signal generation, and signal post-processing techniques among others. Additionally, the performance is dependent on the target of interest (small object or a large field), environment conditions (rain, temperature, etc.), the position of the transmitting and receiving elements with respect to each other (monostatic or bistatic), and the motion of Tx and Rx components (located in moving aircraft or static on ground). The individual performance of each variable is maximized for altimetry applications to measure snow and ice. Hence, maximizing the performance of one antenna element allows maximizing the performance of the overall system.

This chapter analyzes the influence of the changes in antenna performance due to curvature in the capability of the radar system. This is done by evaluating the components of the radar range equation which are explained in sub-chapter 8.1, and by analyzing the curvature effects in the performance of an antenna array instead of a single antenna as explained in sub-chapters 8.2 and 8.3.

8.1. Radar Range Equation for Extended Targets

Mapping snow and ice from an aircraft relates to the measurement of areas (extended targets) rather than point targets. For this, the radar range equation for extended targets is used to define the relationship between the system characteristics and performance as shown in Equation 3. The radar range equation for extended targets relates the power received (P_r) to the power transmitted (P_t) with the influence of: the wavelength of interest (λ), the gain of both receive (R_x) and transmit (T_x) antenna elements, the system's spatial resolution (ΔA) which is also dependent on the bandwidth (B) or pulse duration (τ_p), the backscattering characteristics of the terrain (σ^o), and the slant range (R) which is the height from ground to the elements in nadir looking applications.

$$P_r = \frac{\lambda^2 P_t G^2 \sigma^o \Delta A}{(4\pi)^3 R^4}$$

Equation 3: Radar Range Equation for Extended Targets (scalar units) (Ref. 23)

Where the backscattering coefficient is approximately constant for homogeneous extended area targets (ice and snow), but is still dependent on elevation angle, azimuth angle, and polarization. The gain is also a function of elevation and azimuth angles.

$$\Delta A = \Delta x \cdot \Delta y$$

Equation 4: Radar system's spatial resolution (Ref. 23)

$$\Delta x = \frac{c\tau_p}{2sin\theta}$$

Equation 5: Cross-track ground range resolution (Ref. 23)

$$\tau_p \cong \frac{1}{B}$$

Equation 6: Pulse duration and Bandwidth relationship (Ref. 23)

$$\Delta y = \beta_{az} R$$

Equation 7: Along-track ground range resolution (Ref. 23)

In dB units, the influence of each component of Equation 3 in the received power is more evident as shown in Equation 8. Below the ΔA has been replaced by Δx and Δy, thus the R^4 is simplified to R^3.

$$P_r(\text{dBm}) = 2 \cdot \lambda(dB) + P_t(dBm) + 2 \cdot G(dBi) + \sigma^o(dB) + \text{c}(dB) + \beta_{az}(dB) - 3 \cdot 4\pi\ (dB) - 3 \cdot R(dB) - B(dB) - 2sin\theta(dB)$$

Equation 8: Radar range equation for extended targets in dB units

Based on Equation 8 above, the transmitted power influences the received power by a factor of one, the antenna gain by two, the azimuth half power beam width by one, and the slant range by three. Other components are also dependent on the ground location being measured (incidence angle and along track position), which relate to radiation intensity patterns.

8.2. Antenna Array Considerations

The radar range equation for extended targets explained in the previous sub-chapter is applicable to one antenna. However, the large beam width of the antenna can result in large amounts of interference noise due to the reflections from non-nadir radiated regions. This means that left from right targets cannot be distinguished from each other. Interfering signal levels can be reduced with

an antenna array which results in a more directive nadir beam. If other than nadir regions were of interest, the main beam could be rotated using phase scanning array concepts.

Only individual antenna results have been discussed in this document; however, the author considers necessary to study the influence of the radar range equation components on the radar system by using the array results rather than the single antenna results. Ideally, measured or simulated array results would be used for this. Measured results imply the use of multiple antennas, but only a single antenna was available for testing. Thus, simulating an array is preferred; however, actual array models could not be successfully ran by the software. For these reasons, mathematical expressions are applied to the simulated and measured results of a single antenna to obtain synthetic array gain and radiation patterns.

The UWB MCoRDS array has eight elements aligned along the Y axis and with a constant element spacing (d) of 18.4 in. (0.468 m) as shown in Figure 85.

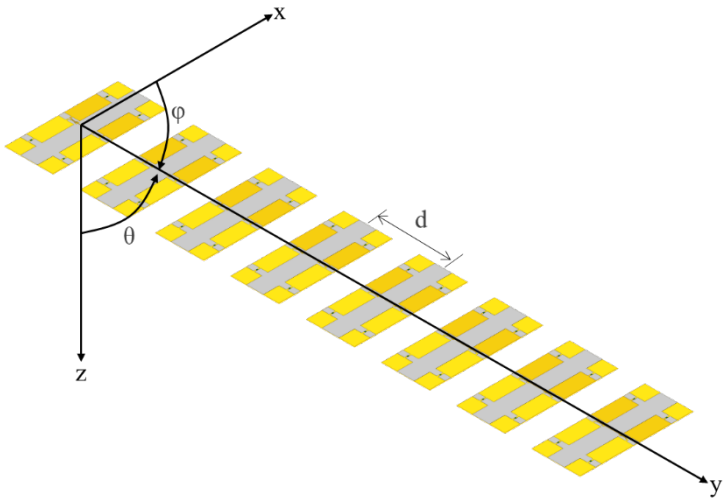

Figure 85: UWB MCoRDS Eight Element Antenna Array along Y Axis, d = 18.4 in or 0.468m

The array factor is defined in Equation 9 for N=8 number of antenna elements. This is calculated for different frequencies and elevations angles assuming that nadir ($\theta_o = 0°$) is the observation direction using Equations 10, 11 and 12. Equation 12 represents the dot product of the unit vector along array axis (y) with the unit vector directed toward the observation point.

$$AF = \sum_{n=1}^{N} e^{j(n-1)\psi}$$

Equation 9: Array Factor Equation (Ref. 24)

$$\psi = kdcos\gamma + \beta_{\theta_o=0^\circ} = 0 \rightarrow \beta = -kd$$

Equation 10: Array Factor Equation Component (Ref. 24)

$$k = \frac{2\pi f}{c}$$

Equation 11: Wave Number (Ref. 24)

$$\cos\gamma = \hat{a}_y \cdot \hat{a}_r = \sin\theta\sin\phi$$

Equation 12: Dot Product Along Y Array Axis (Ref. 24)

The calculated array factor is multiplied with the antenna patterns to obtain the antenna array patterns. The antennas aligned along the Y axis mainly have an effect on the cross-track radiation pattern resulting in a more directive (narrower) main beam width.

Figure 86 shows the calculated cross-track radiation pattern using the measured single antenna results multiplied by the calculated array factor which was obtained using the equations above. It is evident that the side lobes are significantly reduced with respect to the main lobe, and that the main lobe is more directive (narrower). This is also observed in Figure 87. The HPBW shows that the width of the main lobe reduces with increasing frequency, and that the curvature of the antenna has negligible effects on the radiation patterns in difference to the frequency dependent effects for a single antenna presented in previous chapters.

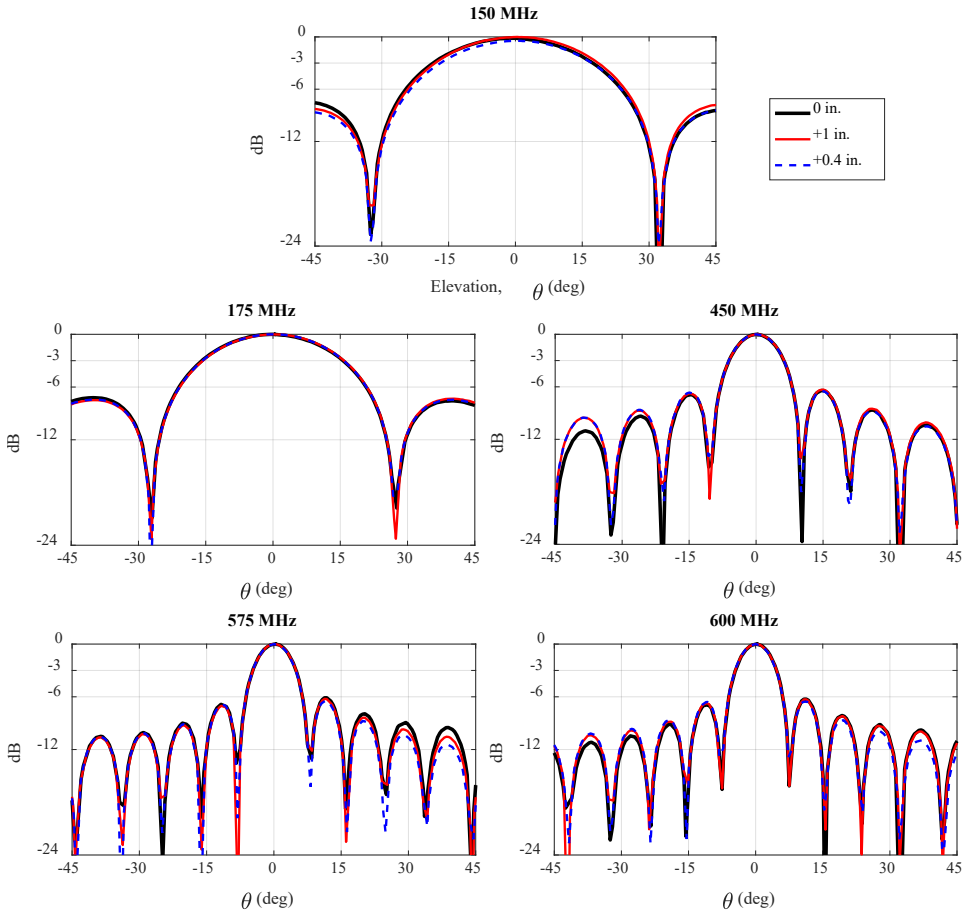

Figure 86: Normalized Measured Pattern with Array Factor, φ=90°

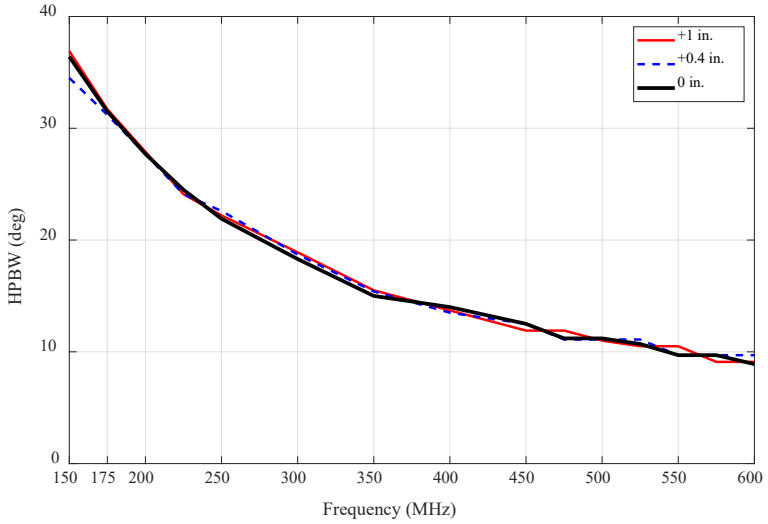

Figure 87: HPBW from Measured Patterns with Array Factor, φ=90°

The results presented above are also in accordance with the in-flight radiation pattern measurements of the fuselage sub-array presented in Figure 4 of Reference 3. These correspond to the Spring 2016 campaign with the BT-67 aircraft over Greenland. A comparison of the half power beam widths of the nadir peak are shown in Table 13 for the frequencies specified in Reference 3. The calculated results are good agreement with the inflight measured results from Reference 3. Small differences between the results are attributed to possible manufacturing inconsistencies of the antenna, the effect of the dielectric radome which is not accounted for in the "calculated" column, and coupling effects between antennas not obtained with the array factor.

Table 13: Cross-Track HPBW with Array Factor vs. In-Flight Measurements

Frequency	HPBW (deg)	
MHz	Calculated	Reference 3
194	28.8	22.6
244	22.7	20.5
294	18.4	17.4
344	15.4	14.2
394	13.5	13.2
444	12.3	11.9

The antenna array gain is also calculated using the array factor equation. At nadir (θ=0°), the antenna array factor is always equal to 8 (9 dB) disregarding the φ value. This array factor makes sense since the gain increases by 3 dB each time the number of antenna elements double:

- Increase from 1 to 2 antennas = +3 dB;
- Increase from 2 to 4 antennas = +3 dB;
- Increase from 4 to 8 antennas = +3 dB;
- Increase from 1 to 8 antennas = +9 dB.

In dB scale, the array factor of 9 dB is added to the gain obtained through measurements. The antenna array gain is shown in Figure 88. In difference to the radiation results, where the shape of the radiation patterns changed for an array, the gain results show the same trends as the single antenna gain results but have higher magnitudes.

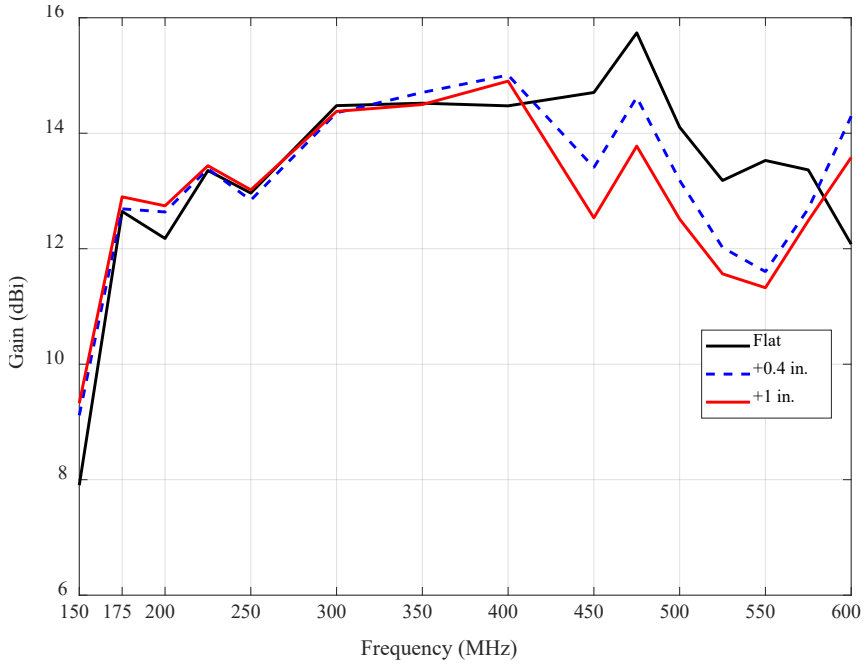

Figure 88: Measured Gain with Array Factor

The array factor was also applied to the single antenna simulation results. The resulting antenna array gain and radiation patterns are shown in Appendix D.

The return loss of the array (active S_{11}) is also influenced by the number of elements and can differ from the single antenna trend. Differences can be caused by reflections from adjacent elements and element coupling. However, this is complex and cannot be calculated using the array factor. This must be obtained through either measurements or simulations. Nevertheless, the S_{11} of each antenna is below -10 dB across most of the frequency range of interest, hence it provides confidence in the robustness of the system. For assurance, the author recommends simulating and measuring the antenna array.

8.3. Influence of UWB MCoRDS Antenna Performance

The components of the radar range equation are helpful to assess the results presented in this document and to determine strategies to overcome any losses added by curving the antenna. These are discussed considering the antenna array results presented in the previous sub-section.

As previously observed, the antenna curvature mainly has an effect in the array gain. The nadir gain of the antenna either shows negligible changes or increases due to curvature below 400 MHz and above 575 MHz. The gain reduces with curvature for 400<f<575 MHz frequency range. This is detrimental to the measurement of the ice sheets which had been previously measured using a 150-520 MHz chirp transmit waveform in the 2016 spring mission (Ref. 3). The maximum negative change in gain due to the supercritical airfoil curvature (0.4 in. trend) is 1.93 dBi at 550 MHz. This equals to a reduction of 3.86 dB for the whole system as the change in gain is multiplied by two as shown in Equation 8. Additionally, reductions of gain at higher frequencies are more relevant than at lower frequencies since the wavelength term in the radar range equation results in negative dB values at higher frequencies as shown in Figure 89.

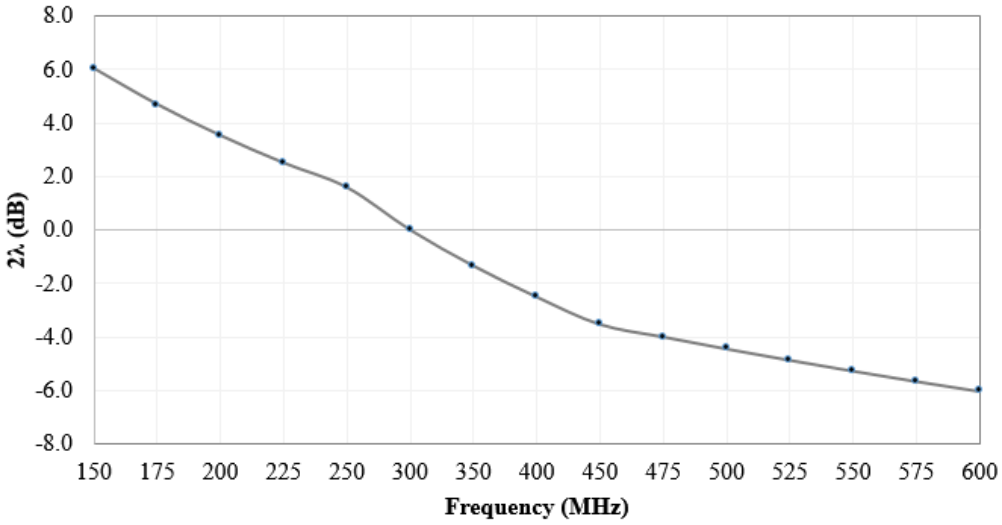

Figure 89: Frequency vs. Value of First Term in Radar Range Equation

The reduction in gain can be lessened by reducing the flight altitude from the nominal 1640 ft. (500 m) used in past missions (Ref. 3), by increasing the transmit power or by a combination of both. The range (R) term in the radar range equation is multiplied by negative three, thus any reduction in aircraft altitude can result in higher receive power. The nominal aircraft altitude is equivalent to 26.99 dB and to 26.02 dB for 1312 ft. (400 m). Reducing the flight altitude by 328 ft. (100 m) results in a 0.97 dB difference, which equals to a 2.9 dB improvement in the received power by taking into account the -3 multiplier.

A 500 W or 1000 W transmit signal power was used in past missions (Ref. 3). Depending on the system design, if 500 W (57 dBm) were used this could be increased to 1000 W (60 dBm) to obtain an increase in receive power by 3 dBm. However, increasing the transmit power results in higher costs and could add complexity to the system. Hence, the need for compensating for the reduction in gain at higher frequencies should be carefully evaluated by the radar system designers.

Based on the results presented above, the author of this thesis recognizes that the advantage of having more antenna elements outweighs the detrimental electromagnetic effects of conforming the antenna to the supercritical airfoil curvature. This means that having more curved antenna elements results in better electromagnetic performance than having a smaller number of flat elements (which would be required to obtain a structurally feasible radome with effective aerodynamic performance while keeping the top and bottom radome surfaces flat).

9. Conclusions and Recommendations

The following conclusions are derived from the work presented in this thesis:

1. A structurally and aerodynamically feasible new radome that accommodates eight UWB MCoRDS antennas requires significantly reduced loads based on the background studies. It was speculated that re-shaping the radome cross-section to more aerodynamically effective shapes (reducing the maximum depth of the cross-section, reducing the depth of the trailing edge, and using supercritical airfoil shapes) would reduce the loads significantly. Two dimensional CFD analyses indicate that maintaining the shape of a supercritical airfoil SC0010 (appropriate for transonic flight) on the full radome cross-section outweighs the influence of the total radome depth on reducing the aerodynamic loads.

   CFD results show that the drag, and magnitude of the pressure loading and Mach number are significantly reduced (22% less drag) by maintaining the SC0010 airfoil shape despite that the radome depth (9.8 in. or 0.25 m) is 22.5% larger than the depth of the radomes with flat top and bottom surfaces studied in sub-chapter 2.2 (8 in. or 0.2 m). Additional findings indicate that the magnitude and location of the shockwaves have a larger influence on drag (+ 90%) compared to the flow separation caused by the depth of the trailing edge (< 2%). A radome with flat top and bottom surfaces and with a short (1.5 in. or 38 mm) TE results in a reduction of 2 drag counts compared to a similar profile but with a taller TE (5.3 in. or 0.13m). But a radome with a supercritical airfoil shape and taller TE (2.75 in. or 70 mm) that creates small shedding vortices results in a reduction of 24 drag counts of wave drag.

2. It was expected that changes in the radome geometry (reducing the cross-section depth and maintaining the airfoil curvature rather than flattening at the location of the antenna) would result in negative changes in antenna performance. Extensive simulation studies showed that changes in the single antenna electromagnetic performance due to ground plane distance and curvature are frequency and electromagnetic parameter dependent.

   It was hypothesized that the effect on antenna performance due to curved ground plane or curved antenna was mainly due to the average ground plane distance across the length of the antenna. Curved ground plane and curved antenna studies in comparison to flat ground

plane studies indicate that changes in antenna performance due to curvature are mainly due to the ground plane distance at the location of the feed. These effects are more evident for larger curvatures or ground plane distances.

For the UWB MCoRDS antenna, it was found that increasing or decreasing the effective ground plane distance by +/- 30 mm (1.18 in.) or less minimally impacts the return loss of the single antenna. The response is maintained under or close to the -10 dB limit across the 150-600 MHz frequency range.

Examination of the simulated gain results indicates that smaller ground plane distances reduce the gain for $f \leq 450$ MHz, but improves it for $f > 450$ MHz. The opposite is true for larger ground plane distances (which includes the results for concave ground planes and conformal antennas presented in this document).

The HPBW results also support this finding and show that the UWB MCoRDS antenna is not significantly sensitive to changes in ground plane distance in the 200-400 MHz range. Additionally, it was observed that increasing the ground plane distance at the feed location generally widens the main lobe in both cross-track and along-track directions. The opposite is true for smaller ground plane distances. Results of the concave ground plane and conformal antenna studies suggest that the trends of both cases are similar since both effectively increase the ground plane distance at the feed location.

3. The influence of conforming the UWB MCoRDS antenna to a 91 in. (2.31 m) chord SC0010 airfoil curvature was believed to cause small effects on the antenna performance due to the small vertical offset at the feed location added by the curvature (0.4 in. or 10.2 mm). This was confirmed through electromagnetic simulations in which the curvature resulted in minimal changes to the return loss, less than 0.5 dB change in gain and less than 8 degrees change in HPBW. To verify these results, electromagnetic tests were performed using one bare UWB MCoRDS antenna (not embedded in fiberglass but with the substrate). The differences between curved and flat antenna cases in the experiment approximate the differences between the curved and flat antenna simulation results. However, contrary to the small change in gain observed in the simulations due to the supercritical airfoil curvature, the experimental results show an approximately 1.93 dB reduction in gain at 550 MHz. Additional deviations from the simulation results are

observed on the cross-track antenna patterns at frequencies higher than 475 MHz where the main beam does not have a dip at nadir (preferred). Deviations from the simulation trends are attributed to the ideal properties used in simulations, possible errors introduced by the components of the test set up (internal reflections on cables, reflections due to the presence of a cable on the ground plane, and misalignment of antennas), and the sensitivity of the results to the simulation parameters (vacuum box size and solution frequency) defined in HFSS.

4. The effect of conforming the UWB MCoRDS antenna to the SC0010 airfoil curvature was expected to be negligible when considering the performance of an array with eight elements aligned along the cross-track direction rather than the performance of a single antenna. By applying an array factor, it was observed that the main beam of the cross-track pattern becomes more directive and no significant differences in the normalized cross-track radiation pattern and HPBW among curved and flat antenna cases are observed. But the curvature effects are still evident in the array gain at nadir.

   The examination of the radar range equation for extended targets indicated that the gain is the main term affected by the curvature of the antenna. Based on this, the changes in gain are multiplied by a factor of two which further reduced the performance of the system at higher frequencies. Considering the wavelength term becomes more negative with higher frequencies in dB scale, reductions of gain at higher frequencies became more relevant than at lower frequencies.
5. Having more antenna elements outweighs the detrimental electromagnetic effects on gain caused by conforming the antenna to the supercritical airfoil curvature. An eight element UWB MCoRDS array results in an improvement of gain by 9 dB at all frequencies, while the maximum reduction in gain due to curvature is 3.86 dB at 550 MHz based on the radar range equation. The reduction in gain remains constant despite the number of elements, but each reduction of elements by half results in a 3 dB reduction in gain. Hence, more curved elements are preferred instead of fewer but flat elements.
6. The negative impact of curving the UWB MCoRDS antennas to the supercritical airfoil shape can be overcome by reducing the flight altitude, increasing the transmit power, and applying signal post-processing techniques. These solution strategies are not exclusive

from each other, and can be combined to obtain the best performance. Therefore, the radome design that maintains the SC0010 supercritical airfoil shape is electromagnetically and aerodynamically acceptable, and is expected to be structurally feasible.

The following are recommendations based on the results presented in this thesis:

1. Study the electromagnetic effects due the combination of a curved ground plane and a curved antenna. Individual studies for each configuration indicated that curvature is favorable to antenna gain at lower frequencies, but detrimental at higher frequencies. If the combination of these concepts results in significantly reduced performance at higher frequencies, then having the top surface of the radome as the ground plane would be undesired. But if the performance is enhanced or reset to the performance of a flat antenna with a flat ground plane at the nominal ground plane distance, then it could further reduce aerodynamic loads.
2. Simulate the actual antenna array to obtain the active S_{11} and determine if any negative changes due to coupling and reflections between elements exist. Simulations of the actual antenna could not be completed due to software issues, but these are preferred for better assessment of the radar system performance. To do this, a smaller frequency range could be analyzed or the specific material properties for the ground plane and antenna could be changed to be "perfect electric conductor" (PEC). These would reduce the computation time and power.
3. Perform three dimensional aerodynamic and structural studies of the finalized radome geometry to verify that the structural feasibility of the concept. The concept has been proven to be aerodynamically and electromagnetically acceptable, hence the structural feasibility needs to be verified by performing a detailed structural analysis using appropriate three dimensional pressure distributions. A structurally feasible design would be achieved if all margins of safety are positive, and a total weight reduction exists.

10. References

1. Stocker, T. F., et. al., “Technical Summary - Climate Change 2013: The Physical Science Basis. Contribution of Working Group I to the Fifth Assessment Report of the Intergovernmental Panel on Climate Change,” *Cambridge University Press*, Cambridge, UK, 2013.

2. Arnold, E., et. al., “Radar Sounder Platforms and Sensors at CReSIS,” *IGARSS*, pp. 7902-7905, 2018.

3. Hale, R., et. al., “Multi-channel Ultra-Wideband Radar Sounder and Imager,” *IGARSS*, pp. 2112-2115, 2016.

4. Hale, R., et. al., “Aerodynamic and Structural Analysis of the Basler Fuselage and Wing UWB Antenna Assemblies,” *CReSIS Technical Report*, March 2015.

5. Hale, R., Arnold, E., Lui. W., “Structural Analysis of the MCoRDS Antenna Assembly.” *CReSIS Technical Report*, August 2009.

6. Arnold, E., “Development and Improvement of Airborne Remote Sensing Radar Platforms,” PhD Dissertation, University of Kansas, June 2013.

7. Anon., “DC-8 Airborne Science Experimenter Handbook,” *NASA Dryden Flight Research*, Palmdale, CA, January 2011.

8. Patran/NASTRAN, Version 2018, MSC Software, Newport Beach, CA.

9. Anon., “NACA 0010 Airfoil Coordinates,” *UIUC Airfoil Coordinates Database Website*, [https://m-selig.ae.illinois.edu/ads/coord/naca0010.dat], retrieved 2018.

10. Yang, M., “Aerodynamic Analysis of DC-8 UWB MCoRDS Radome and Technical Consultation,” *DARcorporation*, Lawrence, KS, 2018.

11. Josefsson, L., Persson, P., “Conformal Array Antenna: Theory and Design,” 1st ed., Wiley-Interscience, IEEE Press Series on Electromagnetic Wave Theory, Wiley, Hoboken, NJ, 2006.

12. Redondo González, M. C., “Analysis of Conformal antennas for Avionics Applications,” M.S. Thesis, Chalmers University of Technology, Gothenburg, Sweden, January 2007.

13. Anaekwe, I., Marciano Jr., J. S., “The Effect of Curvature Adaptation on 2.4GHz Rectangular Patch Antennas,” IEEE TENCON 2013 Spring Conference Proceedings, pp. 123-127, 2013.

14. Dahele, J. S., Mitchell, R. J., Luk, K. M., Lee, K. F., “Effect of Curvature on Characteristics of Rectangular Patch Antenna,” Electronics Letters, Vol. 23 No. 14, pp. 748-749, 1987.

15. Noordin, N. H., et. al., “Antenna Array with Wide Angle Scanning Properties,” 2012 6th European Conference on Antennas and Propagation (EUCAP), pp. 1636-1640, 2012.

16. ANSYS Electronics Desktop - HFSS, Version 2016.1, ANSYS, Canonsburg, PA.

17. Harris, C.D., “NASA Supercritical Airfoils, - A Matrix of Family-Related Airfoils,” *NASA Scientific and Technical Information Division Technical Paper 2969*, Langley Research Center, Hampton, Virginia, 1990.

18. Mendoza Strilchuk, P. M., “Structural-Electromagnetic Simulation Coupling and Conformal Antenna Design Tool,” MS Thesis, University of Kansas, March 2018.

19. Siemens NX, Version 12, Siemens Product Lifecycle Management Software, Munich, Germany.

20. Anon., “Mini-Bicon 3180B with Conical Elements User Manual,” *ETS Lindgren Website*, [http://www.ets-lindgren.com/sites/etsauthor/ProductsManuals/Antennas/3180B(1).pdf], retrieved March 2019.

21. Anon., “ETS Lindgren 3142C BiConiLog Antenna Data Sheet,” *Advanced Test Equipment Rentals Website*, [https://www.atecorp.com/atecorp/media/pdfs/data-sheets/ets-lindgren-3142c_datasheet.pdf], retrieved March 2019.

22. Balanis, C.A., “Antenna Theory, Analysis and Design,” *Gain, Realized Gain*, 4th ed., Wiley, Hoboken, NJ, 2016, pp. 61-63.

23. Richards, M.A., Scheer, J.A., Holm, W.A., “Principles of Modern Radar: Basic Principles,” *The Radar Range Equation*, 1st ed., SciTech Publishing, Raleigh, NC, 2010, pp. 59-86.

24. Balanis, C.A., “Antenna Theory, Analysis and Design,” *N-Element Linear Array: Uniform Amplitude and Spacing*, 4th ed., Wiley, Hoboken, NJ, 2016, pp. 293-299.

Appendix A : Increase of Gap – Ground Plane Distance Studies

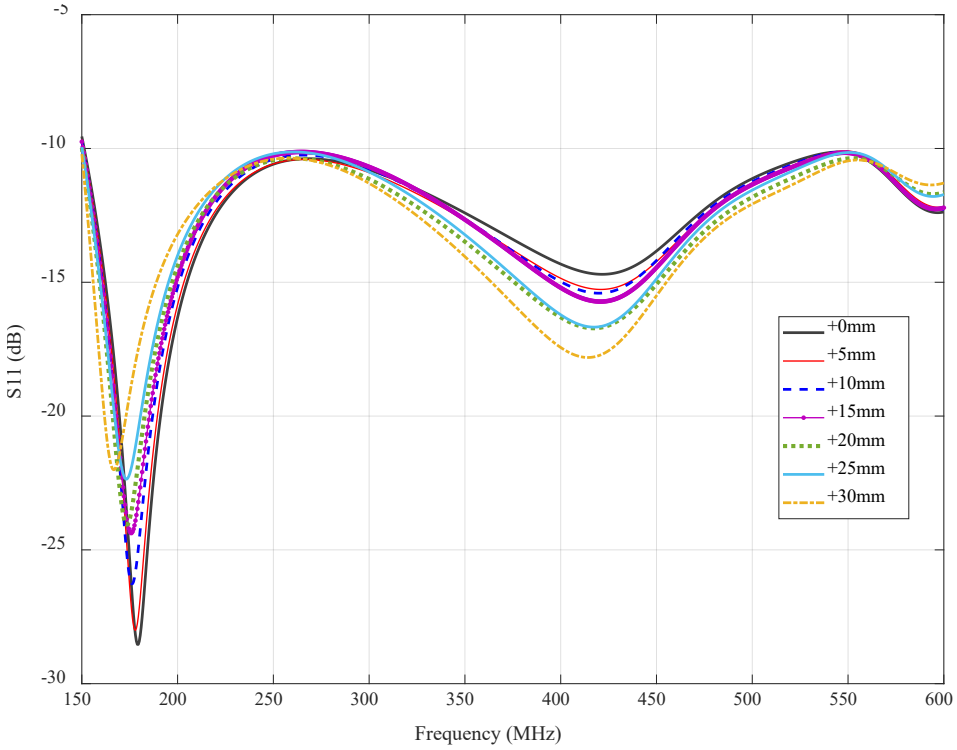

Figure 90: Return Loss Results for Increasingly Larger Ground Plane Distances

Appendix B : Convex Ground Plane Studies

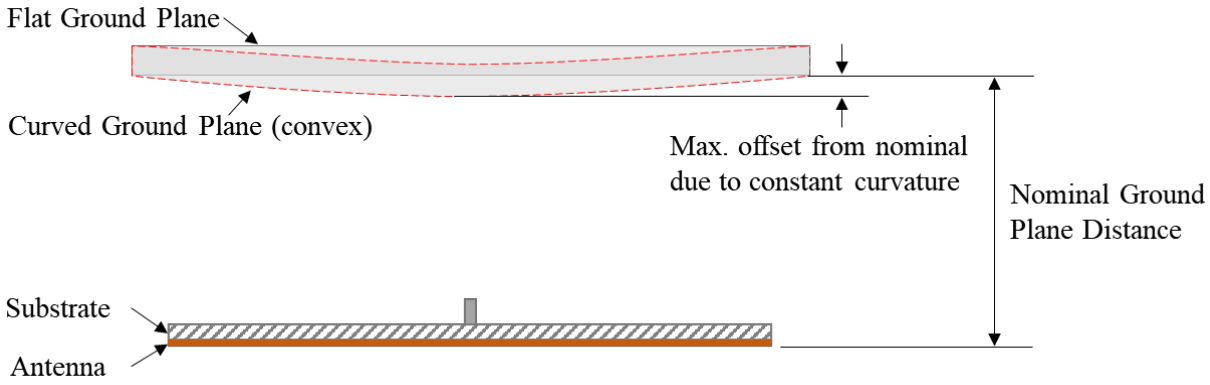

Figure 91: Diagram of Added Convex Curvature to Ground Plane Distance Definition

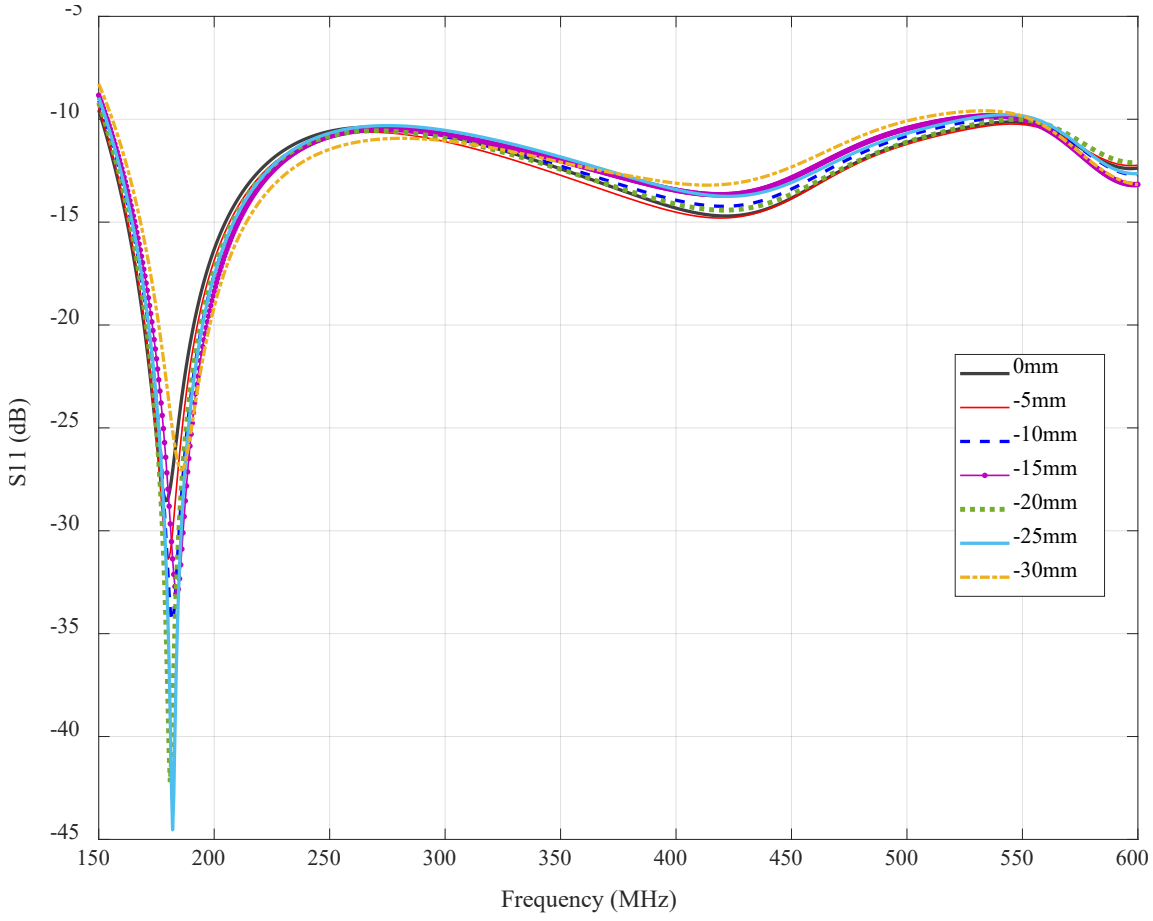

Figure 92: Return Loss Results for Increasingly Higher Convex Ground Plane Curvature

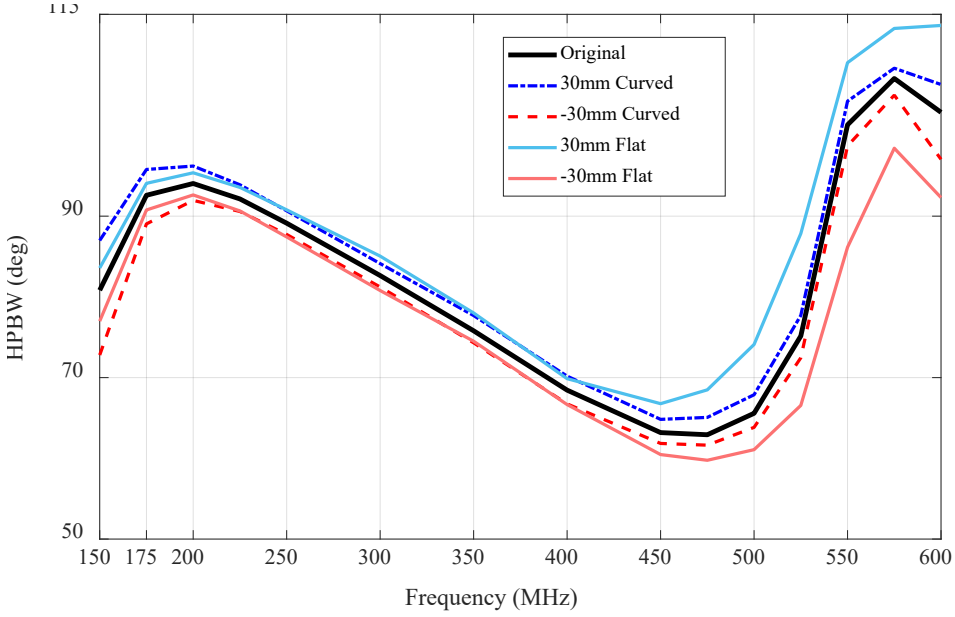

Figure 93: Cross-track HPBW for Curved vs. Flat Ground Planes

Appendix C : Substrate and Ground Plane Effect on Flat Antenna

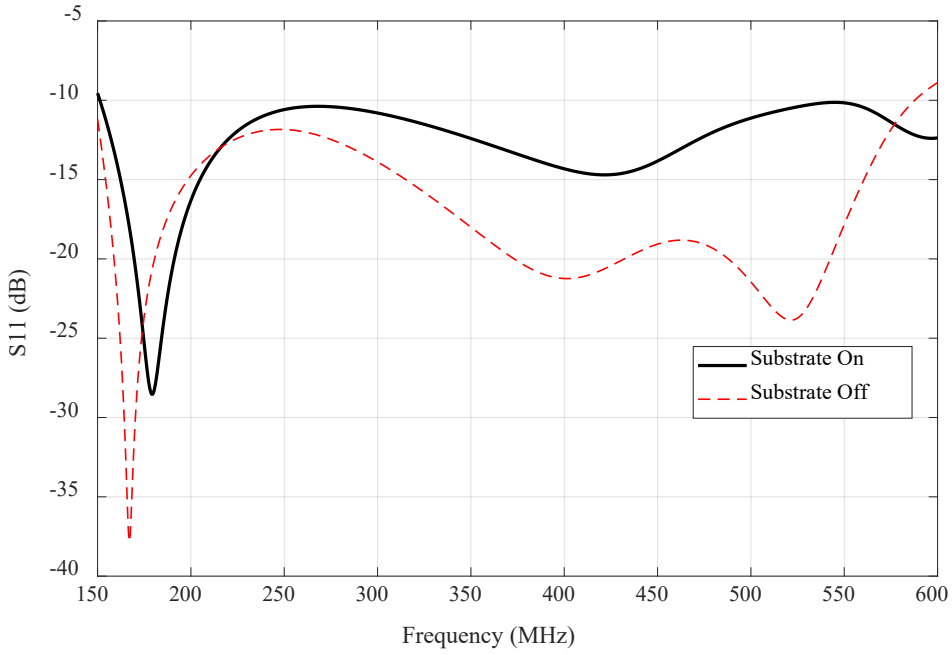

Figure 94: Substrate Effects on Return Loss

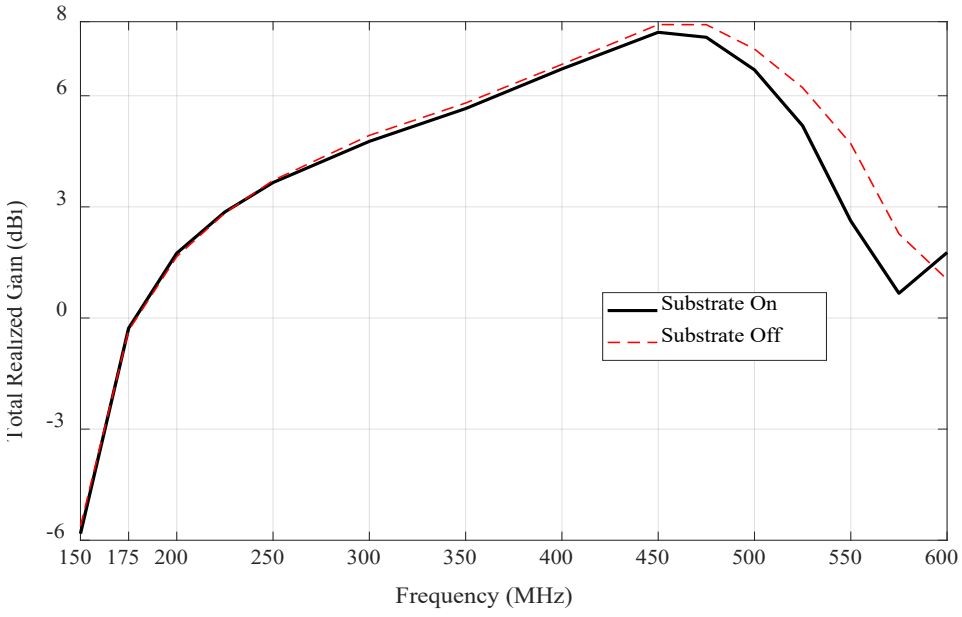

Figure 95: Substrate Effects on Gain

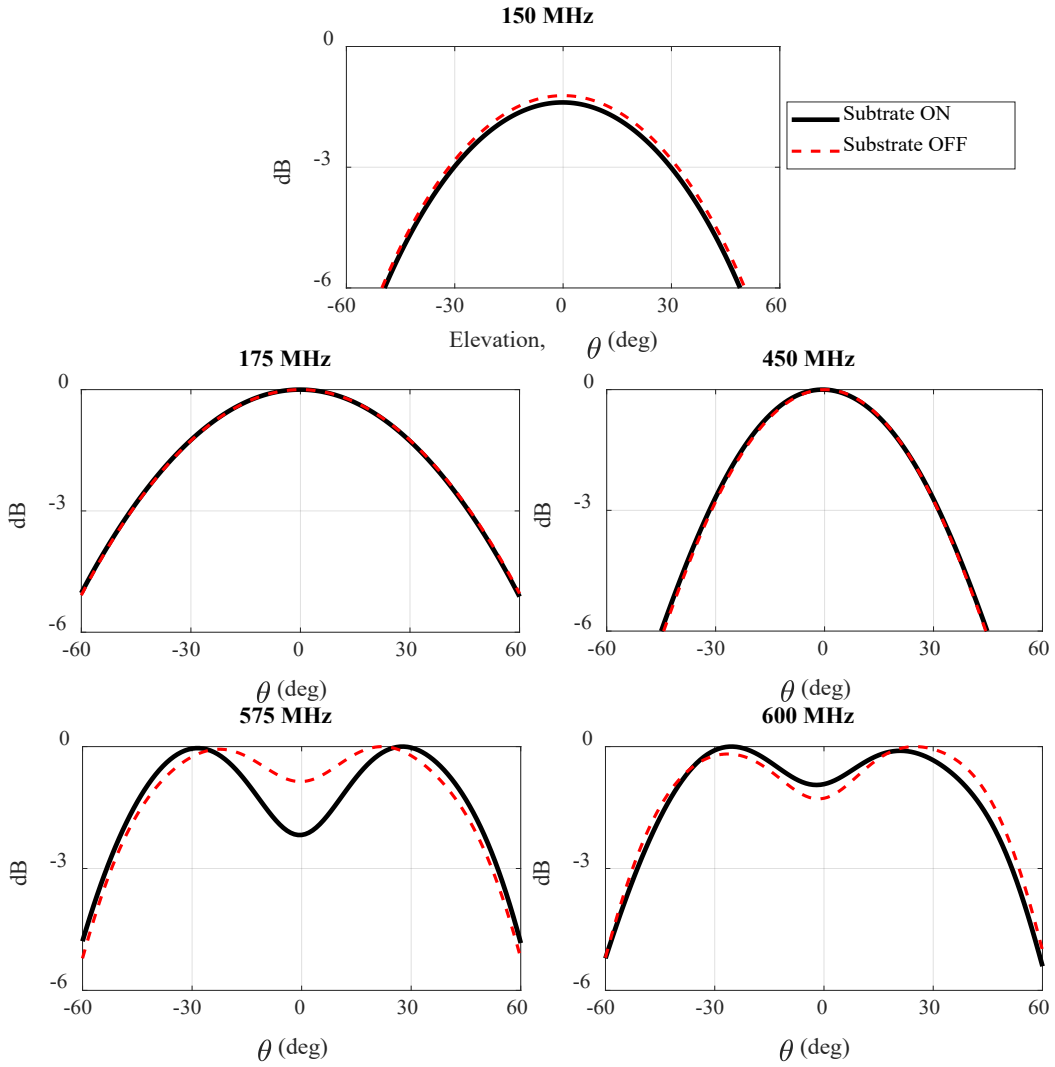

Figure 96: Substrate Effects on Patterns φ=90˚

Appendix D : Single Antenna Results with Array Factor

Contrary to the narrowing effect of the main beam along the cross-track direction due to the array factor, the general shape of radiation pattern along the X axis (along track) remains unchanged, but the main beam width becomes larger as shown in Figure 97.

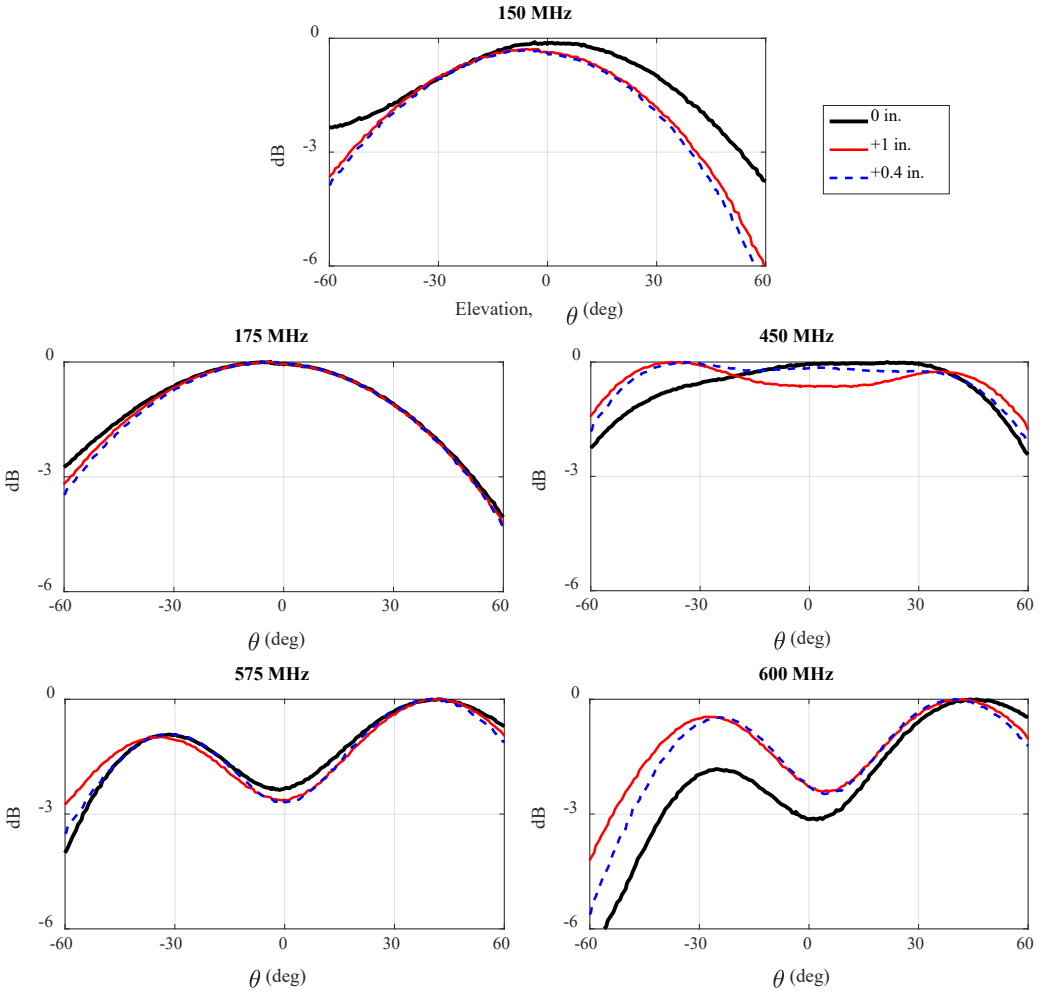

Figure 97: Normalized Measured Pattern with Array Factor, φ=0°

The resulting antenna array gain and radiation patterns using simulation results and an antenna array factor are shown in Figure 98 and Figure 99 respectively. These show similar results compared to the measured single antenna results with the array factor.

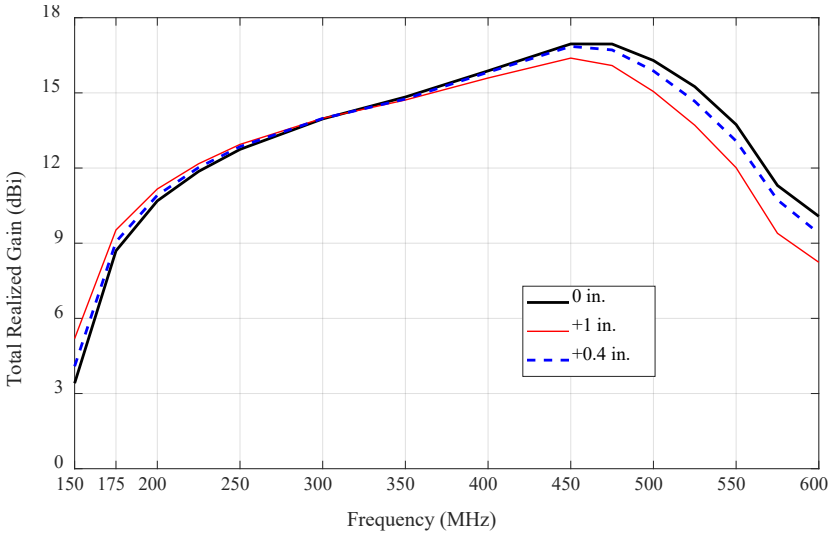

Figure 98: Simulated Antenna Gain with Array Factor for θ = 0°, φ=90°

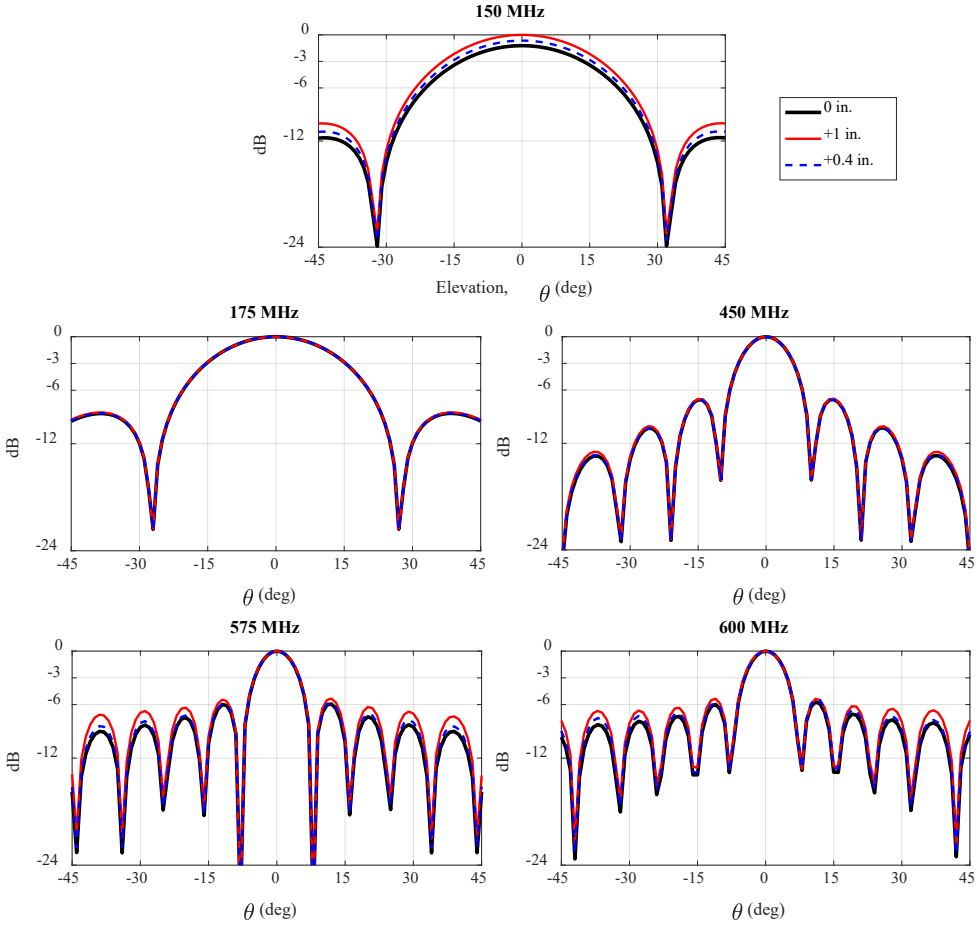

Figure 99: Normalized Simulated Antenna Pattern with Array Factor for φ=90°